Structural and optical properties of II-VI and III-V compound semiconductors

by

Jingyi Huang

A Dissertation Presented in Partial Fulfillment
of the Requirements for the Degree
Doctor of Philosophy

Approved April 2013 by the
Graduate Supervisory Committee:

Fernando A. Ponce, Chair
Ray W. Carpenter
David J. Smith
Michael M. J. Treacy
Hongbin Yu

ARIZONA STATE UNIVERSITY

May 2013

ABSTRACT

This dissertation is on the study of structural and optical properties of some III-V and II-VI compound semiconductors. The first part of this dissertation is a study of the deformation mechanisms associated with nanoindentation and nanoscratching of InP, GaN, and ZnO crystals. The second part is an investigation of some fundamental issues regarding compositional fluctuations and microstructure in GaInNAs and InAlN alloys.

In the first part, the microstructure of (001) InP scratched in an atomic force microscope with a small diamond tip has been studied as a function of applied normal force and crystalline direction in order to understand at the nanometer scale the deformation mechanisms in the zinc-blende structure. TEM images show deeper dislocation propagation for scratches along <110> compared to <100>. High strain fields were observed in <100> scratches, indicating hardening due to locking of dislocations gliding on different slip planes. Reverse plastic flow have been observed in <110> scratches in the form of pop-up events that result from recovery of stored elastic strain. In a separate study, nanoindentation-induced plastic deformation has been studied in *c*-, *a*-, and *m*-plane ZnO single crystals and *c*-plane GaN respectively, to study the deformation mechanism in wurtzite hexagonal structures. TEM results reveal that the prime deformation mechanism is slip on basal planes and in some cases, on pyramidal planes, and strain built up along particular directions. No evidence of phase transformation or cracking was observed in both materials. CL imaging reveals quenching of near band-edge emission by dislocations.

In the second part, compositional inhomogeneity in quaternary GaInNAs and ternary InAlN alloys has been studied using TEM. It is shown that exposure to antimony

during growth of GaInNAs results in uniform chemical composition in the epilayer, as antimony suppresses the surface mobility of adatoms that otherwise leads to two-dimensional growth and elemental segregation. In a separate study, compositional instability is observed in lattice-matched InAlN films grown on GaN, for growth beyond a certain thickness. Beyond 200 nm of thickness, two sub-layers with different indium content are observed, the top one with lower indium content.

To

My parents and my husband

ACKNOWLEDGEMENTS

First of all, I would like to express my deepest gratitude to my advisor, Professor Fernando A. Ponce, for his continued support and guidance throughout my Ph.D. study. He taught me a lot about how to approach research problems, how to analyze and understand the results from a physicist's perspective. His enthusiasm to work and patience with students has greatly impressed me. I appreciate very much his trust and encouragement during the research. It has been a great honor for me to study in his group.

I would also like to thank my committee members, Professor David J. Smith, Professor Michael M. J. Treacy, Professor Ray W. Carpenter, and Professor Hongbin Yu, for reviewing this dissertation. I am grateful for the use of facilities in the John M. Cowley Center for High Resolution Electron Microscopy, and I thank Karl Weiss, Gordon Tam and Dr. Zhenquan Liu for their technical support and assistance throughout my research.

I am extremely grateful to Professor David J. Smith and Professor Ray W. Carpenter for their wonderful teaching of transmission electron microscopy. I express my appreciation to Dr. Lin Zhou, Dr. Qiyuan Wei and Dr. Kewei Sun for sharing their hands-on experience of microscopy. Also thanks to Dr. Alec Fisher, Dr. Yu Huang, Dr. Reid Juday, Dr. Ti Li, Mr. Yong Wei and Mr. Hongen Xie for their discussion and collaboration.

I would like to thank Professor Rodrigo Prioli and his colleagues, especially Paula Caldas and Elizandra Martins, at the Catholic University of Rio de Janeiro in Brazil, Professor Ryuji Oshima at the University of Tokyo in Japan, Professor Takashi Egawa and Dr. Zhitao Chen at Nagoya Institute of Technology in Japan, for their collaboration

and providing interesting samples that are the subject of the research reported in this dissertation.

Many friends have helped me throughout these years. Their support and encouragement helped me overcome setbacks and stay sane during my graduate study. I greatly value their friendship and I deeply appreciate their belief in me.

Last, but not least, I would like to thank my husband Lei Zhang for his understanding, trust, and constant love during the past few years; and my parents for their unconditional love and support throughout my life. I would not have completed my Ph.D. study at Arizona State University without their encouragement.

TABLE OF CONTENTS

Page

CHAPTER Page

CHAPTER Page

LIST OF TABLES

LIST OF FIGURES

Figure Page

Figure Page

Figure Page

Figure Page

CHAPTER 1

INTRODUCTION

1.1 ELECTRON BANDS IN SEMICONDUCTORS

Semiconductors are a class of solid state materials that have electrical conductivity intermediate in magnitude between that of conductors and insulators. The resistivity of a semiconductor is within the range between 10^{-3} and 10^{9} Ω-cm, and it is strongly dependent on temperature.[1] The essential difference between conductors, semiconductors, and insulators can be visualized in the energy band diagram in Fig. 1.1. In solid state materials, the electronic states are closely spaced forming bands, some of which are separated by gaps without states. At absolute zero temperature, the upper occupied band, known as the valence band, is fully occupied in semiconductors. Next to the valence band, through a region without states, known as the band gap, is the conduction band, which is empty at zero Kelvin. Fig. 1.1 shows the difference in band gap energies for three types of solid state materials. Conductive materials have partially filled bands; sometimes with bands overlapping each other. Insulators have no free electronic carriers at room temperature. A semiconductor can have electronic carriers generated either by thermal excitation through a relatively narrow band gap, or by the introduction of doping impurities. The band gap is called "direct" if the position in momentum space of the minimum of the conduction band coincides with the maximum of the valence band; while it is called the "indirect" gap if they do not coincide.

Semiconductors can be classified into two types: elemental and compound. Elemental semiconductors are composed of single species of elements found in the group IV of the periodic table, such as silicon (Si) and germanium (Ge). Compound

semiconductors are formed by combining different elements, such as from Group IV (Si, Ge, Sn), from Group III and V (Al, Ga or In, with N, As, or Sb), or from Group II and VI (Zn or Cd, with O, S, Se, or Te). Table 1.1 lists some common elemental and binary compound semiconductor materials, their band gap values, and types. Three (ternary) or four (quaternary) element compound semiconductors, such as InGaN and GaInNAs, can also be formed and are commonly used in electronic and optoelectronic devices because their band gap and other physical properties (optical, structural, and electronic) can be adjusted by controlling the alloy composition.[2, 3]

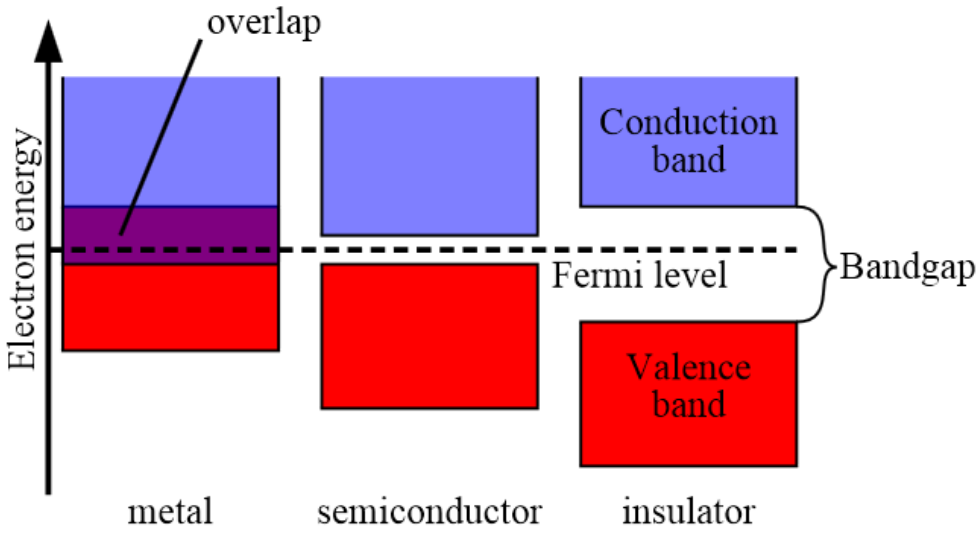

Fig. 1.1. Schematic diagram illustrating the energy band levels of a conductor, a semiconductor, and an insulator.

As already mentioned, at 0 K, intrinsic semiconductors are characterized by a filled valence band and an empty conduction band. Semiconductors can also be classified as intrinsic and extrinsic semiconductors. Conduction in intrinsic semiconductors is due to thermally excited carriers. Due to thermal excitation, electrons in the conduction band and holes in the valence band contribute to the electric current under an electric field. For

electronic engineering application, large carrier densities are usually needed for adequate electric conductivity. This can be achieved by introducing different impurities in a controlled manner, which will contribute either extra electrons (*n*-type dopants) or extra holes (*p*-type dopants). This process is called doping, which changes an intrinsic semiconductor to an extrinsic semiconductor (either *p*-type or *n*-type). Typical doping levels range from 10^{15} to 10^{18} cm^{-3}, and up to 10^{20} cm^{-3} for extremely highly doped materials.

Table 1.1 Band gap values and types of some common elemental and binary semiconductor materials.

Element semiconductors	Band gap (eV)	Gap type	Binary compound semiconductors	Band gap (eV)	Gap type
C	5.47	indirect	GaAs	1.43	direct
Si	1.11	indirect	InP	1.34	direct
Ge	0.67	indirect	GaN	3.44	direct
			InN	0.70	direct
			AlN	6.28	direct
			ZnO	3.37	direct

When a *p*- and *n*- type semiconductors are grown next to each other, a p-n junction is formed. This junction, also called a diode, is fundamental for electronic and optoelectronic applications. Fig. 1.2 (a) represents a typical band diagram of a p-n junction. At zero applied voltage, the valence and conduction bands bend in order to keep the Fermi level constant everywhere in the whole system. If a positive voltage is then applied on the p-type side of this system, the holes in the valence band of *p*-type semiconductor tend to flow to the *n*- side, and the electrons in the conduction band of *n*-type semiconductor tend to flow to the *p*- side. During this process, the electrons and

holes can recombine in the depletion region and generate photons, as illustrated in Fig. 1.2 (b), which is the basic process of a light emitting diode. On the other hand, if a p-n junction is connected in a circuit, and exposed to light as shown in Fig. 1.2 (c), it can absorb the light if the optical energy is larger than the diode band gap, generating electron-hole pairs. Then, in the absence of a voltage, the electrons and holes separate and flow to their corresponding lower energy states as shown to form a circuit. This process is the basis of a solar cell.

When two different semiconductor materials, with different band gaps, electron affinities, and indices of refraction are layered together, a heterojunction is formed. Heterojunctions are usually advantageous in many solid state device applications including semiconductor lasers, solar cells, and transistors. For example, carriers in a small direct band gap material like GaAs between two larger band gap layers like AlAs can be confined so that lasing occurs at room temperature with low threshold currents. Furthermore, heterostructures have been used as optical waveguides because of the different indexes of refraction.[4]

By far, Si is still the most widely used semiconductor material in the industry due to its low cost, relatively simple processing and fabrication. However, Si is an indirect band gap semiconductor, in which the electron must pass through an intermediate state and transfer momentum to the crystal lattice emitting or absorbing a photon. This results in poor light emitters and low light absorption coefficients,[5] making it unsuitable for many optoelectronic applications. Silicon also has a relatively low electron mobility,[6] making it unfit for certain high-speed electronic applications. Thus, more research and progress have been recently made on some compound semiconductors such as InP, GaN,

and ZnO, that have their own promising properties for optoelectronic and high-speed electronic applications. In this thesis, the structural and optical properties of these three materials and some of their alloys will be discussed.

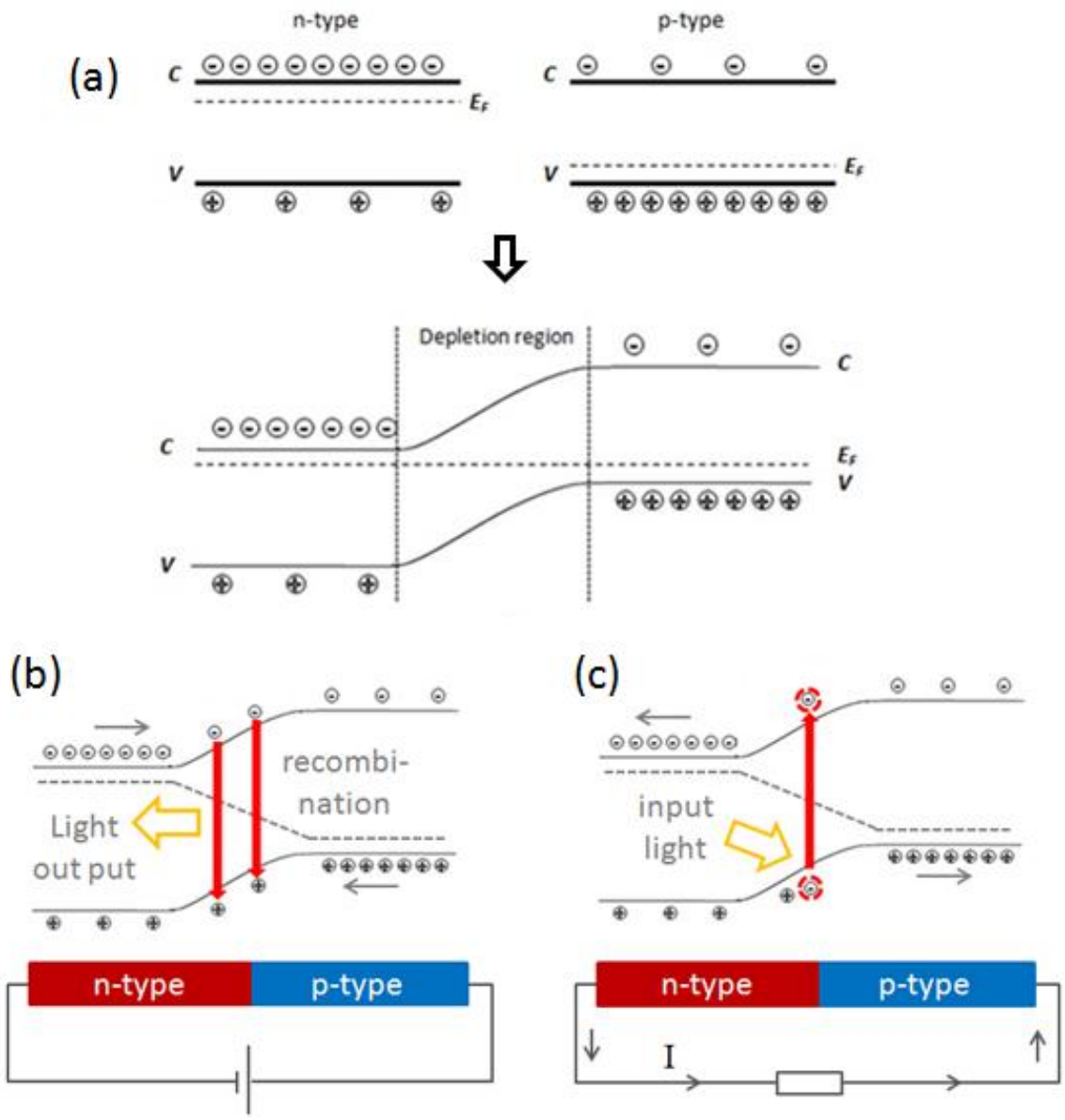

Fig. 1.2. Simplified band diagram of (a) a p-n junction, (b) LED, and (c) solar cell.

1.2 SOME COMMON COMPOUND SEMICONDUCTOR MATERIALS

1.2.1 INDIUM PHOSPHIDE

Indium phosphide (InP) is a III-V binary semiconductor with a direct band gap of 1.34 eV at room temperature. It has a zinc-blende (face-centered cubic) crystal structure, shown in Fig. 1.3, identical to that of GaAs and many other III-V semiconductors. Phosphorus atoms form a face-centered cubic structure, which are displaced by one fourth of the diagonal of the face-centered cube formed by indium atoms. The lattice constant of InP single crystal is ~5.87 Å.

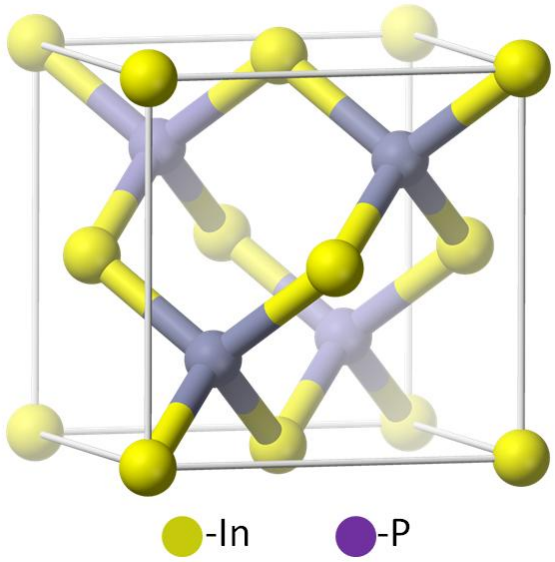

Fig. 1.3. Zinc-blend structure of InP single crystal.

InP-based materials are primarily used for the fabrication of telecommunication and electronic devices because they can operate with high efficiencies and at high power densities with superior electron velocities (~5400 $cm^2/(V\ s)$ at 300 K) with respect to Si (~1400 $cm^2/(V\ s)$ at 300 K). In addition, it has a direct bandgap, which makes it useful for the fabrication of laser diodes, LEDs, bipolar transistors, and solar cells.[7] However,

InP usually serves as the substrate for epitaxial InGaAs(P) growth. The reason for this is that InGaAs(P) can share the same lattice constant with InP while the band gap of the semiconductor alloy can be adjusted to a desired value.[8] This kind of structure is usually called InP-based material system. By carefully adjusting the composition of quaternary InGaAsP alloys grown on InP substrates, the available band gap spans the energy range from 0.75 to 1.35 eV, covering a suitable wavelength band for fiber communication systems. So, InP material plays an important role in optoelectronic materials and device technologies. On the other hand, the InP-based material system is a good candidate for high speed electronic devices and circuits. InGaAs, compared to GaAs, has smaller electron effective mass and higher electron mobility. InGaAsP/InAlAsP heterostructures, compared to GaAs/AlGaAs, have a larger conduction band offset and hence could achieve higher two-dimensional electron gas (2DEG) density. However, the determination of some practical device parameters in this material system usually needs the definite knowledge of many material parameters. Some elastic parameters for InP has been listed in Table 1.2.[9]

Table 1.2 Elastic parameters for InP (300 K). (The unit for Young's modulus is $\times 10^{12}$ dyn/cm^2)[9]

Planes and directions		Young's modulus Y	Poisson's Ratio P
{111} plane	<001>	6.106	0.357
	<011>	9.303	0.020
{110} plane	<001>	6.106	0.357
	<011>	11.27	0.236
{111} plane		9.303	0.369

1.2.2 GALLIUM NITRIDE

GaN is another III-V binary direct band-gap semiconductor material that currently is widely used in optoelectronic devices. Unlike InP, crystalline GaN material tends to have a wurtzite structure, shown in Fig. 1.4, but zinc-blende and rock-salt structures have also been observed under certain special conditions. This is because the electro-negativity of nitrogen atom is much larger than other group V elements, which leads to a higher ionicity in nitride semiconductors than in other III-V compounds such as the arsenides and the phosphides. Crystal structures with high ionicity tend to have the wurtzite structure.[10] Table 1.3 lists the crystallographic parameters of some important wurtzite III-nitride compounds and their common substrates.[11]

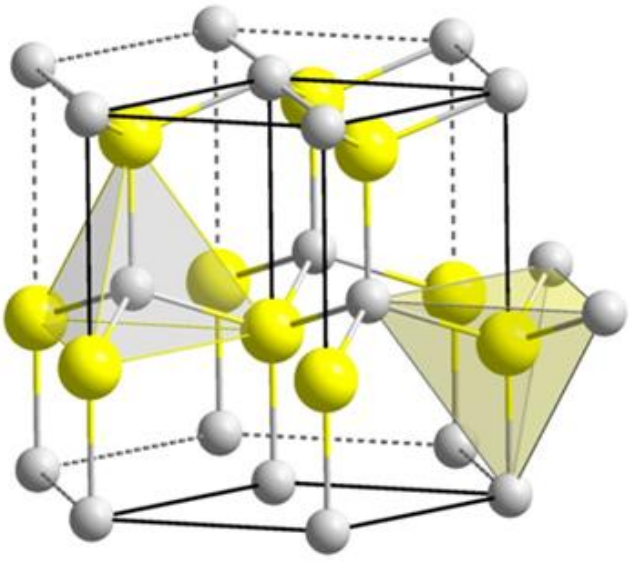

Fig 1.4. Atomic structure of GaN single crystal with wurtzite structure. The yellow balls represent Ga atoms and the grey ones represent N atoms.

Table 1.3 Crystallographic parameters of some important wurtzite III-nitride compounds and their favored substrates. (The unit of lattice parameter is Angstrom and the unit of thermal expansion coefficient is 10^{-6} ℃ $^{-1}$) [11]

Properties	AlN	GaN	InN	Sapphire	6H-SiC
Lattice parameter, a	3.112	3.189	3.545	4.758	3.081
Lattice parameter, c	4.982	5.185	5.703	12.991	15.092
c/a ratio	1.601	1.626	1.609	2.730	1.633
Thermal expansion coefficient along a	4.2	5.6	5.7	7.5	4.2
Thermal expansion coefficient along c	5.3	3.2	3.7	8.5	4.7

The first GaN single crystal layers were grown in 1969 by Maruska at RCA (Radio Corporation of America) using hydride vapor phase epitaxy (HVPE).[12] He used a mixture of hot gaseous gallium chloride and ammonia to react in a temperature controlled quartz furnace, then GaN film was deposited on a foreign substrate as a result. HVPE has a high growth rate so it is difficult to precisely control the thickness of epilayer, such as a quantum well which is typically several nanometers in thickness. Later on, meta-organic vapor phase epitaxy (MOVPE) has been introduced for the GaN growth where the reactants were changed to be metal organic gas (e.g., trimethyl-gallium) and ammonia. MOVPE has lower growth rate but the resulting film had rough surface during initial attempts. This problem was first solved by Akasaki and Amano in 1986 by introducing a low temperature deposited buffer layer.[13] Crack-free GaN films with flat surfaces were accomplished then. Nowadays, the optimum MOVPE growth condition for GaN is typically at 1000-1100 ℃ with a V/III ratio of thousands at near-atmospheric-pressure. Also, molecular beam epitaxy (MBE) is commonly used in scientific research institutions. MBE growth can direct elemental sources in ultra-pure gas form toward a

heated substrate under ultrahigh vacuum conditions (~10^{-5} to 10^{-11} torr). The growth rate is typically < 1 μm/hr, which is much lower than that of HVPE (~several hundred μm/hr) and MOVPE (~2 μm/hr). This low growth rate enables a precise layer-by-layer grow-process, hence abrupt interfaces.

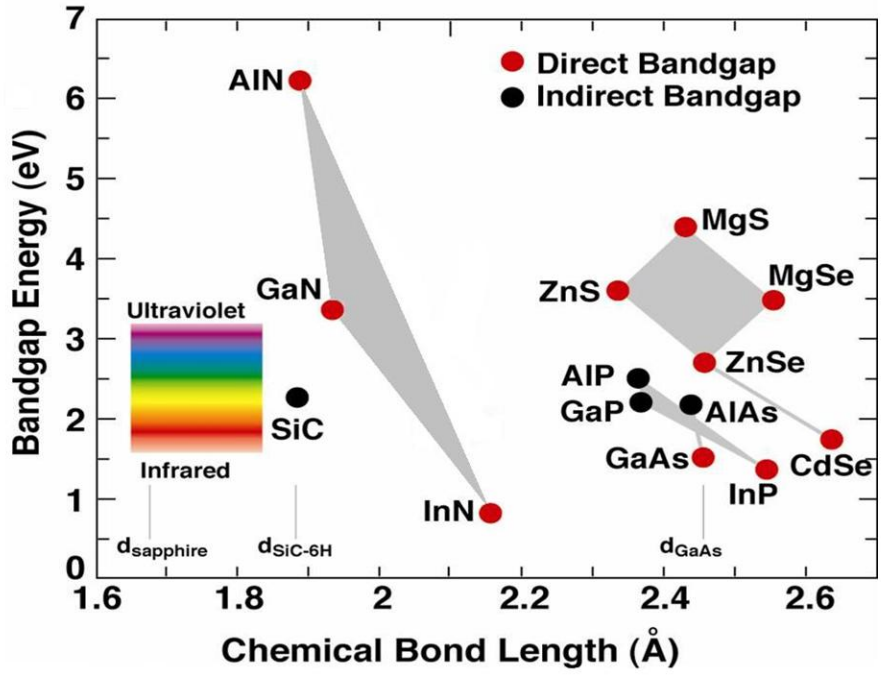

Fig. 1.5. Band gap of some semiconductors *vs* their chemical bond length.[14]

Si and Mg are commonly used as dopants for *n*-type and *p*-type III-nitrides. With the availability of both *n*-type and *p*-type materials, III-nitrides is widely applied to the optoelectronic devices such as LED and LD, because the band gap of InN, GaN, AlN, and their alloys can cover the whole visible spectrum as shown in Fig. 1.5.[14] However, $In_xGa_{1-x}N$ alloys exhibit phase separation via spinodal decomposition – this pseudo-binary system has a miscibility gap between two species, shown in Fig.1.6.[15] Within

the spinodal region, when the free energy change is negative, the system becomes unstable leading to composition fluctuations. $In_xGa_{1-x}N$ quantum wells (QWs) also suffer phase separation and form compositional-modulated "In-rich dots", which may act as nonradiative recombination centers at extended defects in III-nitride LEDs.[16] On the other hand, control of the threading dislocations (TDs) introduced during growth is another challenge for III-nitrides. Due to the disorientated columnar growth of tilted, twisted, or a combination of these two grains, pure edge, screw and mixed TDs can be generated in GaN as sketched in Fig. 1.7 and Table 1.4.[17, 18] These TDs, which usually have a density of ~10^9 -10^{10} cm^{-2}, and are considered as non-radiative recombination centers that degrade the optical properties.[19]

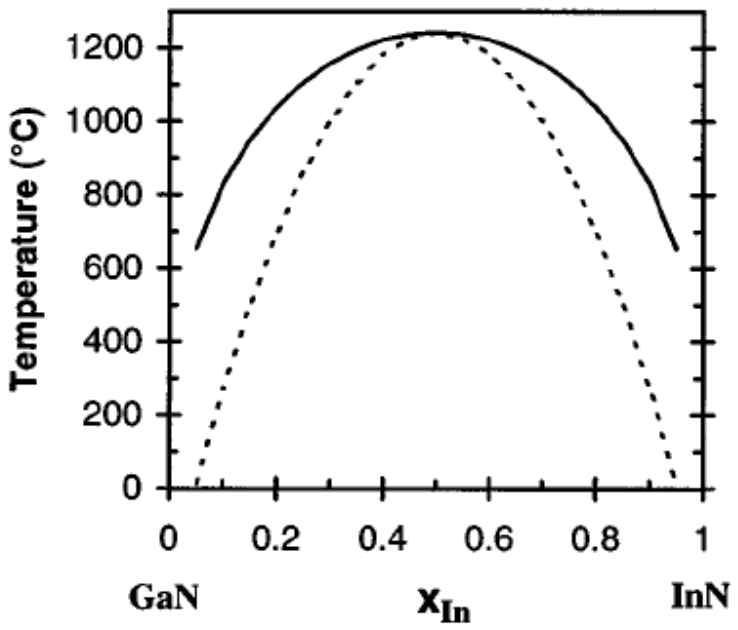

Fig. 1.6. Binodal (solid) and spinodal (dashed) curves for the $In_xGa_{1-x}N$ system, calculated assuming a constant average value for the solid phase interaction parameter.[15]

Table 1.4 Type of threading dislocations in III-nitrides and their Burgers vectors.[17]

Dislocation type	Burgers vector
Pure edge	1/3<11-20>
Pure screw	1/2<0002>
mixed	1/3<11-23>

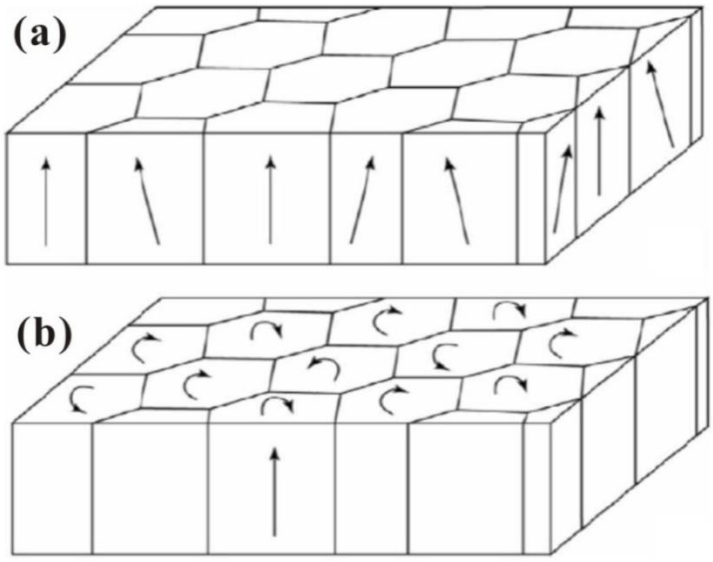

Fig. 1.7. Schematic diagram of the columnar growth of GaN on sapphire substrates, containing tilt (a) and twist (b) components with dislocations existing at the boundaries between grains.[18]

1.2.3 ZINC OXIDE

Zinc Oxide (ZnO) is an II-VI direct wide band gap (~3.37 eV at room temperature) compound semiconductor. Like most of the group II-VI binary compound semiconductors, it crystallizes in either cubic zinc-blende or hexagonal wurtzite structure. At relatively high pressures, it may have rocksalt structure. But at ambient conditions, the thermal-dynamically stable phase is the wurtzite structure, similar to GaN, as shown in

Fig 1.4. Gerward and Osen observed that the hexagonal wurtzite structure of ZnO undergoes a structural phase transformation with a transition pressure starting at 10 GPa and being complete at about 15 Gpa.[20] Also people have observed a clear wurtzite-to-rocksalt transition statring at 9.1 GPa and completing at 9.6 GPa, resulting in a 16.7% change in the unit-cell volume.[21] Then upon decompression, ZnO reverts to the wurtzite structure at about 2 GPa, below which a single phase is present. For wurtzite ZnO single crystal, the lattice constants is about 3.24 Å for the *a* parameter and about 5.20 Å for the *c* parameter. These lattice values could vary slightly due to point defects such as zinc antisites, oxygen vacancies, and extended defects such as threading dislocations. So, the *c/a* ratio varies from 1.593 to 1.604 for wurtzite ZnO.

Similar to GaN, ZnO thin films have a tendency to grow preferentially along (0001) orientation on various substrates, including glass, sapphire, and diamond.[22-24] Nowadays, high-quality ZnO single-crystal films are prepared by RF magnetron sputtering, molecular-beam epitaxy (MBE), pulsed-laser deposition (PLD), metal-organic chemical-vapor deposition (MOCVD), and hydride vapor-phase epitaxy (HVPE).[25-29] In comparison with GaN grown on sapphire, ZnO grown on sapphire has approximately equivalent x-ray diffraction (XRD) and photoluminescence (PL) line widths, and even lower dislocation density.[30] The improved quality of ZnO films has made it gain substantial interest in the research community over decades. ZnO highly *n*-type doped with Al or Ga is transparent to visible light and it is electrically conductive, so it has been widely used for optical coatings, such as energy-saving or heat-protecting windows.[31] Research effort on ZnO has been intensified lately for better understanding of its physical properties, developing high-quality ZnO crystals and nanostructures for device

applications because ZnO has some unique properties and advantages, leading it to some potential applications. For example, ZnO has a wide band gap and a large exciton binding energy (60 meV), which could lead to UV lasing action and bright emission even above room temperature. In addition, ZnO is also very favorable to nano-scale structures and devices because this material lends itself nicely to production of nanostructures from which functional devices have already been fabricated. Although ZnO has already been applied to industry because of its piezoelectric properties and band gap in the near ultraviolet, its application to optoelectronic devices has not been materialized due to the lack of reproducible and low-resistivity *p*-type epitaxial layers. This is partly due to strong self-compensation effects associated with potential *p*-type dopants. So, this issue need to be overcome before ZnO can be applied to practical use, as was the case for GaN.

1.3 INDENTATION AND ITS APPLICATION TO SEMICONDUCTORS

In semiconductor industry, each device production involves a lot of material processing, handling and fabrication, which would bring in significant contact load that could introduce plastic deformation or even fracture, leading devices to failure performances. Thus, the understanding of mechanical properties on such semiconductor materials is very important. Indentation has been the most commonly used technique to measure the mechanical properties of materials. The first test was performed by Brinell at the beginning of the 20^{th} century using a spherical and smooth steel ball as an indenter to characterize the hardness of materials by tracking the applied force and the penetration of the indenter.[32] After that, this technique was quickly adapted to industrial test because of the ease and speed with which it can be carried out. During that time, the typical size of an indenter was at millimeter scale, or even larger. By extending the Hertz model,

which solved the classical problem of an isotropic elastic material indented by a spherical frictionless indenter,[33] to anisotropic media and to a variety of indenter shape, load, and displacement sensing indentation testing was used as an experimental tool for measuring elastic modulus starting in the early 1970's by Bulychev *et al*.[34, 35] As shown in Fig. 1.8, this is the schematic diagram of a typical indentation test and the load-displacement curve. From the information extracted from the curve, some important mechanical properties such as hardness H and stiffness S can be analyzed according to the equations listed below.

$$H = \frac{P_{max}}{A_p} \quad ; \qquad S = \frac{dP}{dh} = \frac{2}{\sqrt{\pi}} E_r \sqrt{A_p} \quad ;$$

Here, A_p is the projected area of the hardness impression. While the unloading stiffness is computed from a linear fit of the upper one-third of the unloading curve. E_r is the reduced modulus determined from the equation

$$\frac{1}{E_r} = \frac{(1-\gamma^2)}{E} + \frac{(1-\gamma_i^2)}{E_i} \quad ;$$

Where E and γ are Young's modulus and Poisson's ratio for the specimen and E_i and γ_i are similar parameters for the indenter.

Later on, with the development of imaging technique for the indent, indentation test has been extended down to smaller scales, which makes instruments capable of accurately measuring loads as small as nano-newton and displacements of about 0.1 nm throughout an indentation. The developments of nanoindentation techniques, atomic force microscopy (AFM) and the interface force microscopy (IFM), which are ideal for imaging of nanometer-scale indents, enable *in situ* imaging of an indentation, providing important information about the deformation and cracking.[36-38] It has been widely

used to estimate the deformation in a very small volume, such as the estimation of the fracture toughness of some ultrathin films, which cannot be measured by conventional indentation tests.

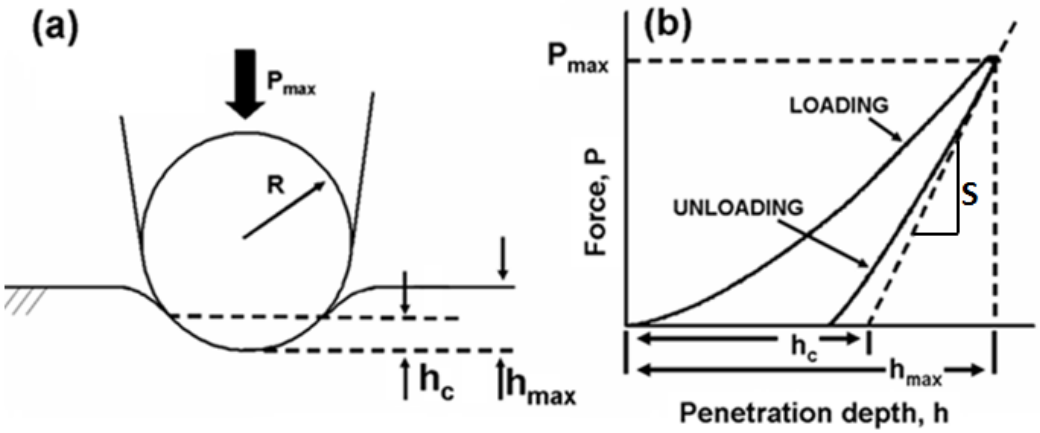

Fig. 1.8. (a) is the schematic figure showing the indentation and some important parameters. R is the radius of curvature of the indentation tip, and h_c is the vertical depth of the tip that is in contact with the sample; H_{max} is the penetration depth of the tip from the surface; P_{max} is the maximum load; (b) is a typical load Vs penetration depth curve.

On the other hand, recent studies have shown that alterations of the near-surface crystal structure can be used for growth of semiconductor nanostructures at specific surface sites.[39, 40] Atomic force microscope and nano-indentation tips have recently been used to produce surface patterns in order to control the site nucleation of semiconductor nano-structures. The patterns were created as shallow indentations on the semiconductor surface, which resulted in mechanical deformation of the semiconductor with the introduction of dislocations. As shown in Fig. 1.9, atomic force nanolithography is exerted on an InP substrate to grow InAs nanostructures.[41] The left image (a) shows the indentation pits produced by the AFM tip with a controllable force, and in figure (b) on the right, it is observed that the nano-crystals are controllably grown on the indentation pits. While figure (c) shows the influence of the increasing applied normal

indentation force on the nucleation of nano-crystals. It reveals that it is not the pits themselves but the deformation-induced dislocations that could control the growth pattern of nanostructures. On the other hand, to take the advantage of the controllable lateral movement of the AFM tip, nano-scratching can be exerted, which is another way to introduce measurable deformation. The grooves produced by nano-scratching have been used to grow nano-crystal arrays.[42] Therefore, nano-indentation as well as nano-scratching can not only be used to measure mechanical properties of semiconductor materials, but also for growth of semiconductor nano-structures.

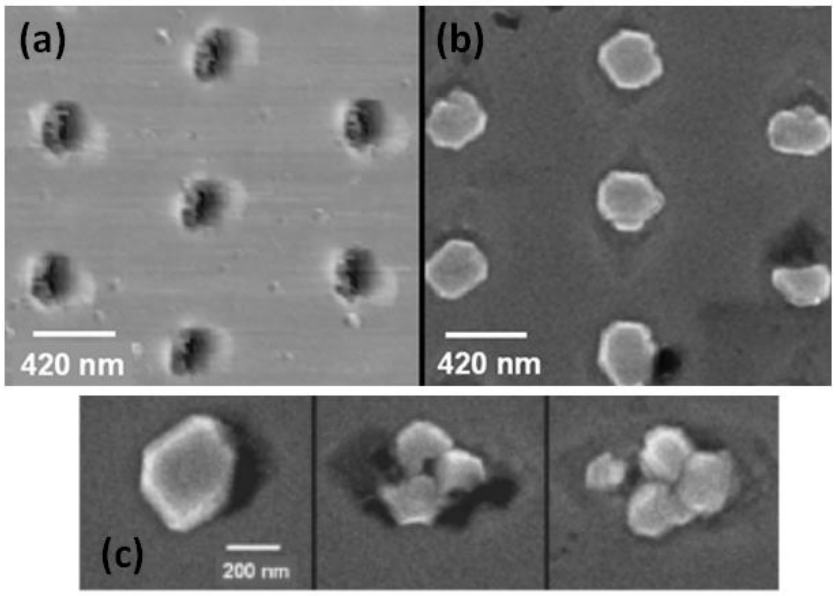

Fig. 1.9. SEM images of nano-indentation pits and the nano-crystals growth site-controlled by the pits.[40]

1.4 INTRODUCTION OF MECHANICAL DEFORMATION

As described above, an indentation (or scratch) could introduce mechanical deformation when the tip contact with material surface with certain load. So it is important to understand the mechanical deformation process. This kind of study was mostly exerted on metals or amorphous materials. A typical stress-strain curve for ductile

metal wire is sketched in Fig. 1.10. From the curve, the stress is linearly proportional to the strain up to the proportionality limit, with a small non-linearly extension to the elastic limit. From the original point to the elastic limit, the deformation is reversible during loading/unloading and this region is called elastic region. If the stress is applied beyond elastic limit, the yield point would be reached, which will cause the material to be deformed permanently. At the end of the unloading, there would exist a permanent strain (usually referred to be a "set") in the material. This kind of deformation is called plastic deformation. It is important to notice that beyond elastic limit, the curve covers a relatively large strain region within a very small, almost negligible stress change. And we call this kind of region yielding region. After the yielding region, the load needs to increase for additional strain to occur. This effect is called strain hardening, which is associated with an increased resistance to slip deformation. Then if the loading is continued beyond the ultimate stress, the cross-sectional area of the material decreases rapidly until it starts fracture. The region between the ultimate stress and fracture point is called necking region.

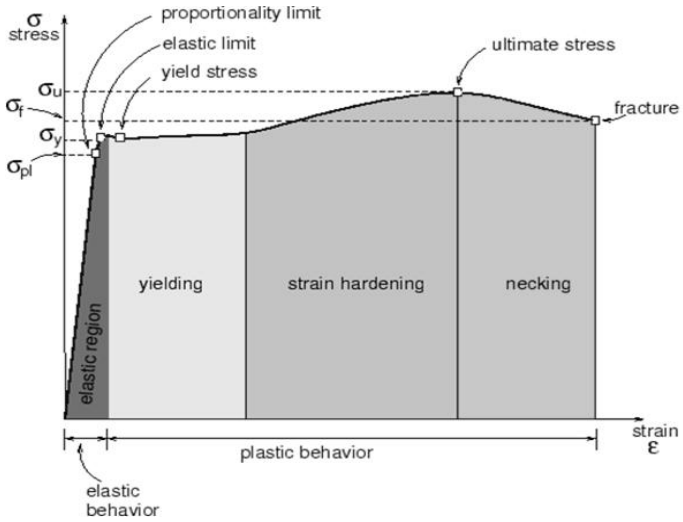

Fig. 1.10. A typical stress-strain curve for ductile metal wire.

Lately, the study of mechanical deformation on some semiconductor crystals, such as Si, InP, and ZnO has been emphasized considering the rapid growth of semiconductor industry. Similar with the description on the metals above, these semiconductor crystals undergo elastic, plastic deformation sequentially as the applied stress increase until reach fracture point. However, compared to the ductile metal, these semiconductor crystals are much more brittle. So when the applied stress reaches the yield point, instead of yielding in a form of flow, the crystal is more likely to be hardened with dislocation generation, propagation and locking. It is because with small elastic recovery region (<0.1% for most semiconductor crystals), to conform the crystal surface with the shape of the tip, shear stress gradient between slip planes could easily build up then lead to a slip step on the surface, meanwhile, to form a dislocation in the crystal. As the tip keep advancing into the crystal, more and more steps are formed to conform the shape of the tip. And more and more dislocations are generated. These dislocations tend to propagate into the crystal until they are locked or pinned with each other. With these locking and pinning, the crystal material becomes strain hardening. Take an indentation on InP for example. It has a zinc-blende structure, which has a <110>{111} slip system. When a spherical indenter is applied on the crystal surface, slip steps could occur at the surface, dislocations are generated in front of the slip steps and propagate in certain {111} slip planes as sketched in Fig. 1.11.[43]

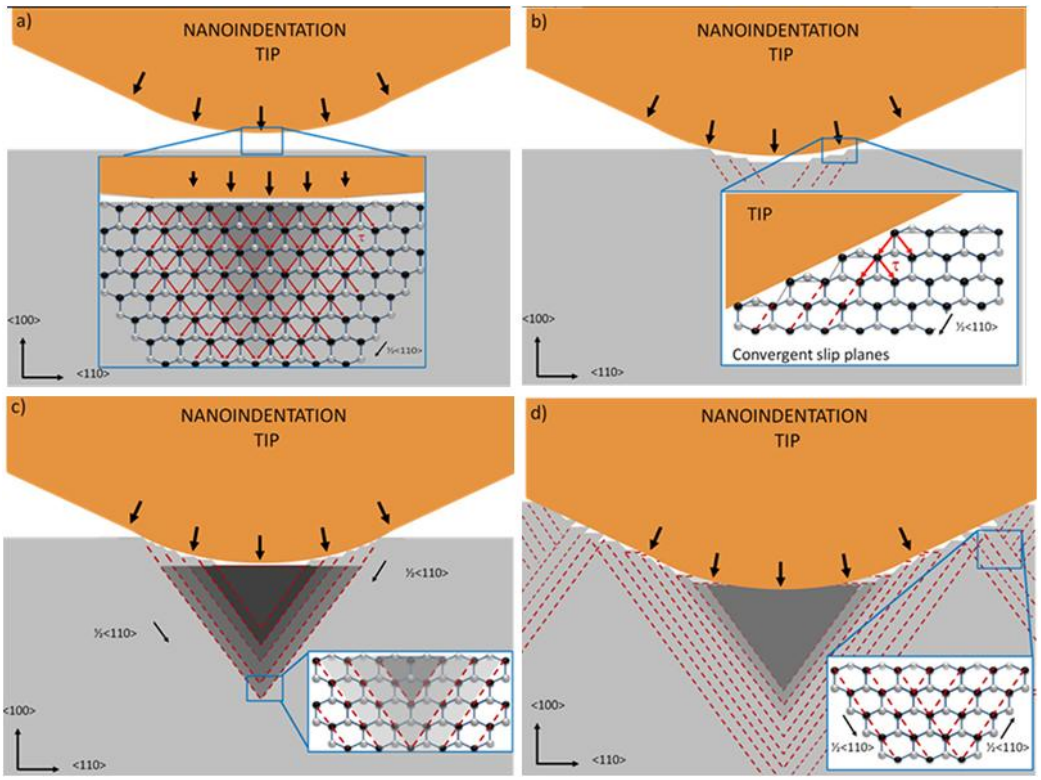

Fig. 1.11. Indentation induced plastic deformation happened in InP single crystal with the activation of slip planes below the tip.[43]

1.5 OUTLINE OF DISSERTATION

The work described in this dissertation is the study on some common compound semiconductors by using transmission electron microscopy (TEM) as well as some other characterization techniques. The experimental techniques involved in this study, such as cathodoluminescence (CL), scanning transmission electron microscopy (STEM), and atomic force microscopy (AFM) are reviewed in Chapter 2. Starting from Chapter 3 to Chapter 7, some of my research work and important results are described. This work can be generally summarized into two aspects. One is the study of defects generated during nano-scale plastic deformation introduced by contact loads on different semiconductor structures. Using conventional TEM diffraction analysis and CL, the microstructure, and

optical properties of nano-scratched InP single crystal, nano-indented ZnO single crystal and GaN films are discussed in Chapter 3 and 4. Chapters 5 and 6 describe fundamental material issues related to the III-nitride alloys and their optoelectronic devices. Chapter 5 represents the compositional inhomogeneity in GaInNAs and Chapter 6 discusses the compositional instability in the lattice-matched InAlN/GaN epitaxy. Finally, in Chapter 7 the main findings of this dissertation are summarized and some future work is suggested.

REFERENCES

[1] B. G. Yacobi, *Semiconductor Materials: An Introduction to Basic Principles* (Kluwer Academic, New York, 2003), p. 1.

[2] R. F. Pierret, *Semiconductor Device Fundamentals*, (Addison-Wesley, 1996), p. 354.

[3] D. A. Neamen, *Semiconductor Physics and Devices: Basic Principles* (3rd Ed., McGraw-Hill, 2003), p. 617.

[4] I. Vurgaftman , J. R. Meyer, and L. R. Ram-Mohan, J. Appl. Phys. **89**, 5815 (2001).

[5] P. Bhattacharya, *Semiconductor optoelectronic devices* (2nd Ed., Prentice Hall, Upper Saddle River, NJ, 1997), pp. 115-118.

[6] S. M. Sze, and K. K. Ng, *Physics of Semiconductor Devices* (3rd Ed., John Wiley & Sons, Inc., Hoboken, NJ, 2007), p. 30.

[7] V. Swaminathan and A. T. Macrander, *Material Aspects of GaAs and InP Based structures*, (Prentice Hall, Englewood Cliffs, 1991), pp. 265, 266.

[8] P. Bhattacharya, *Properties of Lattice-Matched and Strained InGaAs*, (London, 1993), p. 16.

[9] S. Adachi, *Physical Properties of III-V Semiconductor Compounds*, (Wiley-VCH, Weinheim, 2004), p. 23.

[10] J. C. Phillips, *Bonds and Bands in Semiconductors*, (Academic, New York, 1973), p. 71-74.

[11] F. A. Ponce, in *Group III-Nitride Semiconductor Compounds*, ed. by B. Gil (Oxford Univ. Press, Oxford, 1998), p. 127.

[12] M. P. Maruska, and J. J. Tietjen, Appl. Phys. Lett. **15**, 327 (1969).

[13] H. Amano, N. Sawaki, I. Akasaki, and Y. Toyoda, Appl. Phys. Lett. **48**, 353 (1986).

[14] F. A. Ponce, and D. P. Bour, Nature, London, **386**, 351 (1997).

[15] I. Ho, and G. B. Stringfellow, Appl. Phys. Lett. **69**, 2701 (1996).

[16] S. Chichibu, T. Azuhata, T. Sota, and S. Nakamura, Appl. Phys. Lett. **69**, 4188 (1996).

[17] F. A. Ponce, D. Cherns, W. T. Young, and J. W. Steeds, Appl. Phys. Lett. **69**, 770 (1996).

[18] F. A. Ponce, Mater. Res. Soc. Bull, **22**, 51 (1997).

[19] D. Cherns, Mater. Sci. and Eng. B. **91/92**, 274 (2002).

[20] L. Gerward, and J. S. Olsen, J. Synchrotron Radiat. **2**, 233 (1995).

[21] S. Desgreniers, Phys. Rev. B. **58**, 14102 (1998).

[22] T. Yamamoto, T. Shiosaki, and A. Kawabata, J. Appl. Phys. **83**, 7844 (1998).

[23] T. Mitsuyu, S. Ono, and K. Wasa, J. Appl. Phys. **51**, 2464 (1980).

[24] A. Hachigo, H. Nakahata, K. Higaki, S. Fujii, and S. Shikata, Appl. Phys. Lett. **65**, 2566 (1994).

[25] K.–K. Kim, J.–H. Song, H.–J. Jung, W.–K. Choi, S.–J. Park, and J.–H. Song, J. Appl. Phys. **87**, 3572 (2000).

[26] P. Fons, K. Iwata, S. Niki, A. Yamada, and K. Matsubara, J. Cryst. Growth. **201-202**, 627 (1999).

[27] R. D. Vispute, V. Talyansky, R. P. Sharma, S. Choopun, M. Downes, T. Venkatesan, Y. X. Li, L. G. Salamanca-Riba, A. A. Lliadis, K. A. Jones, and J. McGarrity Appl. Sur. Sci. **127**, 431 (1998).

[28] Y. Liu, C. R. Gorla, S. Liang, N. Emanetoglu, Y. Lu, H. Shen, and M. Wraback, J. Electron. Mater. **29**, 69 (2000).

[29] N. Takahashi, K. Kaiya, T. Nakamura, Y. Momose, and H. Yamamoto, Jpn. J. Appl. Phys. Part 2 **38**, L454 (1999).

[30] J. Narayan, K. Dovidenko, A. K. Sharma, and S. Oktyabrsky, J. Appl. Phys. **84**, 2597 (1998).

[31] C. Kingshirn, ChemPhysChem. **8**, 782-803 (2007).

[32] D. Tabor, *The Hardness of Metals,* (Oxford University Press, Oxford, 2000), p. 6.

[33] H. Hertz, J. Reine Angewandte Math. **92**, 156 (1882).

[34] S.I. Bulychev, V.P. Alekhin, M.Kh. Shorshorov, and A.P. Ternovskii, Prob. Prochn. **9**, 79 (1976).

[35] M. Kh. Shorshorov, S. I. Bulychev, and V. P. Alekhin, Sov. Phys. Dokl. **26**, 769 (1982).

[36] J. S. Field and M. V. Swain, J. Mater. Res. **10**, 101 (1995).

[37] W. W. Gerberich, J. C. Nelson, E. T. Lilleodden, P. Anderson, and J. T. Wyrobek, Acta Mater. **44**, 3585 (1996).

[38] P. Tangyunyong, R. C. Thomas, J. E. Houston, T. A. Michalske, R. M. Crooks, and A. J. Howard, Phys. Rev. Lett. **71**, 3319 (1993).

[39] H. Z. Song, Y. Nakata, Y. Okada, T. Miyazawa, T. Ohshima, M. Takatsu, M. Kawabe, and N. Yokoyama, Physica E **21**, 625 (2004).

[40] C. Taylor, E. Marega, E. A. Stach, G. Salamo, L. Hussey, M. Munoz, and A. Malshe, Nanotechnology **19**, 015301 (2008).

[41] H. D. Fonseca-Filho, R. Prioli, M. P. Pires, A. S. Lopes, P. L. Souza, and F. A. Ponce, Appl. Phys. Lett. **90**, 013117 (2007).

[42] F. A. Ponce, Q. Y. Wei, Z. H. Wu, H. D. Fonseca-Filho, C. M. Almeida, R. Prioli, and D. Cherns, J. Appl. Phys. **106**, 076106 (2009).

[43] C. M. Almeida, R. Prioli, Q. Y. Wei, and F. A. Ponce, J. Appl. Phys. **112**, 063514 (2012).

CHAPTER 2

EXPERIMENTAL TECHNIQUES

2.1 NANOINDENTATION AND NANOSCRATCHING

2.1.1 NANOINDENTATION USING A NANOINDENTER SYSTEM

The nano-indenter is an apparatus that allows the study of mechanical properties of materials via indentations and scratches. It basically consists of a tip, similar to the ones used in atomic force microscopy, a piezoelectric ceramic which controls the positioning of the tip on the sample, a transducer which controls the force applied and the displacement during the indentation, a stage with its movement controlled by piezoelectric ceramics, and a system of acoustic insulation – a suspended workbench. The nano-indenter used in this thesis is a Triboscope Hysitron installed in the Van de Graaff Laboratory at PUC-Rio. The tip has a conospherical shape with a radius of 260 nm, as shown in Fig. 2.1.

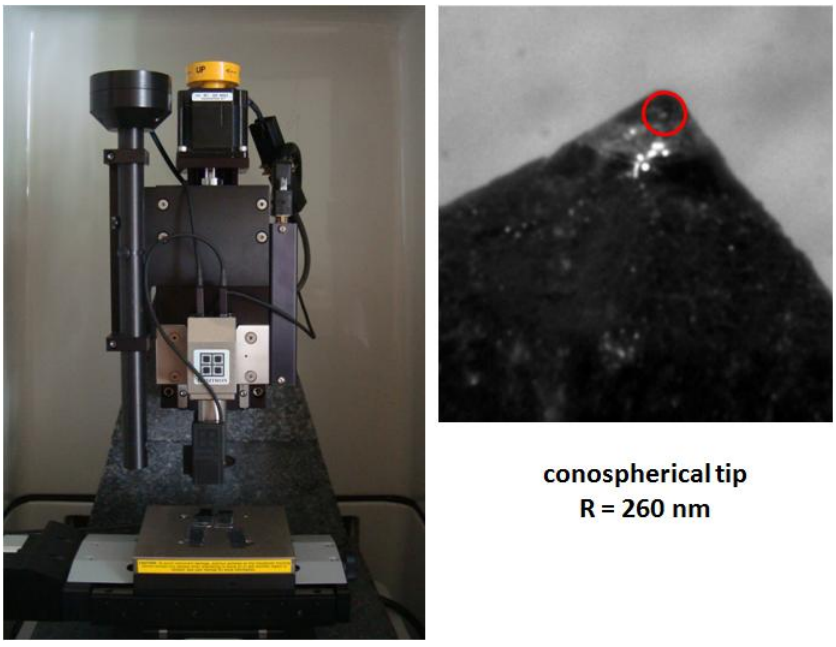

Fig. 2.1. Photos of the nanoindenter system set-up and its conospherical tip.

2.1.2 NANOSCRATCHING IN AN ATOMIC FORCE MICROSCOPE (AFM)

The AFM is a microscope which belongs to the group of Scanning Probe Microscopes (SPM). They are basically composed of a probe, a piezoelectric ceramics to position the sample, a feedback system that controls the vertical position of probe, and a computer that controls the sample, stores data and converts them into images. The AFM tip is fixed at the end of a rod, known as cantilever as sketched in Fig. 2.2(b). The sample is fixed on a stand and positioned over the piezoelectric ceramic, which can move in the x, y and z directions by applying a voltage. Therefore, as the tip scans over the surface, topographic changes on the sample surface imply variations in the interaction force between tip and surface causing a deflection of the cantilever, which is recorded by a laser reflecting on the end of the cantilever and striking on a photo detector connected to an acquisition system. The topographic analysis can be operated in either contact mode or no-contact mode. In contact mode, the tip is placed in "contact" with the sample; while in non-contact mode cantilever is set to vibrate with low amplitudes.

As shown in Fig. 2.2(a), the AFM, used for lithography of the patterns and for the characterization of patterns exhibited in this thesis, is a MultiMode model equipped with a controller IIIa of Veeco installed in the Van de Graaf Laboratory at PUC-Rio. To perform lithography, AFM was set in contact mode at approximately constant force to indent and scratch the surface. The tip is a diamond grit with three pyramidal faces {110}, which has a radius of curvature of ~60 nm, pointing in the [111] direction of diamond. The stainless steel cantilever has a spring constant of 132 nN/nm. In order to create nano-scratch patterns, the force that the tip makes on the sample surface is increased to a

desired value and then the sample is moved with respect to the tip. A trench is left on the surface when the force is great enough to produce plastic deformation in the material.

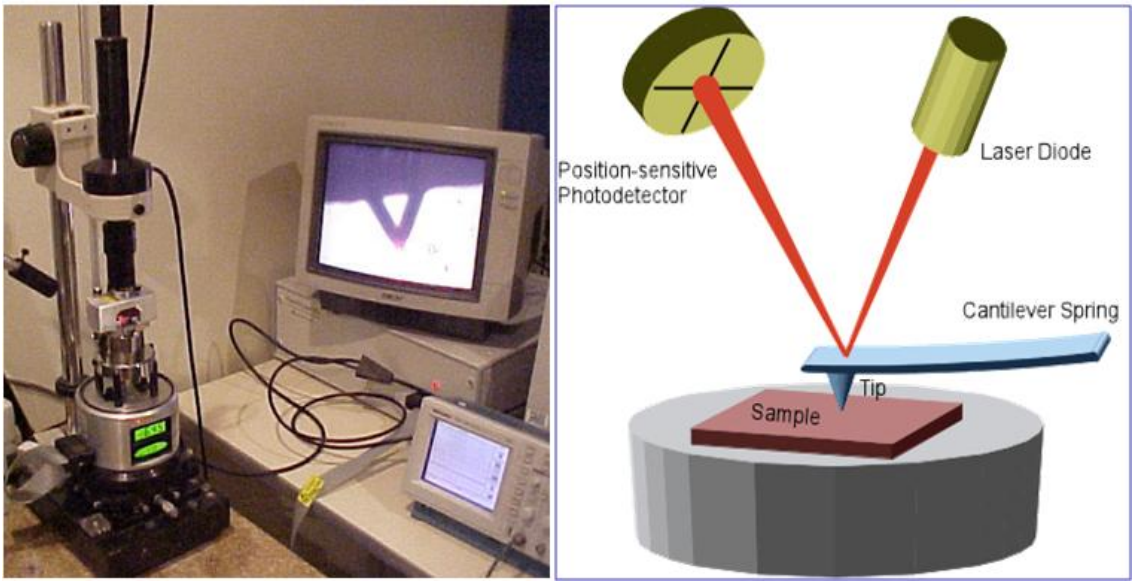

Fig. 2.2. (a) Photo of the nano-scratching system in AFM, and (b) schematic diagram showing essential components of an AFM.

2.2 MATERIAL CHARACTERIZATION

2.2.1 CATHODULUMINESCENCE

Cathodoluminescence (CL) is the generation of light that results from the interaction between electron exposure (source) and a material. When an electron beam impacts on a semiconductor material, electrons from the lower energy state are promoted into higher energy states, leaving behind empty states known as holes. When an electron and a hole recombine, it is possible for a photon to be emitted. The luminescence can be divided into two types. (1) intrinsic type, due to electron-hole pair recombination that involves a transition of an electron from the conduction band to the valence band, and (2) extrinsic type, due to carrier recombination via impurity states within the band. Usually, the CL system is installed in a scanning electron microscope (SEM) to achieve versatile

characterization capabilities. The high spatial resolution in the SEM enables characterization of the light emitted from regions as small as tens of nanometers, up to the millimeter scale, which makes CL suitable for analyzing luminescent details related to fine microstructure features as well as looking at large area emission representing bulk properties. The CL system used in this dissertation is shown in Fig. 2.3, and consists of 4 main parts: (1) SEM, (2) parabolic mirror, (3) spectrometer, and (4) photon detector, which in our case is a photomultiplier tube (PMT). The SEM is a JEOL 6300 equipped with a LaB_6 thermionic electron gun.

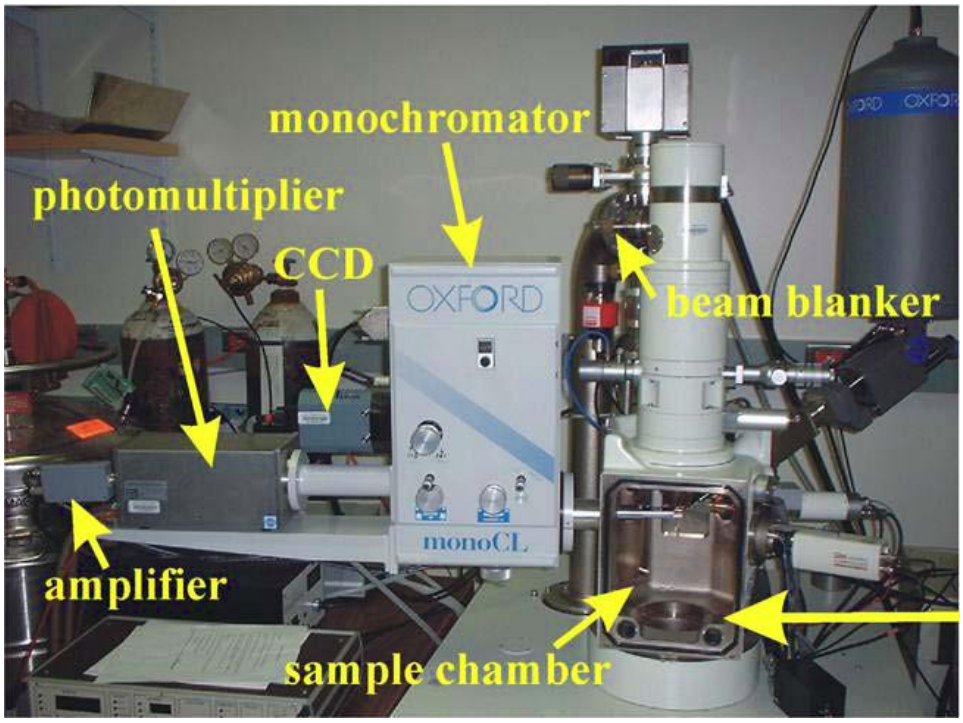

Fig. 2.3. Image of the CL system used in this dissertation.

2.2.2 TRANSMISSION ELECTRON MICROSCOPE

Material properties can always be traced back to the type of atoms, atomic configuration, and their arrangement into microstructures. Transmission electron microscopy (TEM) is a powerful technique for material characterization, especially for

micro-structural features. In a TEM, a beam of electrons is transmitted through an ultra thin specimen, interacting with the specimen as it passes through. An image is formed from the interaction of the electrons transmitted through the specimen; the image is magnified and focused onto an imaging device, such as a fluorescent screen, on a layer of photographic film, or to be detected by a sensor such as a CCD camera. Nowadays the TEM resolution can be pushed into the sub-angstrom regime.[2, 3]

TEM techniques involved in this dissertation can be summarized into three parts: (a) electron diffraction, (b) diffraction contrast, and (c) high-resolution (HR) imaging, which will be introduced in the following paragraphs.

When a wave passes through a periodic structure whose periodicity is of the same order of magnitude as the wavelength, the emerging wave is subject to interference, which produces a pattern beyond the object. In the same way, electrons can be diffracted by a crystal, and the pattern of spots gives information about the crystal lattice, including shape, orientation and the spacing of lattice planes. Taking wurtzite GaN as an example, Figure 2.4 shows the typical diffraction pattern (DP) along the $[11\bar{2}0]$ zone axis. Considering the structure factor for wurtzite GaN, (0001) diffraction is forbidden under the kinematical approximation. But it is often appears as a weak spot in this zone because of the double dynamically excited diffraction from allowed $(1\bar{1}00)$ and $(\bar{1}101)$ planes. However, it can never be excited by dynamic diffraction under $[1\bar{1}00]$ zone because it cannot be acquired by superposition of the allowed diffraction with this zone, as shown in Fig. 2.5.

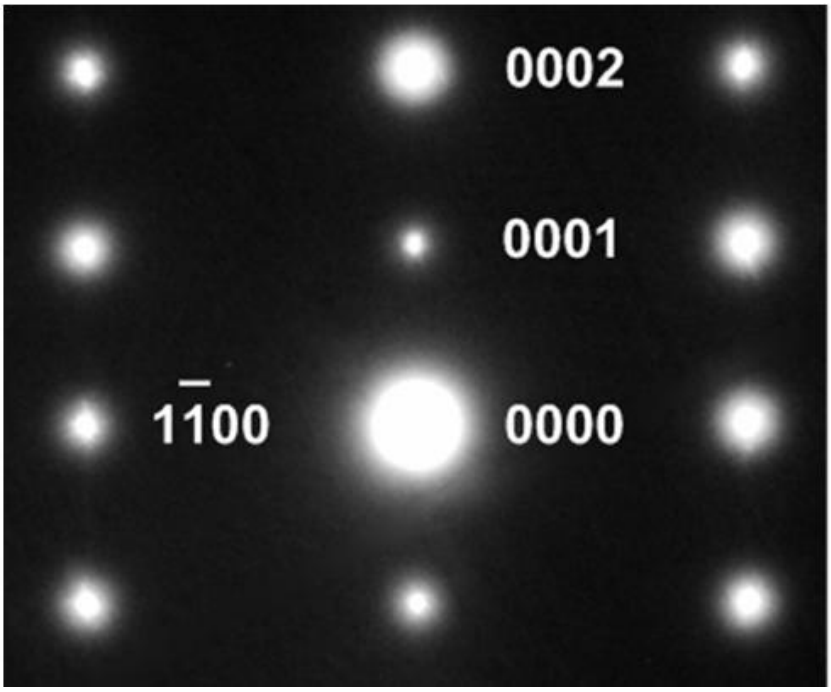

Fig. 2.4. Diffraction pattern of wurtzite GaN acquired along $[11\bar{2}0]$ zone axis.

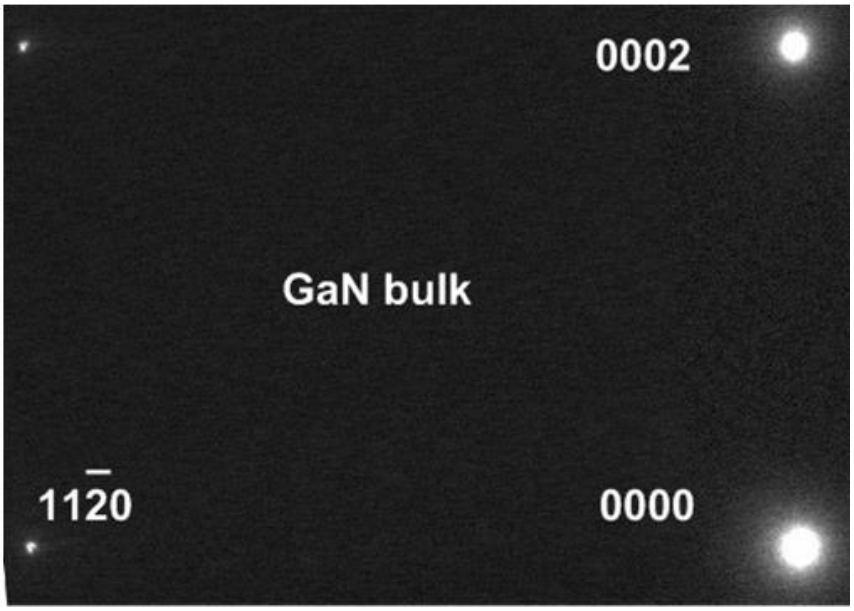

Fig. 2.5. Diffraction pattern of wurtzite GaN acquired along $[1\bar{1}00]$ zone axis.

Based on the diffraction conditions, another TEM technique called diffraction contrast is commonly used particularly in the investigation of crystal defects, such as dislocations, stacking faults, grain boundaries, and precipitates. Every defect can be characterized as a local displacement off the perfect crystal atom positions. The amplitude of the diffracted wave is sensitive to the displacement vector Δr and to the deviation parameter s (s indicates how much the diffraction vector is away from exact Bragg condition: $\Delta k = g$) as indicated in this following equation:

$$\psi_g \propto \sum_r f_{(r)} e^{2\pi i \Delta k r} = \sum_r f_{(r)} e^{2\pi i (g-s)(R+\Delta r)} \approx \sum_r f_{(r)} e^{2\pi i (g\Delta r - sR)}$$

By comparing the defected region with the perfect crystal matrix, the phase difference of $g.\Delta r$ will determine the image contrast of the defects. They are out of contrast when $g.\Delta r = 0$, which is the criteria usually used to determine the Burger's vector of dislocations.

For an improved visualization of dislocations, weak-beam dark-field (WB-DF) images are often adopted for producing sharp dislocation lines. The diffraction contrast depends on the deviation parameter s. The exact Bragg condition (s=0) is poor for imaging dislocations since diffraction contrast will be shown over a large area with a crystal plane distortion close to the dislocation core, causing a wide and fuzzy image of the dislocation.[5] A positive deviation vector is desired under which the diffraction contrast will be asymmetric around the dislocation core, and the darker contrast side in the dark-field image is indistinguishable with the background intensity. Therefore, the dislocations will appear as sharp bright lines in the weak-beam dark-field images.

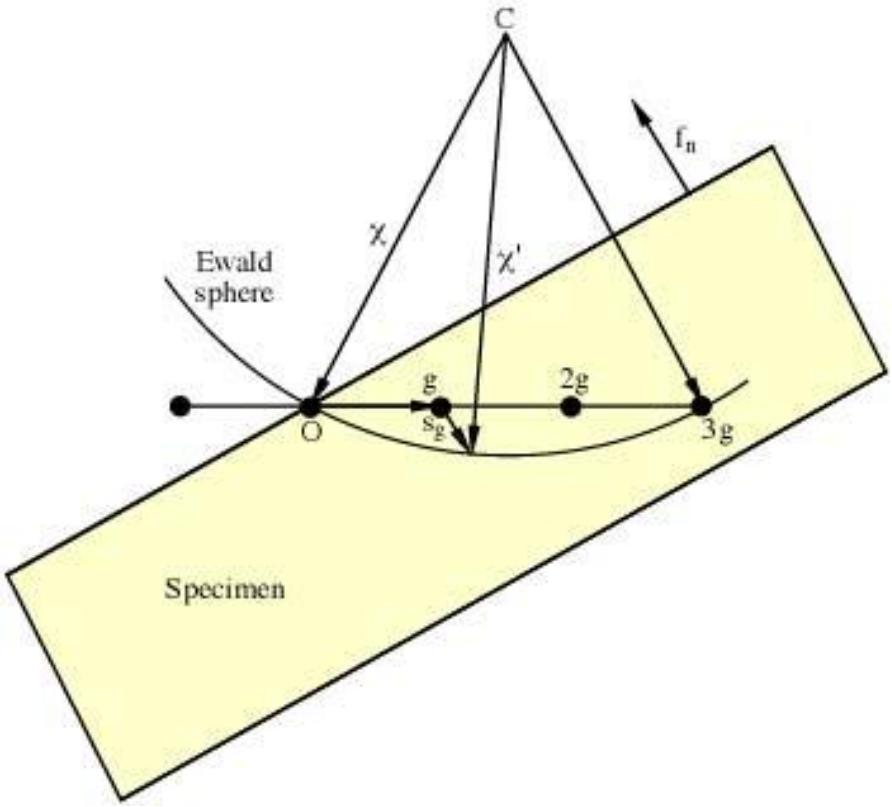

Fig. 2.6. Schematic diagram of g/3g WBDF condition. The vertical direction is the optic axis in the TEM.

In practice, g/3g weak beam condition is often used, which is illustrated in Fig. 2.6. To obtain this condition, the specimen is firstly tilted to a two-beam condition, where the g diffraction spot is strongly excited. Then the DF beam deflection coils are used to change the direction of incident beam, which is equivalent to rotating the Ewald sphere in reciprocal space until the 3g reflection spot is strongly excited while the g reflection spot on the optic axis becomes weak. Finally, an objective aperture is used to select the weak *g* beam to form imaging contrast. One limitation of the diffraction contrast technique is that the position of the dislocation image is not exactly the real position of dislocation core, because this contrast is rather a result of the variation of orientation of crystal planes around the defects than the defects themselves.

In order to directly visualize the structural nature of a crystal, high-resolution TEM (HRTEM) technique is often used, which allows imaging of the crystallographic structure at the atomic scale. When the incident beam passes through the specimen, as a result of the interaction with the sample, the electron exit wave function is determined by the atomic potential. The phase difference between the exit wave and the incident wave peaks at the location of the atom columns can be reconstructed to form the image wave in the imaging plane (films or CCD). However, it is important to realize, that the recorded image is not a direct representation of the samples crystallographic structure. The relationship between the exit wave and the image wave is highly related to the components of the microscope, described by the contrast transfer function:

$$CTF_{(u)} = A_{(u)}E_{(u)}\sin\left(\chi_{(u)}\right)$$

Here $A_{(u)}$ is the aperture function. $E_{(u)}$ is the envelope function. And $\chi_{(u)}$ is the function related to the aberrations of the electron optical system.

Both phase-contrast and diffraction-contrast images presented in this dissertation were recorded using either a JEOL JEM-4000EX high resolution electron microscope operated at 400 KV or a Philips CM200-FEG high resolution electron microscope operated at 200 KV.

2.2.3 SCANNING TRANSMISSION ELECTRON MICROSCOPY AND ENERGY DISPERSIVE X-RAY SPECTROSCOPY

A scanning transmission electron microscope (STEM) is also a type of TEM, which is distinguished from conventional TEM by focusing the electron beam into a narrow spot which is scanned over the sample in a raster manner. As sketched in Fig. 2.7, the image-forming lens focuses the electron beam to form an atomic scale probe at the

specimen, and two pairs of scan coils are used to raster the probe over the sample. When the focused electron beam pass through the thin sample, different types of signals can be generated. The transmitted electrons within a relatively low scattered angles (<10 mrad) with respect to the optic axis are used to form bright field images; scattered electrons at relatively high angles (~10-50 mrad) can be detected by an annular dark field (ADF) detector for form annular dark field images; while electrons scattered to even higher angles (~50 mrad) can form so-called high angle annular dark field (HAADF) images. X-ray generated from the interaction between the electron beam and sample is used to obtain energy-dispersive X-ray spectroscopy (EDS), providing information about the chemical formation and elemental distribution of the sample. There is another technique, called electron-energy loss-spectroscopy (EELS), used to extract information of local chemical variations by analyzing transmitted electrons that have lost measurable amounts of energy when passing through the sample.[6, 7]

Since HAADF images are formed by collecting incoherently scattered electrons at very high angles (~50 mrad), the image contrast is strongly dependent on the sample thickness and atomic number Z, so this technique is often referred as Z-contrast imaging. And the dependence of the imaging contrast to atomic number Z is in the form of $I \sim Z^{n}$, where the n is in the range between 1.6 and 1.9 depending on the inner and outer ADF detection angles.[8] The HAADF images and EDS spectroscopy reported in this dissertation were taken using an JEOL 2010 F TEM operated at 200 kV. The focused probe size was chosen to be 0.2 nm for STEM imaging mode, and the camera length was chosen to be 6 cm.

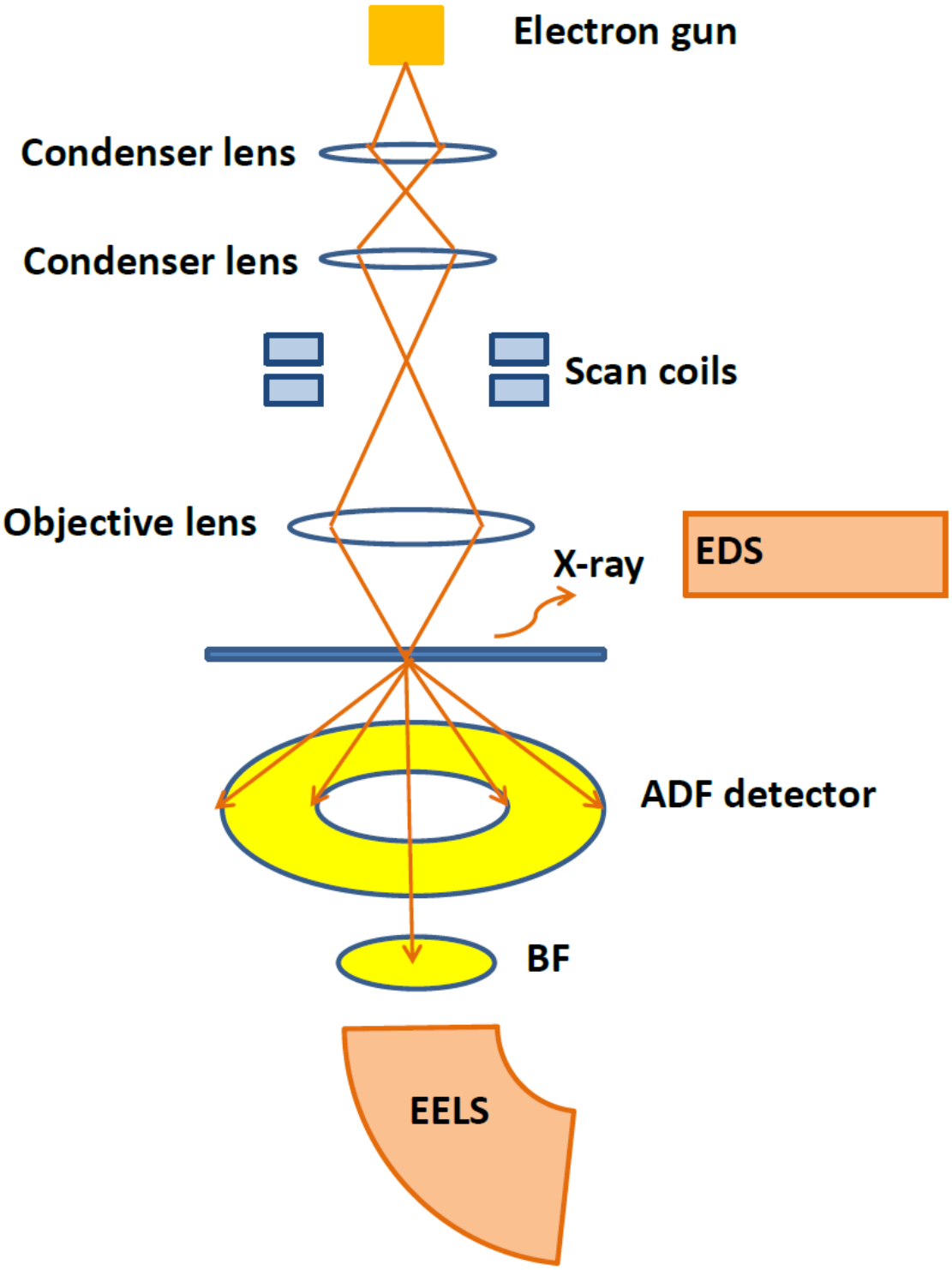

Fig. 2.7. Schematic diagram representing essential components of a STEM.

2.3 TEM SAMPLE PREPARATION

2.3.1 CONVENTIONAL SAMPLE PREPARATION

For cross-sectional TEM observation, TEM foils have to be firstly prepared. In this dissertation, TEM samples described in chapter 5 and 6 are prepared using conventional methods-wedge polishing and dimpling.

As to wedge polishing, samples were cut into slabs with sizes of about 2.5mm × 1.5mm using a diamond blade, then the two pieces were glued together using M-bond, with the expitaxial film layers facing each other. Mechanical polishing was first operated on one side successively using 30, 9, 6, 3, 1 and 0.5 μm diamond lapping films until this side was smooth without any scratches. After that, the other side was polished using the same lapping film sequence in addition to the introduction of a 2° wedge angle when changing to the 9 μm lapping film. Mechanical polishing was stopped when the thin area started showing fringes and both sides were scratches-free. The samples were then glued to the copper grids suitable for the TEM sample holder. Finally, the specimens were thinned by argon ion-milling at 3.5~4.0 keV followed by a low energy cleaning at ~2 keV, using double-mode of the Gatan Model 691 precision ion polishing system (PIPS). A liquid-nitrogen-temperature cooling stage was used for some materials to minimize any thermal or ion-beam damage.[9]

As to dimpling, samples were also cut into slabs with sizes of about 2.5mm × 1.5mm using a diamond wafer blade. Then the four slabs were glued together using M-bond, with face-to-face expitaxial film layers. Mechanical polishing successively using 30, 9, 6, 3, 1 and 0.5 μm diamond lapping films on both sides, followed by dimpling using a copper wheel first then cloth wheel, typically reduced the sample thicknesses to ~

10 μm. Then the 10 μm pieces were glued to copper grids for final thinning by PIPS at 3.5 keV followed by a low energy cleaning at ~2 keV, until small holes were formed in the films. A liquid-nitrogen-temperature cooling stage was used to minimize any thermal or ion-beam damage.

2.3.2 FOCUSED ION BEAM

Focused ion beam (FIB) technique was also used for TEM cross-sectional sample preparation on the nanoindented and nanoscratched samples in Chapter 3, 4 and 5. Most instruments combine the scanning electron microscope (SEM) with the FIB column, forming the so-called "Dual Beam" systems. The FIB system uses a Ga^+ ion beam to raster over the surface of a sample in a similar way as the electron beam in a SEM. The generated secondary electrons (or ions) are collected to form an image of the sample surface. The major advantages of FIB over conventional TEM specimen preparation methods are that samples can be extracted from specific regions, and large uniform thin areas can be obtained. However, the energetic Ga^+ ion-beam induces sample damage in FIB-prepared TEM samples. Ga^+ ions can be implanted into the TEM specimen, which would affect the local chemical composition of the material. Also this kind of implantation can introduce critical amorphization of the TEM specimen surface.[10]

Sample preparation by FIB in this dissertation was performed in an FEI Nova 200 system. A ~1 μm-thick platinum layer was first deposited over the area of interest to prevent ion damage, as illustrated in Fig. 2.8. The piece was lifted out with an Omni probe. After that, this piece was attached to the copper grid followed by further thinning with successively decreasing current (from 7 nA to 0.1 nA in steps). Low-energy low-

current milling (5 kV, 45 pA) was operated to the specimen during the final stage of milling. Typically the FIB-prepared XTEM sample has a thickness of less than 100nm.

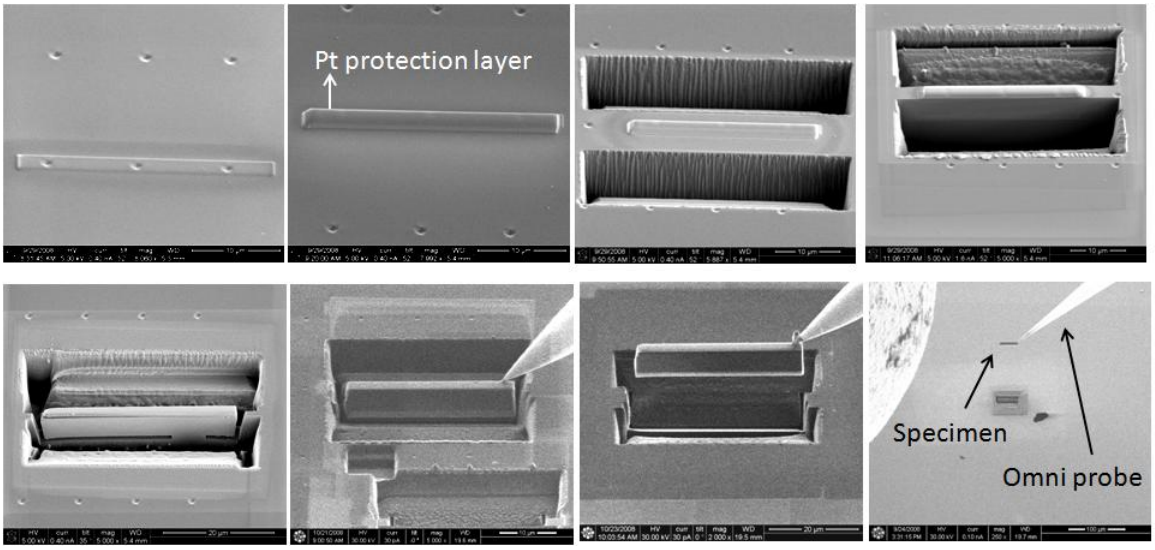

Fig. 2.8. A series of SEM images showing the procedure of TEM sample preparation by FIB.

REFERENCES

[1] B. G. Yacobi and D. B. Holt, *Cathodoluminescence Microscopy of Inorganic Solids* (Plenum Press, New York, 1990).

[2] P. E. Batson, N. Dellby, and O. L. Krivanek, Nature **418**, 617 (2002).

[3] D. J. Smith, Materials Today. **11**, 30 (2008).

[4] F. A. Ponce, D. P. Bour, W. T. Young, M. Saunders, and J. W. Steeds, Appl. Phys. Lett. 69, 337 (1996).

[5] B. Fultz, and J. M. Howe, *Transmission electron microscopy and diffractometry of materials*, 2nd edition. (New York, Springer, 2001), p. 362.

[6] D. B. Williams, and C. B. Carter, *Transmission Electron Microscopy*, (Springer, 1996), chapter 38, p. 655-663.

[7] P. D. Nellist, *Scanning Transmission Electron Microscopy: Imaging and Analysis*, (Chapter 2, Springer, 2011), chapter 2, p. 91-116.

[8] P. Hartel, H. Rose, and C. Dinges, Ultramicroscopy **63**, 93 (1996).

[9] C. Z. Wang, D. J. Smith, S. Tobin, T. Parodos, J. Zhao, Y. Chang, and S. Sivananthan, J. Vac. Sci. Technol. A **24**, 995 (2006).

[10] L. A. Giannuzzi, and F. A. Stevie, Micron **30**, 197 (1999).

CHAPTER 3

NANOSCALE DEFORMATION OF INP SINGLE CRYSTALS BY SCRATCHING WITH AN ATOMIC-FORCE MICROSCOPE TIP

This chapter presents the microstructure of (001) InP crystals scratched in an atomic force microscope with a diamond tip as a function of crystallographic direction and applied normal force, in order to understand the deformation mechanism of zinc-blende structure at the nanometer scale. This work was carried out in collaboration with Prof. Rodrigo Prioli and colleagues at Universidade Católica do Rio de Janeiro. The nano-scratching and AFM imaging were performed by Paula Galvão Caldas and C. M. Almeida at Universidade Católica do Rio de Janeiro. My role in this work involved micro-structural characterization using focused ion beam and transmission electron microscopy, and analysis of the deformation mechanism. The major results of this study have been published. *

(*) J. Y. Huang, F. A. Ponce, P. G. Caldas, C. M. Almeida, and R. Prioli, "*Microstructure of nano-scratched semiconductors*", J. Phys.: Conf. Ser. **326**, 012061 (2011)

3.1 INTRODUCTION

Achieving control of matter at the atomic scale is of major importance for nanotechnology applications. By the controlled introduction of defects, materials properties of technological importance can be modified at the nanometer scale. Indentation techniques allow the introduction of plastic deformation at specific locations in a crystal, and recent reports indicate that nanoscale lithography on semiconductors by indentation techniques causes site-selective growth of nanostructures.[1-5] It has been observed that nucleation of nanocrystals is achieved by the presence of dislocations generated by the indentation, rather than by the morphology of the indentation pits.[6] It thus becomes necessary to understand at the nanometer scale the indentation process and the nature of the resulting crystal defects. To achieve this objective, the atomic force microscope (AFM) and nano-indenter testing instruments have been used to apply measureable forces on regions with atomic scale dimensions.[7-9] By regulating the force exerted by the indenting tip, dislocations are controllably introduced by slip over nanometer-scale lengths. The introduction of crystal defects modifies the local microstructure, which can be studied by cross-section transmission electron microscopy (TEM). The availability of focused ion beam (FIB) milling has allowed the production of thin TEM foils containing the indented region. TEM observations of indentations using micron size tips in Si, InP, GaAs and GaN have been reported, where the deformation happens by slip on the {111} planes of the diamond and zinc blende structures, and on the $\{1\bar{1}01\}$ and {0001} planes in the wurtzite structure.[10-14]

The availability of AFM tips with radius of curvature of less than 100 nm opens the opportunity to study the defect structure generated within very small volumes.

Taking advantage of controllable lateral movement in the AFM, scratching with the tip provides another method of achieving nano-scale deformation. By applying a normal force with a stationary tip, while the crystal is being moved with constant speed in a specific direction, linear arrays of crystal defects can be controllably introduced.[15] Dislocations have been found to be confined in a well-defined volume below the scratch, and to act as nucleation sites for growth of linear arrays of nanocrystals.[16] Some recent studies show that crystalline defects introduced by nanoindentation and nanoscratching are different in nature,[17] but the deformation mechanisms in nanoscratching have been hardly explored. We report here on a study of the structural properties related to elastic and plastic deformation resulting from nanoscratching (001) surfaces of InP crystals. We have performed nanoscratches using a sharp AFM tip, under various applied normal forces and along different crystalline directions to analyze the nanoscale deformation mechanisms in the zinc blende crystal structure.

3.2 EXPERIMENTAL DETAILS

The crystals used in this study were produced by growing an InP epilayer with a thickness of 500 nm by metal organic vapor phase epitaxy at 630 ℃ and 50 mbar, on epi-ready wafers of semi-insulating (001) InP. The InP film was grown with the purpose of minimizing surface damage resulting from wafer cutting and polishing. An AFM equipped with a nanoindentation cantilever was used to scratch the surface along the <100> and <110> crystal directions, producing a periodic array of scratches with applied normal force values of 7.5, 15, 30, 60, and 120 μN. The scratching velocity was kept constant at 120 m/s. The cantilever made of stainless steel was 400 μm in length with an elastic constant of 310 N/m. It makes an angle of 12 degrees with the cantilever holder.

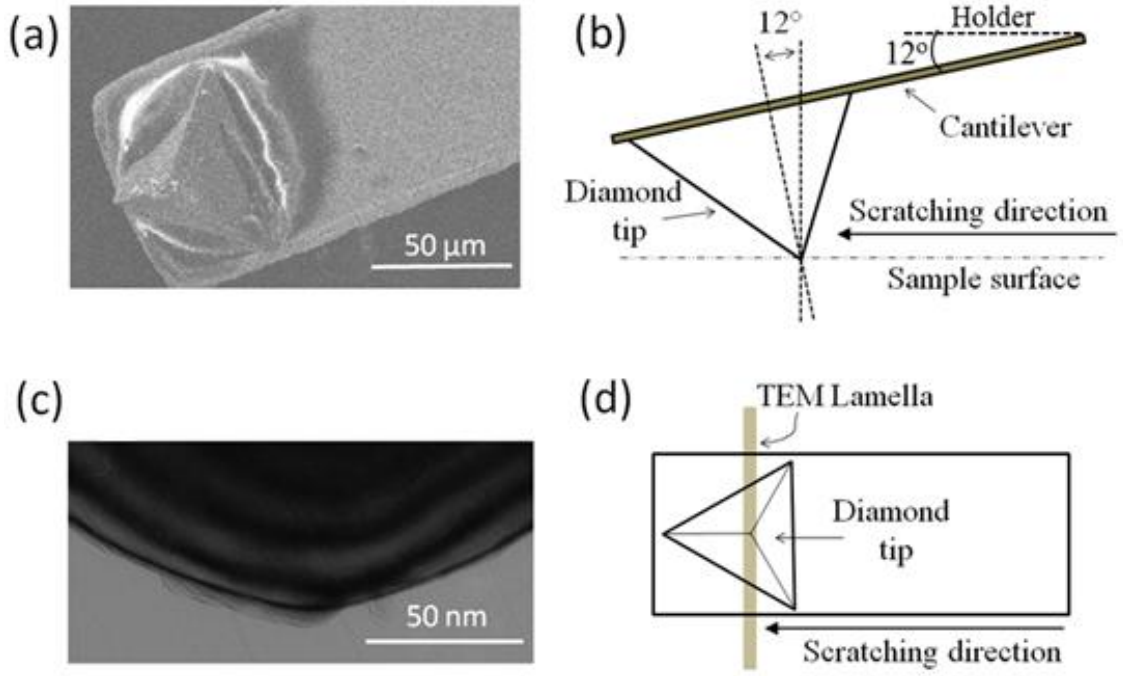

Fig. 3.1. Configuration of the AFM tip used in this study. (a) Secondary electron image of portion of the cantilever that includes the diamond tip. (b) Schematic side view of the tip geometry during scratching. (c) TEM image of the contact area of the AFM tip, viewed along the cantilever length projection. (d) Schematic representation of the TEM lamella sectioning in relation to the AFM tip configuration.

A diamond crystal tip was mounted at one end as shown in Fig. 3.1(a). The diamond tip has an elliptical shape with radii of curvature of ~ 60 nm and ~120 nm along the minor and major axes, respectively. The major axis is parallel to the scratch direction. A schematic lateral view of the diamond tip setting is shown in Fig. 3.1(b**).** Figure 3.1(c) is a TEM image of the diamond tip taken perpendicular to the cantilever length, showing the shape of the tip normal to the scratch direction. The buckling of the tip during a scratch was of the order of arc-seconds for the range of applied forces used in this study. Under similar conditions, interaction between parallel scratches was observed to lead to hardening for scratch separations of less than 80 nm, in this range of applied forces.[18]

In order to minimize the interaction between adjacent scratches we have used a scratch separation of ~ 700 nm. Thin lamella of the scratched semiconductor crystal were prepared in cross-section for TEM, using a focused ion beam (FIB) in a Nova 200 UHR FEG (FEI) system, for projected views along the direction of the scratch lines as shown in Fig. 1(d). A layer of platinum, about 1 μm thick, was deposited over the surface of the scratched region of the semiconductor for protection from damage during the ion beam milling process. The deepest scratches at 120 μN were readily observable in secondary-electron images, and thus were used as reference for the lift out process by FIB, in order to produce a region with 5 μm in width that covered a full period of scratches. The microstructure of scratched crystal was studied by diffraction contrast TEM using a JEOL 4000EX instrument operated at an accelerating voltage of 400 kV and a Philips CM200-FEG system operated at an accelerating voltage of 200 kV.

3.3 RESULTS

3.3.1 MICROSTRUCTURE OF SCRATCHES ALONG <110> ORIENTATION

Figure 3.2 shows the surface morphology as observed by AFM and the microstructure by TEM of a sequence of scratches parallel to a <110> direction with different normal forces. The top AFM image shows that the scratch depth increases with the normal force, and pile-ups distributed asymmetrically on the sides of the scratch. Using diffraction contrast as shown in the bottom TEM image, we observe scratch-generated dislocations for forces of 15 μN and above. The 7.5 μN scratch shows no defect contrast, which indicates that only elastic deformation occurs with no residual impression on the surface, consistent with the AFM image.

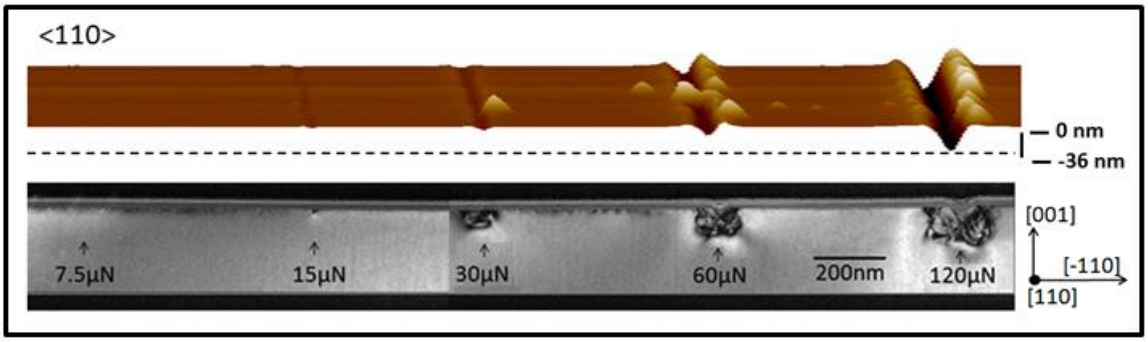

Fig. 3.2. Morphology and microstructure of the scratches along <110> direction under applied normal forces of 7.5, 15, 30, 60, and 120 μN. (top) AFM profiles showing the surface morphology. (bottom) Diffraction-contrast TEM image taken in cross-section under $\boldsymbol{g}$ = (002). The horizontal scale is the same for the AFM and TEM images.

To see the defects more clearly, images shown in Fig. 3.3 were taken at higher magnification of the same scratches providing more details about the defect microstructure for forces increasing from 15 μN to 120 μN. It is observed that dislocations appear below the scratch when using forces of ~15 μN and higher. This is related to a critical shear stress for plastic deformation for the crystal slip systems. At a normal force ≥ 30 μN, an inverted triangular region with high density of defects is observed right below the tip contact region, and beside the triangular region quasi-symmetric dislocation bands were observed. At higher loads, the dislocations propagate deeper into the material and the size of the inverted triangular region and quasi-symmetric dislocation patterns become larger. The shapes of the defect region always look similar and the width of the inverted triangular region follows the curvature of the contact region between the AFM tip and the InP surface. Neither cracks nor fracture has been observed for any scratch in our study. At a load of 120 μN, surface discontinuities are observed at the intersections of the triangular region and the surface, namely a "pop-up" event.

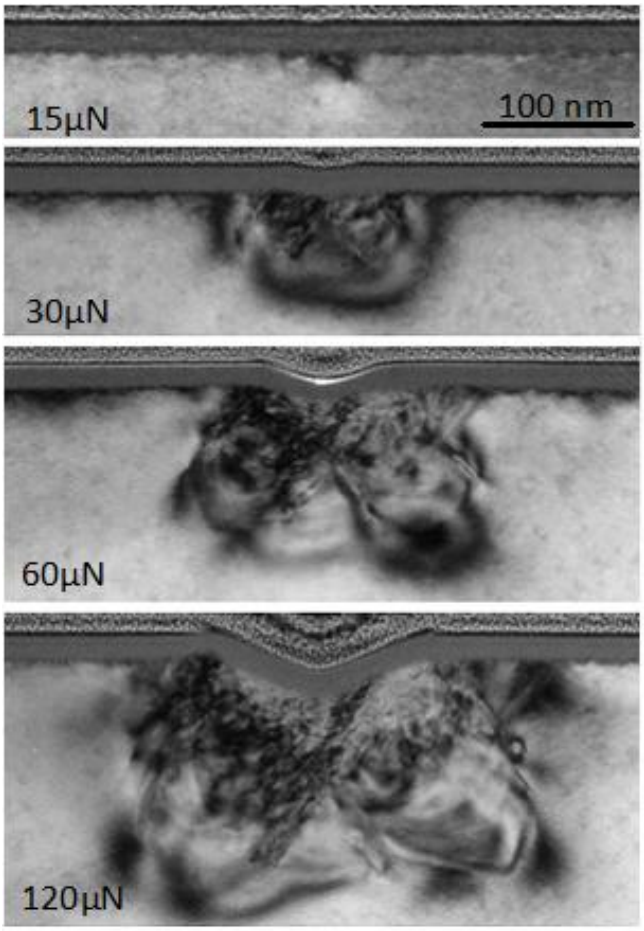

Fig 3.3. Bright-field cross-section TEM images of <110> scratches using different applied normal forces, under $\boldsymbol{g}$ = (002). Under this diffraction condition, all dislocations lying on {111} planes are visible. The InP crystal is covered by a 25 nm thick layer of amorphous carbon followed by platinum. The morphology of the platinum follows the InP surface.

To identify the nature of dislocations generated by the <110> scratching, a series of TEM images were taken under different diffraction conditions. Figure 3.4 shows the microstructure characteristics of a scratch with an applied force of 120 μN. In Fig. 3.4(a) corresponding to diffraction conditions $\boldsymbol{g}_1 = (1\bar{1}1)$ the presence of deep dislocation loops on the right and shallow loops on the left is noticeable. Similarly in Fig. 3.4(b) under $\boldsymbol{g}_2 = (\bar{1}11)$ deep loops to the left and shallow ones to the right are observed; while all loops are visible under $\boldsymbol{g}_3 = (2\bar{2}0)$ in Fig. 3.4(c). The TEM diffraction contrast of a dislocation

with Burgers vector $\boldsymbol{b}$ becomes invisible when $\boldsymbol{g}.\boldsymbol{b} = 0$. Therefore, we can conclude that the deep loops on the right and the shallow ones on the left in Fig. 3.4(a) have Burger's vectors that lie in the $(\bar{1}11)$ plane. The Burger's vectors of the deep loops on the left and the shallow ones on the right in Fig. 3.4(b) lie in the $(1\bar{1}1)$ plane. The main slip system in the FCC lattice is <110>{111}, so the Burger's vector of the dislocations loops are of the 1/2<110> type lying on the $(1\bar{1}1)$ and $(\bar{1}11)$ planes. The dislocation density in the inverted triangular region is significantly higher, so it is difficult to image them individually in order to determine their nature. Nevertheless, they should be associated with the interaction of loops on different {111} slip planes, which will be discussed later.

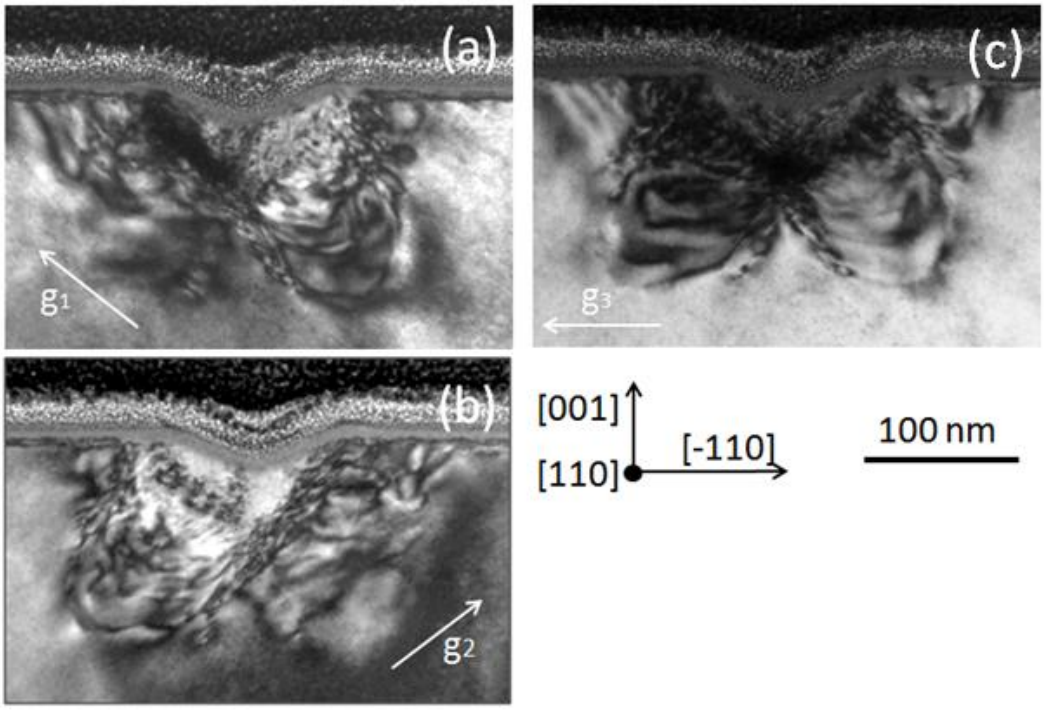

Fig. 3.4. Bright-field images of the <110> scratch with F = 120 μN, taken with various diffraction conditions: (a) $\boldsymbol{g}_1 = (1\bar{1}1)$, (b) $\boldsymbol{g}_2 = (\bar{1}11)$, (c) $\boldsymbol{g}_3 = (2\bar{2}0)$.

3.3.2 MICROSTRUCTURE OF SCRATCHES ALONG <100> ORIENTATION

To learn about the dependence of the microstructure on the scratch direction, scratches along the <100> crystal direction were also studied. Figure 3.5 shows the surface morphology as observed by AFM and the microstructure by TEM of a sequence of scratches parallel to a <100> direction under various normal forces. The top AFM image shows that the scratch depth increases with the normal force, and the development of a smooth pile-up on both sides of the scratches that become prominent at higher normal forces. The TEM image on the bottom shows no visible contrast for scratches with applied normal forces of 7.5 and 15 μN, with the onset of plastic deformation occurring at ~ 30 μN instead of ~ 15 μN as observed in the <110> case.

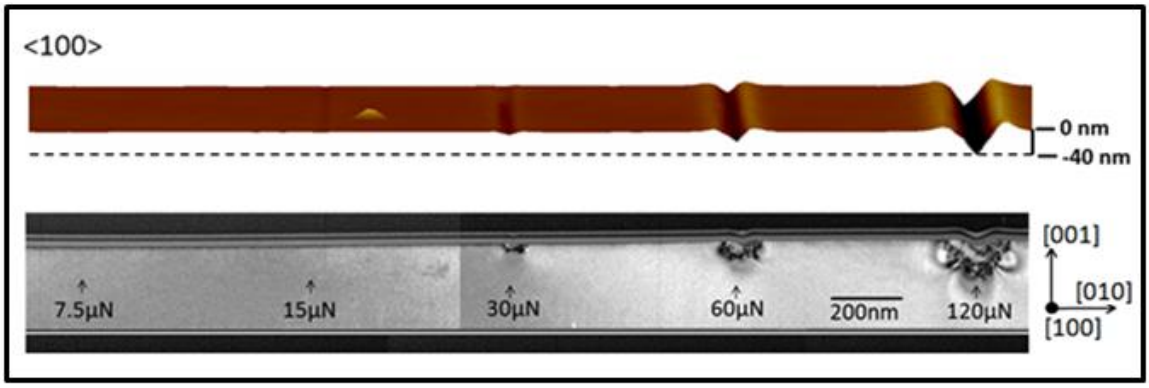

Fig 3.5. Morphology and microstructure of the scratches along a <100> direction under the various applied normal forces. (top) AFM profiles showing the surface morphology. (bottom) Diffraction-contrast TEM image taken in cross-section under $\boldsymbol{g}$ = (002). The horizontal scale is the same for the AFM and TEM images.

Figure 3.6 shows cross-section TEM images of scratches along the <100> orientation taken at a higher magnification, with applied normal forces increasing from 15 μN to 120 μN. Unlike the <110> scratches in Fig. 3.3, in which the defect regions keep the same pattern when the applied normal force increased from 30 to 120 μN, the defect regions generated by <100> scratches display different patterns. When the applied

normal force is 30 μN, the defect region consists of two triangular arms as observed in Fig. 3.6. The long sides of these two triangles form an angle of ~ 27 ºwith the surface. With increasing normal force, the defect region turns out to be a single inverted triangle, whose sides are observed to make an angle of 45 ºwith the surface, which is observed to dominate the image contrast at 120 μN. This change of defect morphology should be associated with the force interaction to the crystal structure during scratching, which will be discussed later. No "pop-up" event has been observed at any force for scratches along the <100> direction. The scratching surface is always smooth without any discontinuity. Material pileup on both sides of the scratch, and a high stain field under the two sides of the scratch are observed.

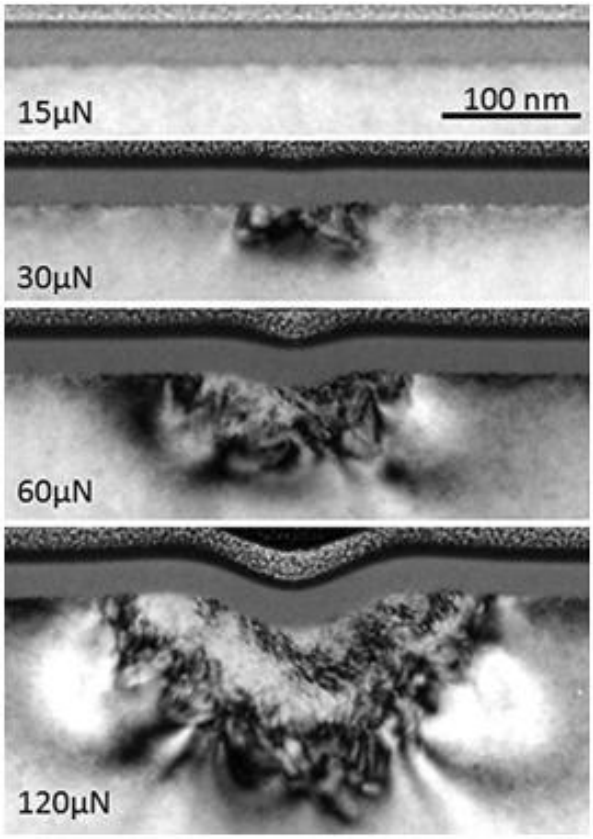

Fig. 3.6. Bright-field cross-section TEM images of <100> scratches using different applied normal forces, taken at higher magnification under $\boldsymbol{g}$ = (002).

As with the <110> scratches, a series of TEM images were taken from a <100> scratch with the highest normal load under different diffraction conditions, the results are shown in Fig. 3.7. We observe many short dislocation segments and small loops. The ***g.b*** analysis shows that these segments and loops are mostly visible when they are along the ***g*** direction and becomes invisible when they are perpendicular to the ***g*** direction, indicating that these dislocations are also mostly of screw type.

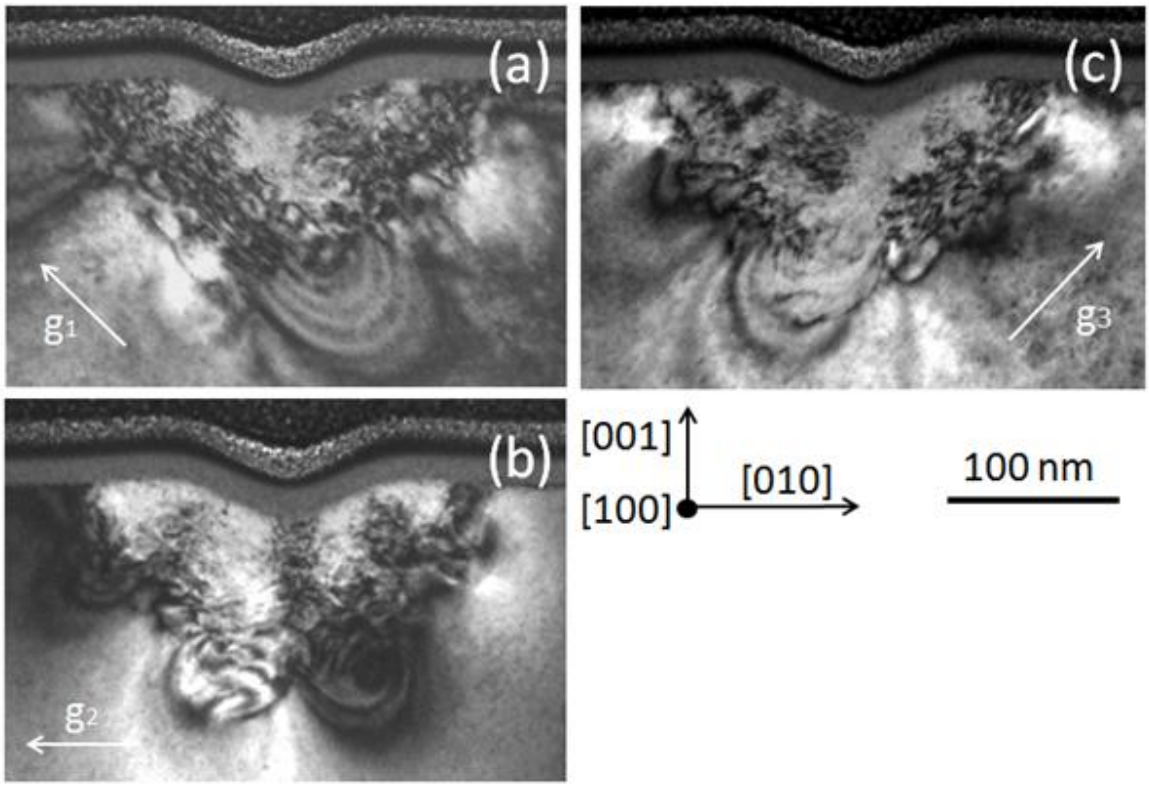

Fig. 3.7. Bright-field TEM images of the <100> scratch with F = 120 μN, taken under various diffraction conditions: (a) $\boldsymbol{g}_1 = (0\bar{2}2)$, (b) $\boldsymbol{g}_2 = (0\bar{2}0)$, (c) $\boldsymbol{g}_3 = (022)$.

3.4 ANALYSIS AND DISCUSSION

3.4.1 NORMAL VERSUS LATERAL FORCES DURING NANOSCRATCHING

The onset of plastic deformation, defined as the nucleation of the first dislocation, is found to depend on the direction of motion of the tip, as observe for our (001) InP case in Figs. 3.2 and 3.5. It happens at a normal force of ~ 15 μN for the <110> case, and at ~ 30 μN for the <100> case. The defect structure is a result of normal and lateral forces acting together on the crystal surface. The applied normal force by itself results in an indentation pit due to atomic scale slip events consisting of dislocation generation and propagation as the surface of the crystal conforms to the tip shape. These dislocations form a work-hardened region with an inverted pyramidal shape and a high density of dislocation loops immediately below the tip.[23] The hardened pyramidal region acts as an effective tip generating elongated dislocation loops in symmetric bands that propagate deep into the crystal. From this perspective, the contribution of the normal force to the scratch morphology is expected to be independent of the scratch direction. On the other hand, motion of the tip generates a lateral force that consists of two parts. One is the frictional force between the tip and the surface, and the other is associated with the conformity of the surface of the crystal to the curvature of the tip. For low values of the normal force, the lateral force is of a frictional character, and the effect on the crystal is elastic deformation and heat generation. At sufficiently high normal forces, the critical shear stress for plastic deformation is exceeded, and the surface begins to conform to the tip shape by the slip of crystal planes. In order to adapt to the curvature of the tip, the lattice planes must glide and create steps at the surface; steps that accommodate the surface to the shape of the tip (equivalent to a lateral indentation). During this process, in addition to the frictional character, the lateral force starts plowing into the material, leaving a groove along the scratch line and pile-ups on both sides of the groove and on

the front side of the tip. At higher normal forces, hardening of the crystal takes place, leading to possible fracture, with the formation of cracks and powder-like particles that get detached from the crystal. At even higher normal forces, plowing of the crystal will lead to significant fracture and breakage.

3.4.2 CONTACT AREA DURING SCRATCHING

Understanding the nature of the contact area is important in the discussion of plastic deformation due to scratching. A schematic diagram of the scratch geometry is shown in Fig. 3.8. For a rigid crystal, only the forward part of the tip contacts the surface during the scratch. In the elastic-plastic case, however, the contact area between the tip and the crystal depends on the amount of elastic recovery at the rear of the tip. This has been simulated by finite element modeling for scratches on elastic and perfectly plastic materials.[24] In a first approximation, for the case of pure plastic deformation, the subsequent elastic recovery at the rear of the tip can be neglected, and it can be assumed that in the case of InP the major contact with the crystal surface is at the front section of the tip. Values of the contact area and normal stress calculated in this manner are shown in Table 3.1. In the <110> case, for example, for a semispherical contact area with radius R = 60 nm and an applied normal force FN = 60 μN, the penetration depth is h ≈ 11 nm, the contact area $A = \frac{1}{2} \pi hR \approx 2{,}100\ nm^2$, and the normal stress $\sigma = FN/Ap \approx 32$ GPa. Here only results for FN =30, 60, and 120 μN are shown because there was no significant plastic deformation observed at lower loads. Comparing the data in Table 3.1, for a given normal force we observe smaller penetration depth in the <100> case that leads to smaller contact area and larger normal stress. This can be attributed to hardening of the surface due to locking of dislocations.

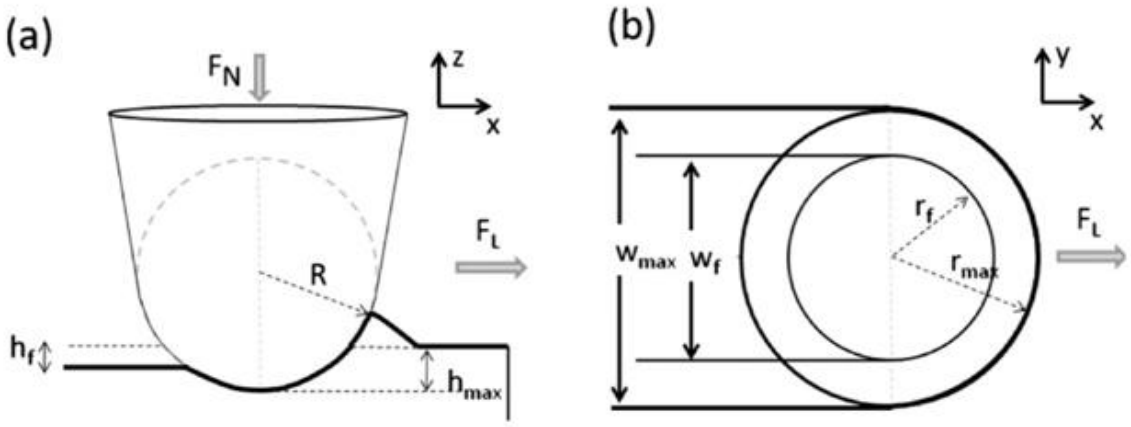

Fig. 3.8. Schematic diagram of the scratch geometry. R is the radius of the tip, F_N is the applied load, F_L is the lateral force, h_{max} is the maximum scratch depth, h_f is the final depth. (a) Cross sectional view showing change in surface height with a pileup in front of the tip. (b) Plane view showing the maximum contact radius r_{max} achieved at the maximum scratch depth and the final scratch radius after elastic recovery.

TABLE 3.1.
Contact area and normal stress for <110> and <100> scratches.

<110> Case

Normal Force (μN)	penetration depth (nm)	contact area (nm^2)	normal stress (Gpa)
30	3.2	602	50
60	11.1	2091	32
120	34.8	6560	25

<100> Case

Normal Force (μN)	penetration depth (nm)	contact area (nm^2)	normal stress (Gpa)
30	1.6	595	51
60	9.6	1809	36
120	25.6	4820	31

For a semispherical contact area with radius R, applied normal force F_N, with a penetration depth h, the contact area is $A = ½ \pi.R.h$, the projected contact area is $A_p = ½ \pi (R^2 – (R - h)^2)$, and the normal stress is $\sigma = F_N / A_p$.

3.4.3 ONSET OF PLASTIC DEFORMATION

The stress distribution associated with forces applied by the tip can be estimated using finite element modeling that take into account rheological aspects of the deformation. Ignoring the plastic deformation effects, the stress applied by the tip causes a maximum shear stress at a certain distance from the tip/crystal contact. A calculation shown in Fig. 3.9, which simulates an indentation using a tip of radius 60 nm with an applied force of 120 μN, gives a maximum value of the maximum shear stress at ~22 nm below the tip. A more detailed analysis requires consideration of the crystal nature of the material, namely the slip systems, and more specifically the component of the force along the slip directions. The critical shear stress in the bulk (away from the surface) has been calculated for the elastic-plastic case to be 2.5 GPa,[21] and for a pure-plastic case that includes dislocation generation at the surface to be 1.3 GPa.[25]

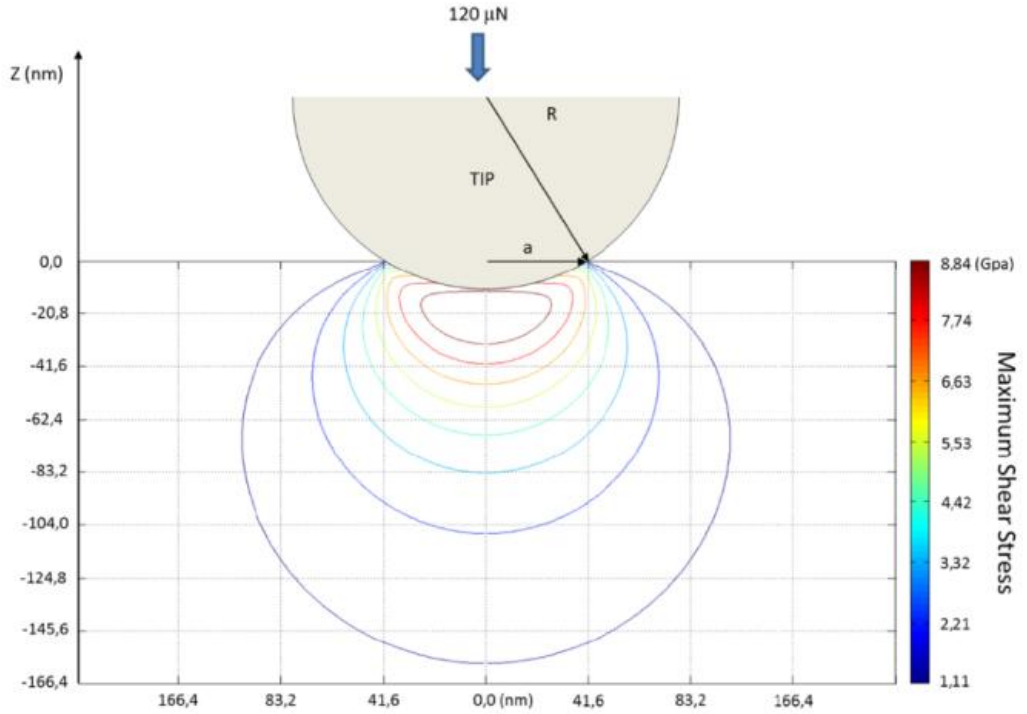

Fig. 3.9. Maximum shear stress distribution for an indentation with load of 120 μN.

It is of interest to know the dependence of the resolved shear stress on the direction of the applied lateral force. An analysis of the stress fields associated with scratching brittle materials has been reported by Ahn et al.[26] An analysis of the scratch contact area for an elastic and perfect-plastic material with a Berkovich tip has been reported by Bucaille et al.[24] The distribution of the maximum shear stress inside the bulk and at the surface of the scratch has been simulated by Wasmer et al.[21] Here a simpler approach was used by considering the projection cosine of the lateral force in the direction of the displacement (Burgers) vector. In other words, we consider the component of the lateral force along the possible <110> directions associated with elemental plastic events. These possible <110> lattice displacements for the [110] and [100] scratches are illustrated in Fig. 3.10, and the corresponding projection cosines are shown in Table 3.2.

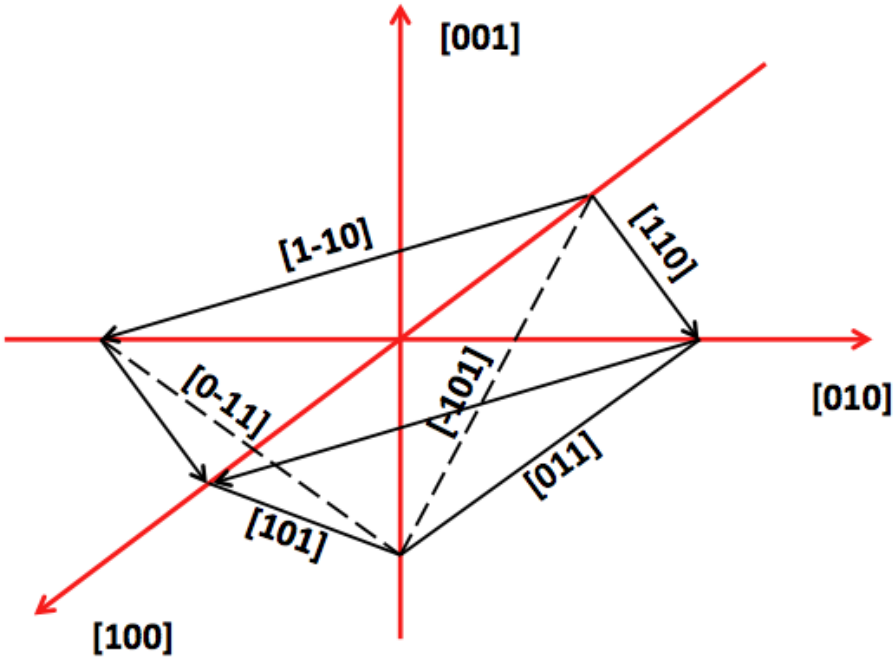

Fig. 3.10. Possible <110> lattice displacements in a zinc bende structure during scratch.

TABLE 3.2.
Projection cosine of the applied lateral force along the direction of displacement. The projection cosine **S.b**/|**S**||**b**| is shown for the possible displacement directions (**b**) along the indicated scratch directions (**S**).

Slip Direction	[110] scratch	[100] scratch
$[1\bar{1}0]$	0	$1/\sqrt{2}$
$[110]$	1	$1/\sqrt{2}$
$[101]$	$1/2$	$1/\sqrt{2}$
$[011]$	$1/2$	0
$[\bar{1}01]$	$-1/2$	$-1/\sqrt{2}$
$[0\bar{1}1]$	$-1/2$	0

For a [110] lateral force, a displacement parallel to the force has a cosine of one, while displacements along the other four oblique <110> directions have a cosine of ½. The displacement parallel to the lateral force will generate a lattice rotation about the [001] direction in the vicinity of the scratch, and should be associated with the introduction of mostly screw dislocations. [15] At the point of intersection of the rotating regions, the crystal displacement is along the same direction, with no opposing motion. The other active displacements are $[\bar{1}01]$ and $[0\bar{1}1]$ into the crystal (projection cosine -

1/2) leading to hardening, while [101] and [011] are out of the crystal (projection cosine +1/2) causing pile-up in front and on the sides of the tip. For a [100] lateral force, the projection cosine of the lateral force in Table II has the same absolute value along four <110> directions and it is zero for the other two <110> directions. The displacements along $[1\bar{1}0]$ and [110] result in motion away from the tip leading to coherent pile-up on the sides. The [101] displacement is capable to producing pile-up in front of the tip, while the $[\bar{1}01]$ displacement leads to compression into the material.

3.4.4 SURFACE MORPHOLOGY CAUSED BY SCRATCHING

The AFM and TEM images in Figs. 3.2 and 3.5 indicate that the surface morphology of a scratch consists of a groove in the middle and pile-ups on both sides. Asymmetry in the pile-ups is sometimes observed for both the <110> and <100> cases, with one side of the scratch showing different pile-up heights than the other. This is thought to be due to a slight misalignment of the tip in the scratch direction.[21] The misalignment may be due to the geometry of the tip/cantilever assembly and/or to instabilities in tip orientation during the scratch. In fact, a symmetric position of the tip should be unstable, since it would tend to simultaneously generate glide on symmetric slip planes, resulting in the locking of dislocations (hardening) in the vicinity of the surface. A slight tilt of the tip favors plastic deformation along one of the slip planes instead of the other, thus reducing the hardening effects and facilitating the scratch progress. In the <110> scratches of Fig. 3.2, the pile-ups are discontinuous, with irregular protrusions, suggesting that they are the result of significant displacements that relax the strain. These are pop-in and pop-out events, with displacements into and out of the crystal surface, respectively. After one such relaxation event, it takes some motion of

the tip to restore the strain necessary for the following event. On the other hand, in the <100> scratches of Fig. 3.5, the pile-up is continuous, with a smooth surface and no observed bumps in the direction of the scratch; which, as describe earlier, we interpret as due to hardening associated with the nature of the slip systems.

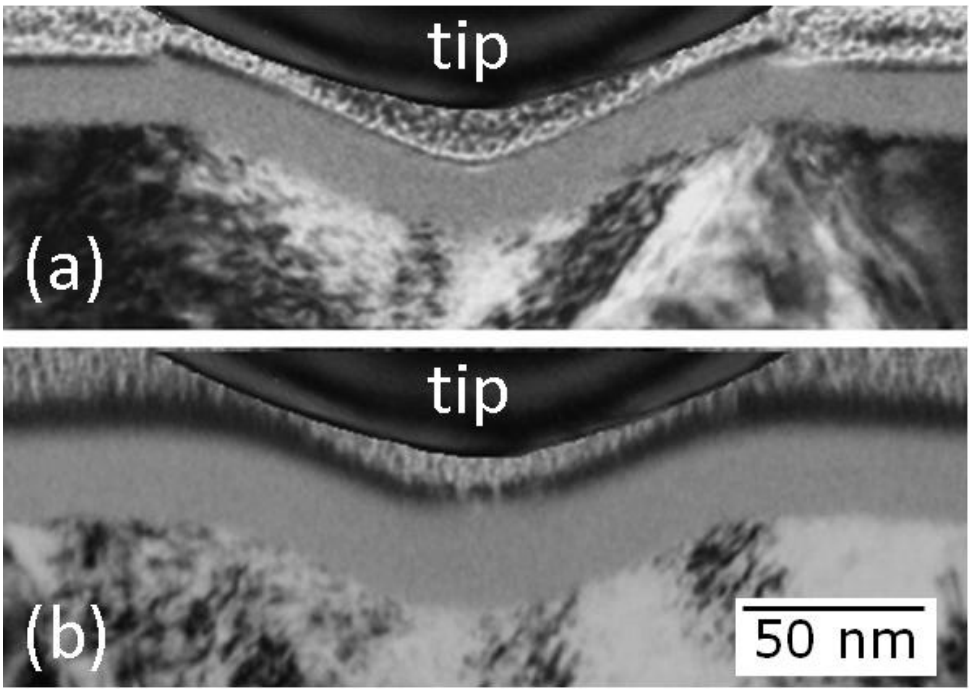

Fig. 3.11. The surface morphology of the (a) <110> and (b) <100> scratches are compared with the shape of the diamond tip used in the scratch. The TEM images of the tip and of the pit were obtained separately in each case.

Furthermore, as observed in 3.11, which shows magnified images of the scratches in both direction with a normal force of 120 μN, with a superimposed TEM image of the tip, the groove profile conforms to the tip shape (within the wobbling and tilting range of the tip). This is because the surface deforms plastically to conform to the shape of the tip, by generating slip that creates steps on the surface with dislocations at the front of the displacement. In the figure, the scratch surfaces look slightly sharper than the shape of

the tip, with an angle difference of ~ 3°. This small difference originates from the cantilever tilt when the tip is brought into contact with the surface. The TEM image of the tip was taken perpendicular to the cantilever length; but during the scratch the cantilever tilts about 12° with respect to the InP crystal surface.

3.4.5 DEFECT MORPHOLOGY AND DISLOCATION TYPE – [110] SCRATCH

For scratches along the [110] direction, the extended defect structure corresponding to the various normal forces consists of inverted triangular regions and quasi symmetric dislocation bands, as sketched in Fig. 3.12. In reality, the actual dislocation bands are slightly asymmetric, as observed in Fig. 3.3, a feature that is believed to be due to a slight tip misalignment, as mentioned before. To help visualize the defect structure, the {111} slip planes of the face-centered cubic lattice are sketched in Fig. 3.13. Let us first consider the $(11\bar{1})$ and $(\bar{1}\bar{1}\bar{1})$ planes that appear oblique in the [110] projection in Fig. 11b. The lateral force produces in front of the tip crystal displacements that lie on the $(11\bar{1})$ planes and have positive projection cosines (shown in Table II). They push the material upwards and generate the shallow dislocation loops depicted in the figure. The lateral force also produces crystal displacements that lie on the $(\bar{1}\bar{1}\bar{1})$ planes and have negative projection cosines, which push the material downwards and generate the deep dislocations loops depicted in the figure. Let us next consider the $(\bar{1}1\bar{1})$ and $(1\bar{1}\bar{1})$ planes, seen edge-on in the <110> projection. The lateral force generates on these planes resolved shear stresses that cause clockwise and anticlockwise rotation about the normal to the surface in the vicinity of the scratch.[15] The crystal rotations result in the screw-type dislocations as confirmed by the diffraction contrast analysis.

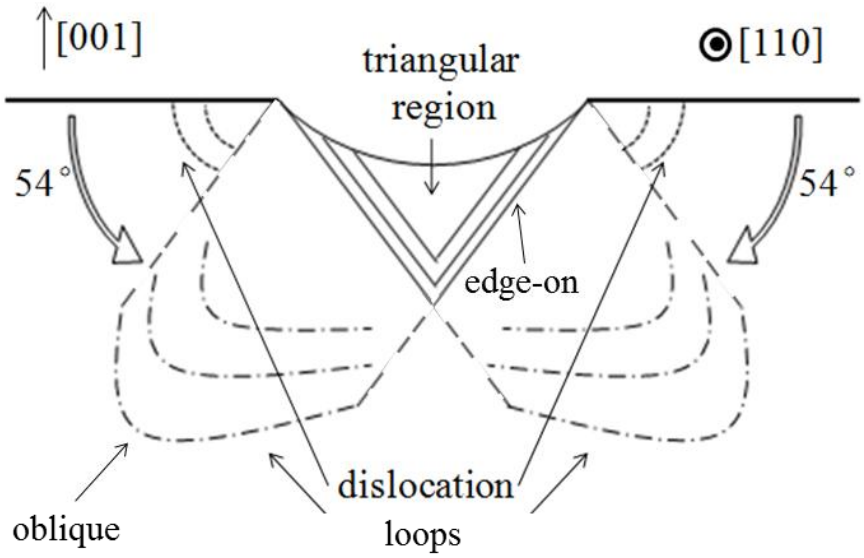

Fig. 3.12. Schematic diagram of the plastically deformed region for a <110> scratch in a projection parallel to the scratch. Solid lines represent dislocation loops on {111} slip planes viewed edge-on and dashed lines represent dislocation loops on {111} slip planes oblique to the <110> projection. Shallow dislocation loops are observed propagating close to the surface. Deep dislocation loops are observed to make an angle of 54.5 ° with the surface.

The dislocation density in the inverted triangular region is significantly higher, making it difficult to image them individually in order to determine their nature. Nevertheless, they are expected to be associated with the interaction of loops on different {111} slip planes. Increasing the normal force, this defect structure becomes magnified, keeping the same characteristics of an inverted triangular region and a quasi-symmetric dislocation loop pattern. The width of the inverted triangular region follows the curvature of the diamond tip, indicating it is the slip step that causes the deformation. Neither cracks nor fracture has been observed for any scratch in our study. At a load of 120 μN, surface discontinuities are observed at the intersections of the triangular region and the surface. This indicates that a large stored elastic energy generated by plastic deformation is released by pushing the high defect density region out of the volume, causing a pop-up

event. This is new for us. Pop out events have been reported in silicon indentation experiments, and were attributed to an amorphous-crystalline phase transition.[19, 20] In this experiments, no other phases than the zinc blende structure has been observed.

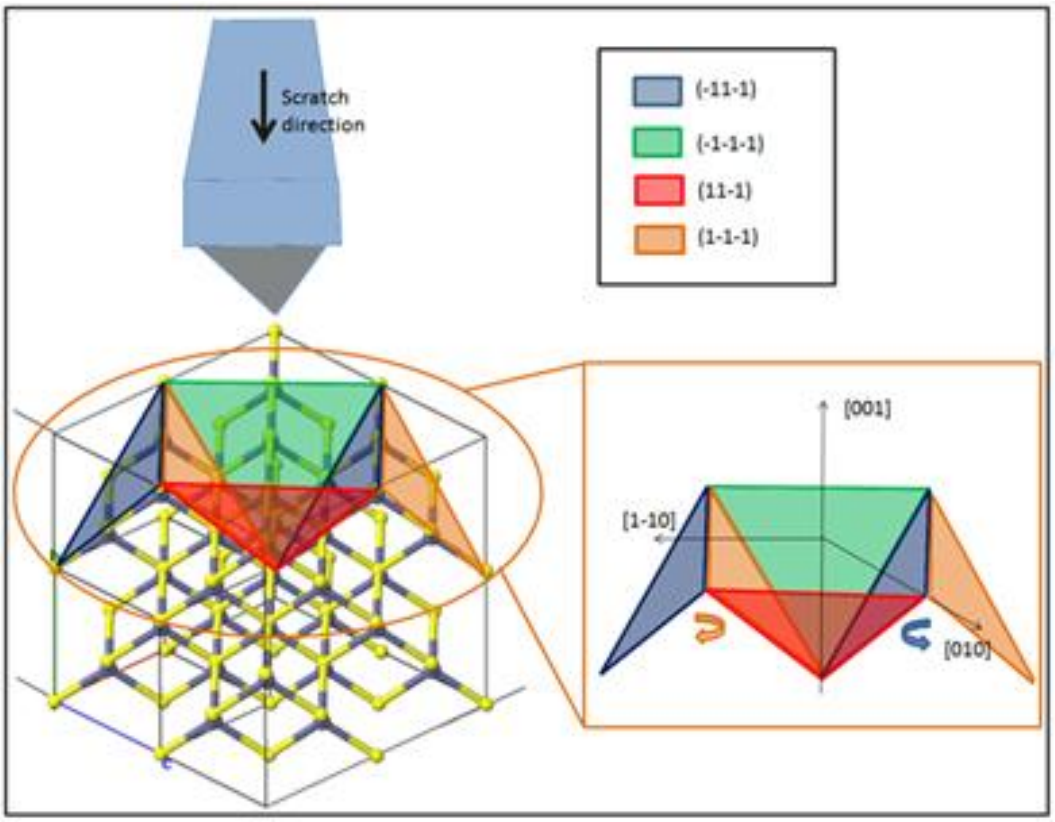

Fig. 3.13. Schematic representation of scratches along <110> showing the zinc-blende structure with the slip planes activated by the normal and lateral forces. The black arrow indicates the scratch direction. The inset shows possible rotation of slip planes activated due to lateral forces along the respective arows.

3.4.6 DEFECT MORPHOLOGY AND DISLOCATION TYPE – [100] SCRATCH

For the scratches along the <100> direction in Fig. 3.6, it has been observed that the nature of the defect structure changes with increasing normal force. This can be understood by considering the interaction between the tip and the crystal structure,

depicted in Fig. 3.14. It is noticed that the {111} planes are symmetric with respect to the normal and lateral force acting along the [001] and [100] directions; this meaning that the relative orientation of each of the forces is the same for all the slip planes. The shear stress due to the lateral force will generate a rotation in each {111} plane, leading to the generation of dislocations. Dislocations gliding on different slip planes will produce a lock at their intersection. At low load, the lock of dislocation is not obvious, single dislocation loops can be identified as observed in the 30 μN case in Fig 3.6, consisting of 30 ° and 90 ° segments. [22] When observing the sample in the <100> projection, the 30 ° segment along the <112> direction makes an angle of 27 ° with the surface, similar to the long side of the defect region observed in the scratch with 30 μN. As the applied normal force increase, the coherent rotation of these four {111} planes together with the slip of similar planes due to the normal force component leads to an inverted triangular shaped defect region, in which a number of locking and pinning occurs limiting the dislocation propagation and hardening the surface. Similar with the <110> scratch, the rotation of {111} planes happened during <100> scratch also results in mostly screw type dislocations as confirmed by ***g.b*** analysis in Fig. 3.7. The strain field loops observed under different diffraction contrast are also evidence of rotation of the {111} planes.

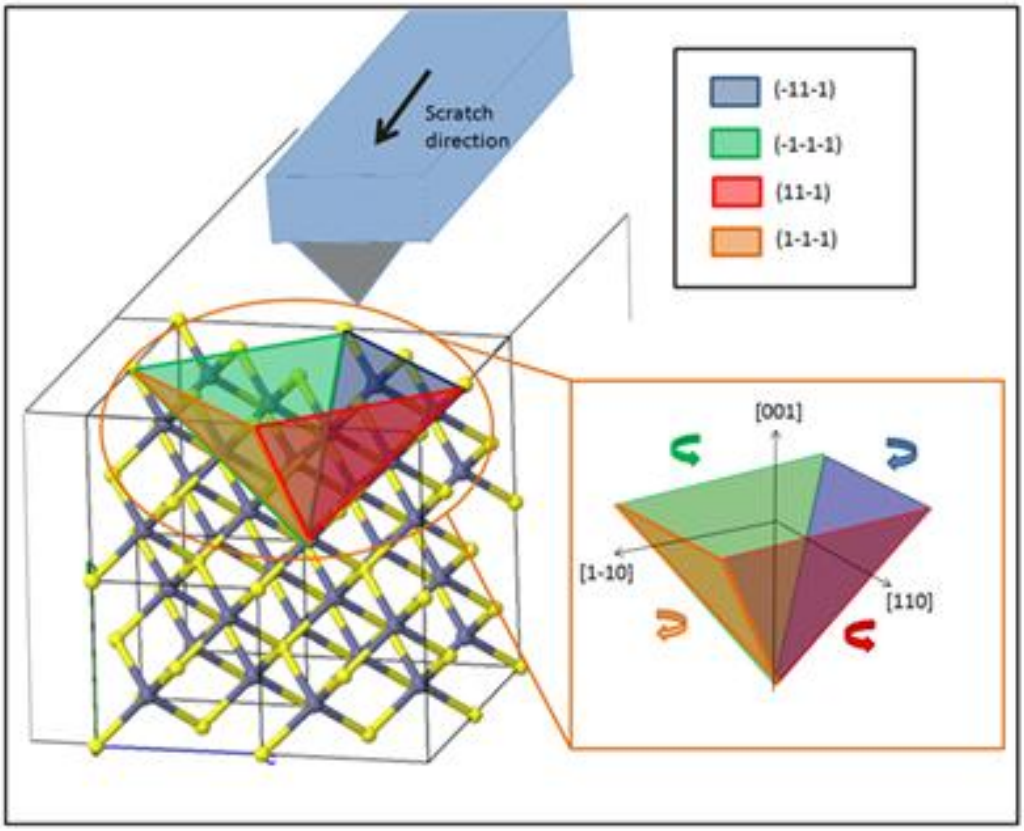

Fig. 3.14. Schematic representation of scratches along <100>, showing the zinc-blende structure with the slip planes activated by the normal and lateral forces. The black arrow indicates the scratch direction. The inset shows possible rotation of slip planes activated due to lateral forces along the respective arows.

Furthermore, the difference in depth of the defect region for the two scratch directions is shown in Fig. 3.15. At a given applied normal force, the depth of the defect region in the <100> case is always smaller than in the <110> case, which can be explained by dislocation locking that can be more possibly happened in <100> scratches. The difference is comparably larger at a load of 60 μN (~45%), than at 120 μN (~20%). Our observation suggests that a "pop-up" event relaxes the strained material under the <110> scratch and stops dislocation propagation. For the <110> scratches, the {111} slip planes that are along the scratch direction can let dislocation loops propagate to both sides of the scratch, causing a deeper defected region than that of <100> scratches. Since

the plastic deformation is deeper in <110> scratches, the material under the <110> scratch yields more than the material under the <100> scratch at a given load. So, when the load is increased to 120 μN, a "pop-up" event is firstly observed to occur for scratches along the <110> but not along the <100>.

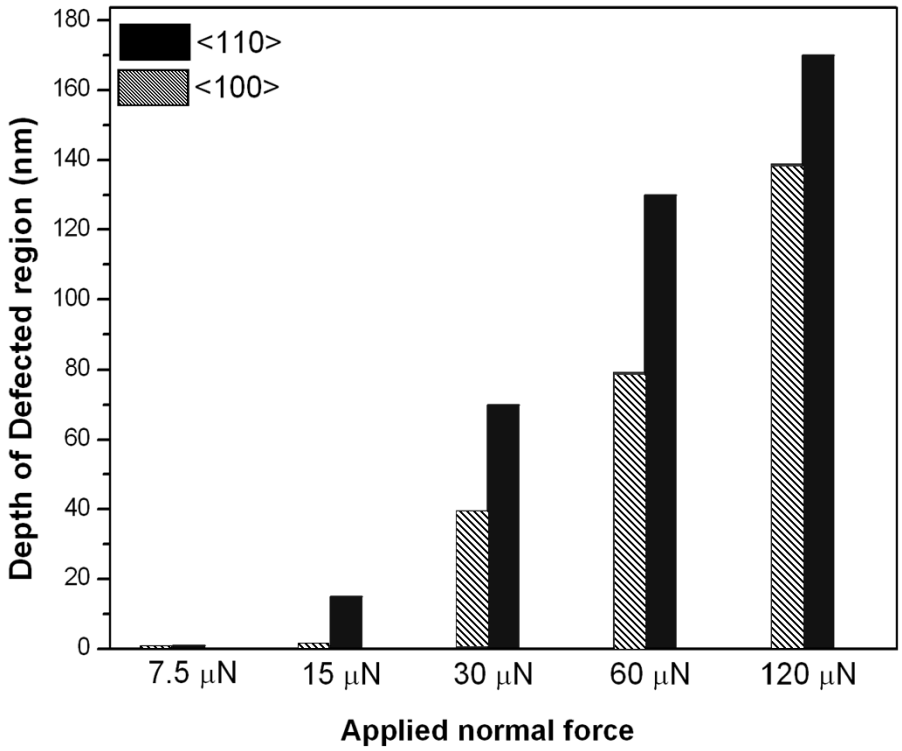

Fig. 3.15. Depth of the plastically deformed region for the various applied normal forces.

3.5 CONCLUSIONS

In summary, a thorough analysis of scratches produced with an AFM tip under various normal forces and along different crystallographic directions has been performed using AFM and diffraction-contrast TEM. Within the force range used in this study, the cross-section TEM images show that the scratch conforms to the tip shape by formation of crystal steps produced by slip of {111} planes, indicating that plastic deformation

without fracture is dominant for all scratches. Meanwhile, the slip of {111} planes produce dislocations in the material. The results presented in this paper show that both the scratch surface morphology and extended dislocation structure can be explained by the interplay between normal and lateral forces and the {111} slip system. The normal force contribution is independent on the crystallographic direction, while the lateral force contribution is highly related with the scratch direction. Considering the relative direction of the lateral force with respect to the possible <110> displacements in a <110>{111} slip system, it is found out that some of these displacements are towards the surface while others are into the crystal. For a <110> scratch, these displacements lead to the coherent local crystal movement and rotation, (along the same direction while on different slip planes), causing dislocations to propagate deep into the crystal and irregular pile-ups at the sides of the scratch. A pop-up event was observed at highest normal load for the <110> scratch. It relaxes the strained material under the scratch and slows down the dislocation propagation. For a <100> scratch, these displacements lead to the incoherent local lattice movement and rotation (along different directions and on different slip planes), causing dislocation locking that inhibit their propagation into the crystal. Meanwhile, because of the material hardening caused by dislocation locking, the displacements in the direction towards the surface lead to regular pile-up at the sides of the scratch.

REFERENCES

[1] C. K. Hyon, S. C. Choi, S. H. Song, S. W. Hwang, M. H. Son, D. Ahn, Y. J. Park, and E. K. Kim, Appl. Phys. Lett. **77**, 2607 (2000).

[2] H. Z. Song, Y. Nakata, Y. Okada, T. Miyazawa, T. Ohshima, M. Takatsu, M. Kawabe, and N. Yokoyama, Physica E **21**, 625 (2004).

[3] A. Hirai and K. M. Itoh, Physica E **23**, 248 (2004).

[4] H. D. Fonseca-Filho, R. Prioli, M. P. Pires, A. S. Lopes, P. L. Souza, and F. A. Ponce, Appl. Phys. Lett. **90**, 013117 (2007).

[5] C. Taylor, E. Marega, E. A. Stach, G. Salamo, L. Hussey, M. Munoz, and A. Malshe, Nanotechnology **19**, 015301 (2008).

[6] H. D. Fonseca-Filho, R. Prioli, M. P. Pires, A. S. Lopes, P. L. Souza, and F. A. Ponce, Appl. Phys. A.: Mater. Sci. Process. **89**, 945 (2007).

[7] B. Bhushan and V. N. Koinkar, Appl. Phys. Lett. **64**, 1653 (1994).

[8] P. Egberts and R. Bennewitz, Nanotechnology **22**, 425703 (2011).

[9] C. M. Almeida, R. Prioli, and F. A. Ponce, J. Appl. Phys. **104**, 113509 (2008).

[10] J. E. Bradby, J. S.Williams, and J. Wong-Leung, Appl. Phys. Lett. **77**, 23 (2000).

[11] J. E. Bradby, J. S.Williams, and J. Wong-Leung, Appl. Phys. Lett. **78**, 21 (2001).

[12] L. Largeau, G. Patriarche, F. Glas, and E. Le Bourhis, J. Appl. Phys. **95**, 8 (2004).

[13] C.-H. Chien, S.-R. Jian, C.-T. Wang, J.-Y. Juang, J. C. Huang and Y.-S. Lai, J. Phys. D: Appl. Phys. **40**, 3985 (2007).

[14] J. E. Bradby, S. O. Kucheyev, J. S. Williams, J. Wong-Leung, M. V. Swain, P. Munroe, G. Li, and M. R. Phillips, Appl. Phys. Lett. **80**, 3 (2002).

[15] F. A. Ponce, Q. Y. Wei, Z. H. Wu, H. D. Fonseca-Filho, C. M. Almeida, R. Prioli, and D. Cherns, J. Appl. Phys. **106**, 076106 (2009).

[16] H. D. Fonseca-Filho, C. M. Almeida, R. Prioli, M. P. Pires, P. L. Souza, Z. H. Wu, Q. Y. Wei, and F. A. Ponce, J. Appl. Phys. **107**, 054313 (2010).

[17] K. Wasmer, M. Parlinska-Wojtan, R. Gassilloud, G. Pouvreau, J. Tharian, and J. Micher, Appl. Phys. Lett. **90**, 031902 (2007).

[18] P. G. Caldas, R. Prioli, C. M. Almeida, J. Y. Huang, and F. A. Ponce, J. Appl. Phys. **109**, 013502 (2011).

[19] V. Domnich, Y. Gogotsi, and S. Dub, Appl. Phys. Lett. **76**, 2214 (2000).

[20] N. Fujisawa, S. Ruffell, J. E. Bradby, J. S. Williams, B. Haberl, and O. L. Warren, J. Appl. Phys. **105**, 106111 (2009).

[21] K. Wasmer, R. Gassiloud, J. Michler, and C. Ballif, J. Mater. Res. **27**, 320 (2012).

[22] J. Schreiber and S. Vasnyov, J. Phys.: Condens. Matter **16**, S75 (2004).

[23] C. M. Almeida, R. Prioli, Q. Y. Wei, and F. A Ponce, J. Appl. Phys. **112**, 063514 (2012).

[24] J. L. Bucaille, E. Felder, and G. Hochstetter, Wear **249**, 422 (2001).

[25] G. Patriarche and E. Le Bourhis, Philos. Mag. A **82**, 1953 (2002).

[26] Y. Ahn, T. N. Farris, and S. Chandrasekar, Mechanics of Mater., **29**, 143 (1998).

CHAPTER 4

PLASTIC DEFORMATION OF WURTZITE STUCTURAL SINGLE CRYSTALS (ZNO AND GAN) INDUCED BY NANO-INDENTATION

This chapter presents a study of nano-indentation induced plastic deformation in ZnO single crystals with various crystallographic orientations and in *c*-plane GaN crystals. This work was carried out in collaboration with Prof. Rodrigo Prioli and colleagues at Universidade Católica do Rio de Janeiro (PUC-Rio). The nano-indentations were performed by Elizandra Martins and Paula Caldas at PUC-Rio. My role in this work mainly involved micro-structural characterization using focused ion beam and transmission electron microscopy, and analysis of the deformation mechanism. Meanwhile, I cooperated with my group member Reid Juday to analyze the optical properties obtained from cathodoluminescent studies. Part of this work has been submitted to Journal of Applied Physics.

4.1 INTRODUCTION

With a direct band gap of 3.37 eV and large exciton binding energy of 60 meV, Zinc oxide (ZnO) is a highly attractive II-VI compound semiconductor for its potential application in short-wave optoelectronic devices such as blue and UV light emitting diodes, laser diodes and optical detectors.[1-3] Due to the availability of high-quality ZnO crystals with low dislocation densities and the small lattice mismatch (~1.7%) between ZnO and GaN[4,5], which has been widely used in the solid state lighting, ZnO has been treated as a potential substrate or buffer for the growth of GaN epitaxy.[6, 7] However, both ZnO and GaN, with the c-axis as natural growth, exhibit strong spontaneous and piezoelectric polarization,[8] which could have a negative influence on

the performance of light emitting devices by means of the quantum-confined Stark effects (QCSEs).[9, 10] Therefore, non-polar growth has been proposed to avoid it. Lately, there has been a lot of research interest aroused on the growth of m-plane ZnO epitaxy,[11-13] and m-plane III-nitride alloys epitaxy on m-plane ZnO substrate or buffer.[14, 15] However, as a relatively soft material (with a hardness of only ~5 Gpa for c-plane),[16] ZnO could be significantly deformed during the thin film growth and device processing. So, even though high–quality ZnO single crystals growth can limit the density of built-in dislocations, contact loading which is frequently encountered during material fabrication can induce deformation in a small volume, in which many defects could be introduced to significantly degrade the performance, or lead to device failure performance. Therefore, it is important to understand the mechanical behavior and the resulting structural and optical properties of deformed material before apply it to optoelectronic devices. Previous studies on the mechanical properties of ZnO have been conducted either on polycrystalline materials,[17] which provided limited information about the deformation mechanism, or on *c*-plane ZnO,[18, 19] which reported that the basal and pyramidal slip systems are the major deformation mechanism. Few people have reported such properties on non-polar ZnO. As research interests on non-polar growth of GaN and ZnO films and optoelectronic device demonstrations have been grown rapidly as the possible fabrication of high performance LEDs free from the polarization appears in sight, study on corresponding mechanical properties of non-polar wurtzite structures becomes essential. In this chapter, a complete and systematic investigation on the mechanical characteristics of deformed polar and nonpolar ZnO single crystals, such as the micro-structural and optical properties, will be presented. The results presented and discussed

here will allow us to unveil the mechanical deformation mechanisms of wurtzite ZnO at the nanometer scale, which should have technological implications for the fabrication of ZnO-based devices.

4.2 EXPERIMENTAL DETAILS

The ZnO crystals used in this study are 0.5 mm thick, oriented along the $\langle 1\bar{1}00 \rangle$ *m*-, $\langle 11\bar{2}0 \rangle$ *a*-, and $\langle 0002 \rangle$ *c*-directions respectively, and grown by the hydrothermal technique by the MTI Corporation. Nano-indentations were performed on the crystals with applied loads ranging from 3.0 mN to 5.0 mN, at room temperature, using a commercial nanoindetation system. The nanoindentations were performed by first linearly increasing the applied load from zero to a desired maximum value in 5 sec, then keeping it at the maximum value for 2 sec, and then linearly decreasing down to zero in 5 sec. The nano-indenter used in all indentations is a cono-spherical diamond tip with a radius of curvature ~260 nm. At this load, reasonable residual plastic deformation was produced and significant CL contrast was obtained. The CL study was performed at liquid He temperature (4.4K) using an Oxford Instruments Mono CL system, installed on a JEOL 6300 scanning electron microscope (SEM). The TEM samples were prepared by a focused ion beam (FIB) in a Nova 200 UHR FEG (FEI) system, which also provides the SEM image of indentations. Before milling, the indented surface was protected from ion damage by the deposition of a ~1 μm thick platinum layer on top. TEM foils were cut along the $\langle 0002 \rangle$ *c*-projection and $\langle 11\bar{2}0 \rangle$ *a*-projection respectively on the indentation on the *m*-plane ZnO, $\langle 0002 \rangle$ *c*-projection and $\langle 1\bar{1}00 \rangle$ *m*-projection respectively on the indentation on the *a*-plane ZnO, and for the indentation on the c-plane ZnO, two TEM

foils were cut along $\langle 11\bar{2}0\rangle$ *a*-projection and $\langle 1\bar{1}00\rangle$ *m*-projection. TEM imaging was taken in a FEI CM 200 system and JEOL 4000EX system.

4.3 RESULTS AND ANALYSIS

4.3.1 LOAD-DISPLACEMENT CURVES

Figure 4.1 is the load-displacement curve obtained from the indentation on *m*-plane and *c*-plane ZnO with maximum loads of 5 mN, The tip used for these indentations is a cono-spherical indenter with radius of 260 nm. For the *m*-plane case, the total penetration depth during the indentation is of ~580 nm. A residual plastic deformation with a depth of ~ 370 nm was left in the crystal after elastic recovery. From the magnified inserted curve, a "pop-in" event is firstly observed at a load of ~200 μN, which indicates the catastrophic plastic deformation as a result of structural changes induced by nano-indentation. And the pop-in length was observed to be about 23 nm. From the unloading curve and the analytical method developed by Oliver and Pharr,[20] the hardness of *m*-plane ZnO single crystal was calculated to be ~ 4.1 Gpa in this study. However, it is important to point out here that the measured "hardness" depends on the size of the tip.[21] Typically, higher values are obtained with smaller tip sizes. The small radius of curvature of the tip used in our measurements increases the local applied shear stress and can activate several slip planes simultaneously.

In the case of indentation on the *c*-plane ZnO, the total penetration depth during the indentation is of ~315 nm and the residual plastic deformation depth is about 240 nm, both of which are smaller than the similar parameters obtained by indentation on m-plane ZnO. The first "pop-in" event is observed when the load reaches about 250 μN, with a pop-in length of 8 nm. Since this indentation was made with the same condition as that

applied on the *m*-plane ZnO, the hardness of *c*-plane ZnO (~ 6.5 Gpa) determined to be from the unloading curve indicates *c*-plane ZnO crystal is more resistive to deformation than *m*-plane one.

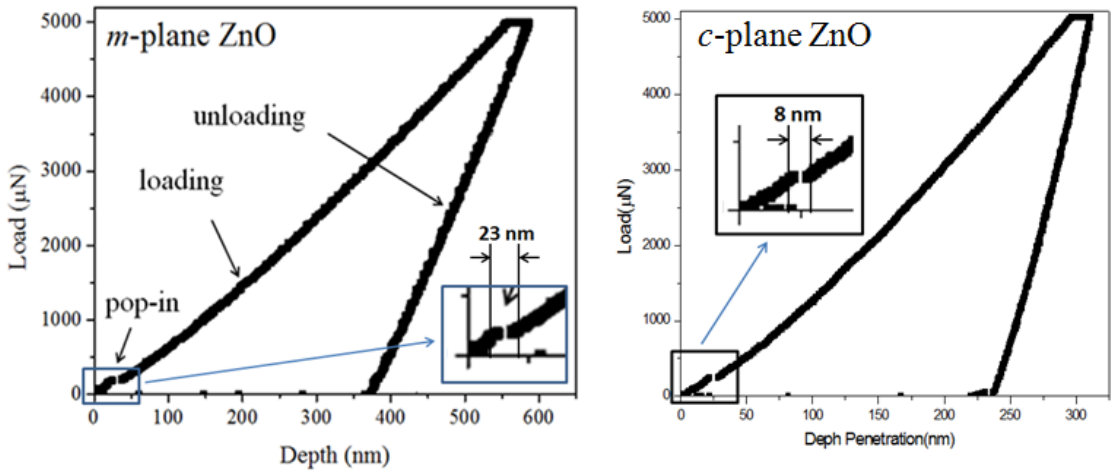

Fig. 4.1. Load-displacement curve of indentation on *m*-plane and *c*-plane ZnO single crystals with maximum load of 5.0 mN.

The pop-in event has been proved to be the critical crossover for the elastic-plastic transition, which is related to the formation of defects. So the difference on the two characteristics at each pop-in events of the *c*-plane and *m*-plane ZnO, critical force (250 μN for *c*-plane ZnO and 200 μN for *m*-plane ZnO) and pop-in length, or called slip length, (8nm for *c*-plane ZnO and 23 nm for *m*-plane ZnO), indicates different defects formation mechanism, or say deformation mechanism, was involved in these two samples.

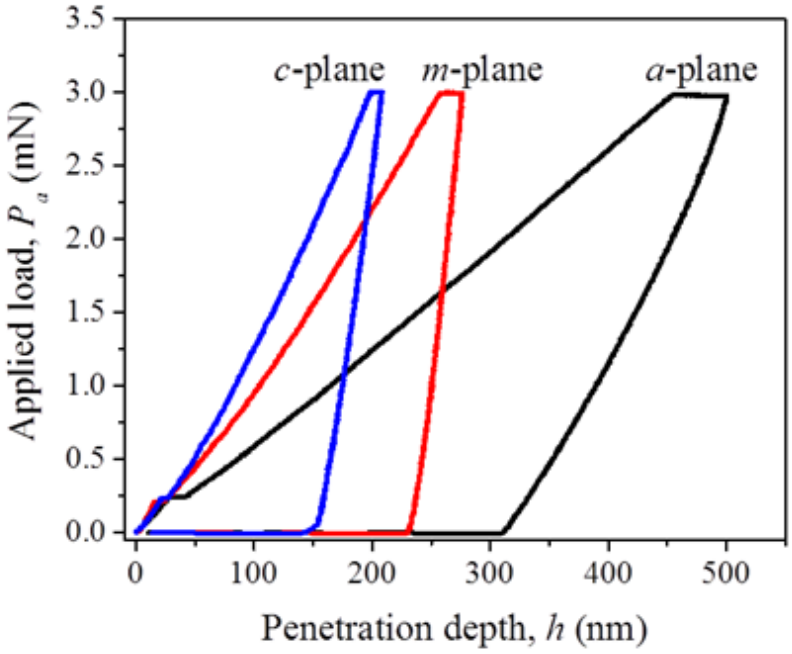

Fig. 4.2. Load-displacement curve of indentation on *a*-plane, *m*-plane and *c*-plane ZnO single crystals with maximum load of 3.0 mN.

To make a complete comparison, loading-displacement curves for indentations on *a*-, *m*-, and *c*-planes ZnO crystals are shown in Fig. 4.2. These were acquired using a maximum applied load of 3.0 mN with the same tip described above. The *c*-plane crystal turns out to be more resistive to deformation than the *a*- and *m*-plane crystals, as is shown by the lower penetration depth at equal values of the applied load. The maximum stress (or say "hardness" in this condition) obtained by dividing the maximum applied load by the projected contact area of the tip at that load, $\sigma_{max} = P_{max}/A_{p,max}$ is shown in Table 4.1. On the one hand, the values for *c*- and *m*- plane ones are consist with those obtained from indentations with maximum load of 5 mN, confirming that the "hardness" value tends towards a constant value for high applied loads.[18, 21, 22] On the other hand, the *a*- and *m*-plane crystals exhibit σ_{max}values smaller than that of the *c*-plane crystal, with

the *a*-plane crystal supporting the least amount of stress. The σ_{max} value for the *a*-plane crystal, 2.3 GPa, agrees well with reported values for the "hardness" of single crystal *a*-plane ZnO, namely 2.0 GPa, obtained from load-displacement curves using a tip radius of 4.3 μm.[19] The σ_{max} value for the *m*-plane crystal, 4.1 GPa, found using our tip and indentation method is also comparable to "hardness" values of single crystal *m*-plane ZnO, reported to be between 2 and 4 GPa, obtained from load-displacement curves using a diamond Berkovich indenter tip.[23] The value for the *c*-plane ZnO, 6.5 GPa, lies between the reported "hardness" values of 4.8 and 7.2 GPa, obtained from load-displacement curves for tip radii of 4.3 and 0.08 μm, respectively.[19, 22] Therefore, considering tip size, our σ_{max} value is reliable with reported ones. The trend is clear, with the *a*-plane being the "softest" face and the *c*-plane being the "hardest" face.

TABLE 4.1. The maximum stress σ_{max} determined from load-displacement curves, corresponding to a conospherical tip with R = 260 nm.

Surface Orientation	σ_{max} (GPa)
a-plane	2.3 ± 0.1
m-plane	4.1 ± 0.1
c-plane	6.5 ± 0.3

4.3.2 EFFECT OF PLASTIC DEFORMATION ON THE LUMINESCENCE

Figure 4.3 shows the low temperature (LT) photoluminescence (PL) and cathodoluminescence (CL) spectra of the *c*-plane ZnO crystal. The peaks are labeled in accordance with Meyer's results.[24] The spectra are dominated by donor-bound exciton transitions at residual donors, located between 3.350 and 3.375 eV. A free exciton transition, associated with valence subband A, is observed at 3.377 eV. According to the

specifications from the ZnO grower, aluminum is thought to be the most common impurity in these crystals, and the LT luminescence is dominated by aluminum donor-bound excitons, labeled as I_6 at 3.360 eV. At energies below 3.350 eV we observe longitudinal optical (LO) phonon replicas and a two-electron satellite (TES) of the main peak, I_6. The LO phonon replica peaks are separated from their associated peak by integer multiples of the LO phonon energy in ZnO, 72 meV. The TES of I_6 is will be located lower in energy of I_6 by ¾ of the donor energy. The donor energy level of Al is 52 meV,[24] therefore the TES of I_6 should be located at 3.360 eV – ¾ (0.052 eV) = 3.321 eV, which agrees well with our labeling. The luminescence from each of the differently-oriented crystals looks similar, taken by both PL and CL, and therefore it can be concluded that the crystallographic orientation of these ZnO single crystals does not have an obvious effect on the luminescent properties.

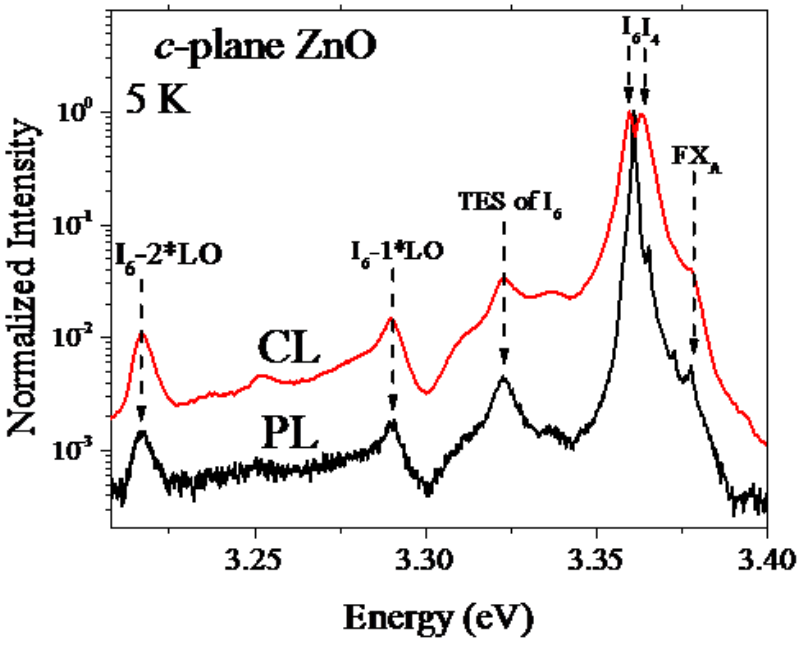

Fig. 4.3. Normalized low temperature CL and PL spectra of the *c*-plane ZnO crystal.

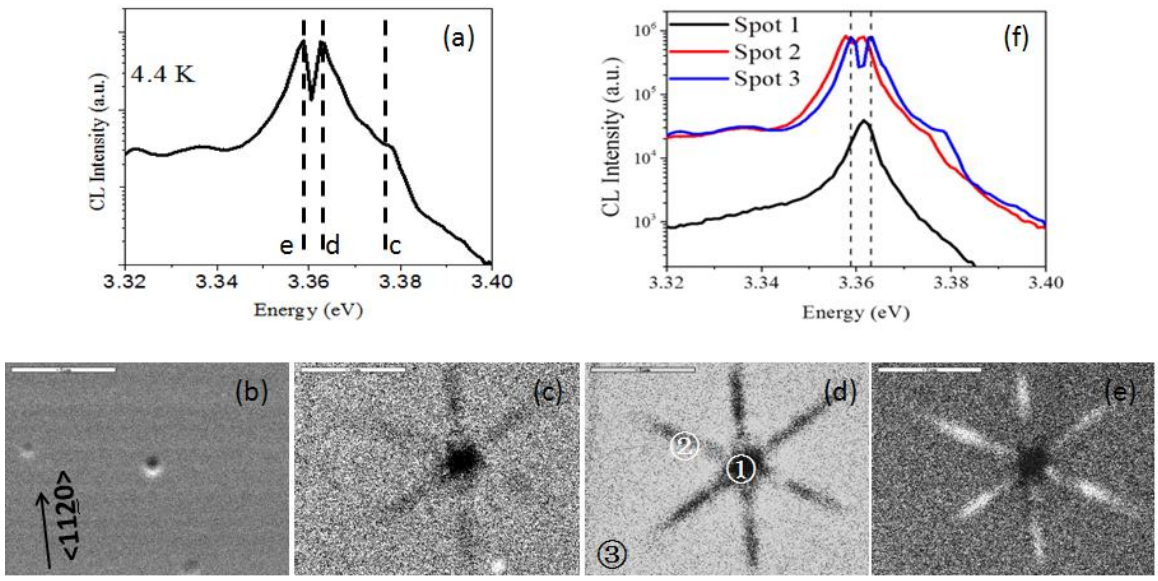

Fig. 4.4. (a) Low temperature CL spectra, (b) SEM image, (c)-(e) CL monochromatic mappings, and (f) spot-mode CL spectra of the indentation on the *c*-plane ZnO crystal.

To investigate the effect of nano-indentation on the luminescence of ZnO single crystals, a series of complete CL spectra and SEM images were taken from the nano-indented areas. Figure 4.4 shows the results from an indentation in the c-plane ZnO. (a) is the LT CL spectrum, (b) is the SEM image, (c)-(e) are the monochromatic mappings taken at the energies indicated in (a), and (f) is the spot-mode CL spectra taken at different spots near the indentation as marked in (e). It is apparent in the mappings that the indentation creates six radial lines lying equally spaced around the indentation, and these defect lines lay along the six equivalent $\langle 11\bar{2}0 \rangle$ *a*-directions. Similarly-shaped near band-edge luminescence quenching has previously been observed in *c*-plane indented ZnO.[18] These lines appear with dark contrast in Fig. 4.4(c)-(d) and bright contrast in (e). The lines extend for approximately 5 μm in each *a*- direction. From the Fig. 4.4(f), the luminescence is greatly decreased when the beam is kept on the indentation tip-

material contact spot. While spectrum taken at spot2 which is located on one of the six radial lines observed in mappings exhibit luminescence which has been red-shifted by 1-2 meV from spot3 where perfect crystal. The CL intensity between Spot 2 and Spot 3 is essentially unchanged, indicating the 1-2 meV red shift in emission wavelength, which is sufficient to give us the contrast change in mappings, comes from the indentation-induced tensile strain distribution.

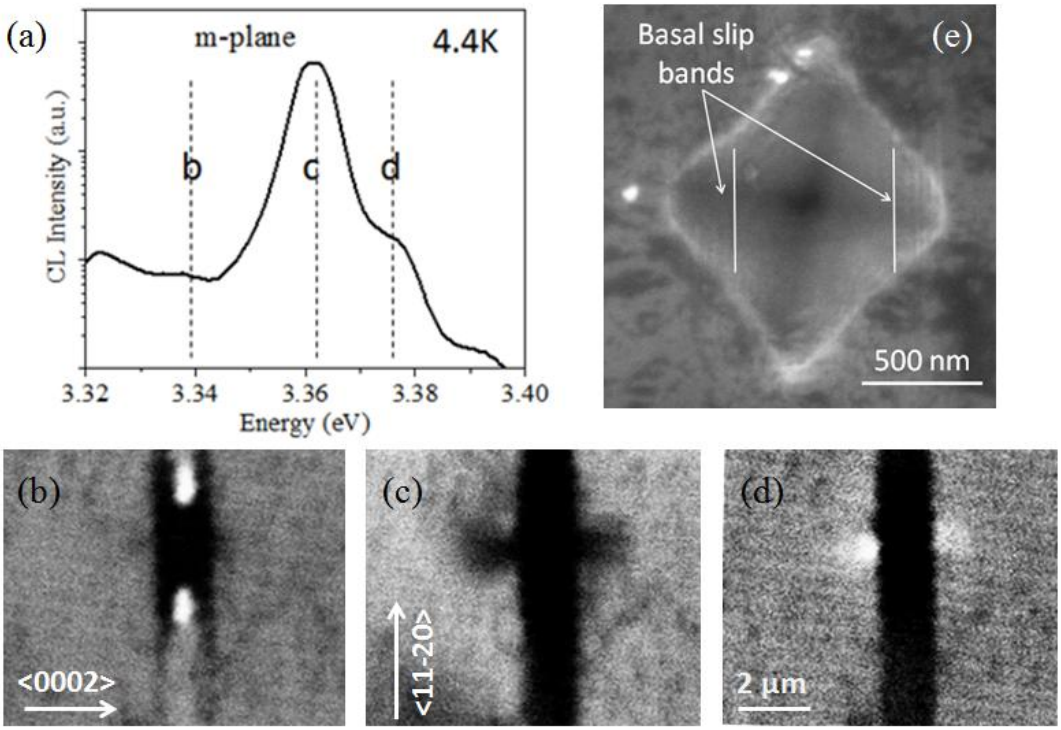

Fig. 4.5. (a) Low temperature CL spectra, (b)-(d) CL monochromatic mappings, and (b) SEM image, of the indentation on the *m*-plane ZnO crystal.

Figure 4.5 shows the results from an indentation on m-plane ZnO. As marked in Fig. 4.5(e), which is the SEM image of the indent, many parallel lines are observed along $\langle 11\bar{2}0 \rangle$ c- directions, which indicate the basal plane slip bands. From the CL spectrum acquired from this region in (a) and the monochromatic CL mappings shown in (b)-(d) which were taken at different energies: (b) 3.340 eV, (c) 3.362 eV and (d) 3.376 eV

respectively as marked by dashed lines in (a), the main emission peak that occurs at 3.362 eV comes from the perfect ZnO crystal bulk, which is the donor-bound exciton emission for ZnO materials.[24, 25] Near the indentation region, this emission vanishes and appears as a dark region which consists of a dark band along the $\langle 11\bar{2}0\rangle$ *a*- direction and two ear-like dark regions besides the dark band extending along the $\langle 0002\rangle$ c- direction. It is assumed that this donor-bound emission quenching is caused by nano-indentation induced non-radiative defects in the basal planes and the strain build up along the ±*c* directions. Fig.4.5(b) and (d), which are the monochromatic CL mappings taken at lower and higher energies of the main emission peak respectively, show the presence of similar dark bands along the a- direction. However, the mapping taken at lower energy shows spotty luminescence close to the indentation pit along a- direction, and the mapping taken at higher energy shows contrast inversion on the two ear-like regions, compared to (c). This contrast change indicates that these regions are either strained or containing some defects that act as radiative recombination centers. Similar phenomenon was also observed in indentations made on *a*-plane ZnO, as shown in Fig. 4.6, dark bands along basal planes and ear-like bright spots besides the dark bands.

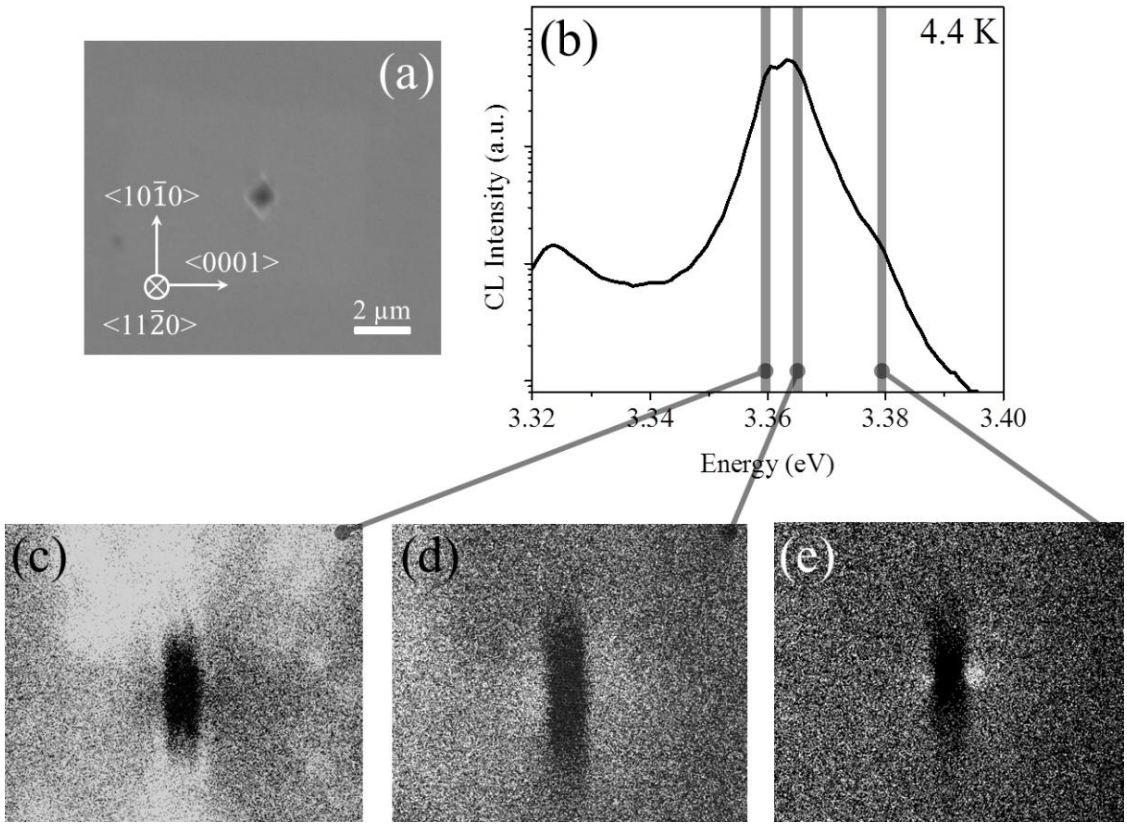

Fig. 4.6 (a) SEM image, (b) Low temperature CL spectra, and (c)-(e) CL monochromatic mappings, of the indentation on the *a*-plane ZnO crystal.

4.3.3 MICROSTRUCTURAL CHARACTERIZATION ON THE PLASTIC DEFORMATION

Although the CL results described above gave us an indication on how the indentation on different facets could introduce various kinds of deformation to ZnO single crystals from the top view, TEM analysis described in this part could bring more detailed information on what kind of deformation mechanism happened during indentation and how the defects propagate inside these differently oriented crystals. Figure 4.7 shows some TEM images taken from two samples that were both prepared along the $\langle 11\bar{2}0 \rangle$ *a*-projection containing the deformed region in *c*-plane ZnO. Diffraction conditions used for them are marked in the images. Since defects that extend

to sides are mostly invisible when $\boldsymbol{g=c}$ as shown in (a) and (d) and become invisible when $\boldsymbol{g=m}$ as shown in (b) and (c), it can be concluded that indentation induced displacements that have $\boldsymbol{c}$ component are mostly happened right below the tip-material contact area, where is the highly defected region. In this highly defected region, besides the horizontal defect lines, there are some inclined defect lines which mostly make an angle of 61° with the surface. This indicates that in the highly defected region right below the indenter, two kinds of deformation mechanism happened. One is the basal plane (0002) slip and the other is pyramidal plane $(1\bar{1}01)$ slip. Meanwhile on the sides of indentation, only horizontal defect lines have been observed, with equivalent extending range as the spikes observed in CL. It indicates that only basal plane slip occurs on sideways. So, combining the TEM observation with the CL results observed in Fig. 4.4, we can conclude that the basal plane slip has preferential directions – the six equivalents $\langle 11\bar{2}0\rangle$ *a*- directions. So the short horizontal defect lines that can be clearly seen in Fig. 4.7 (c) are the segments of dislocation loops that travel along $\langle 11\bar{2}0\rangle$ directions. Then the defects generated by pyramidal plane slipping act as nonradiative recombination centers, while the dislocation loops propagating along $\langle 11\bar{2}0\rangle$ directions build tensile strain along these directions.

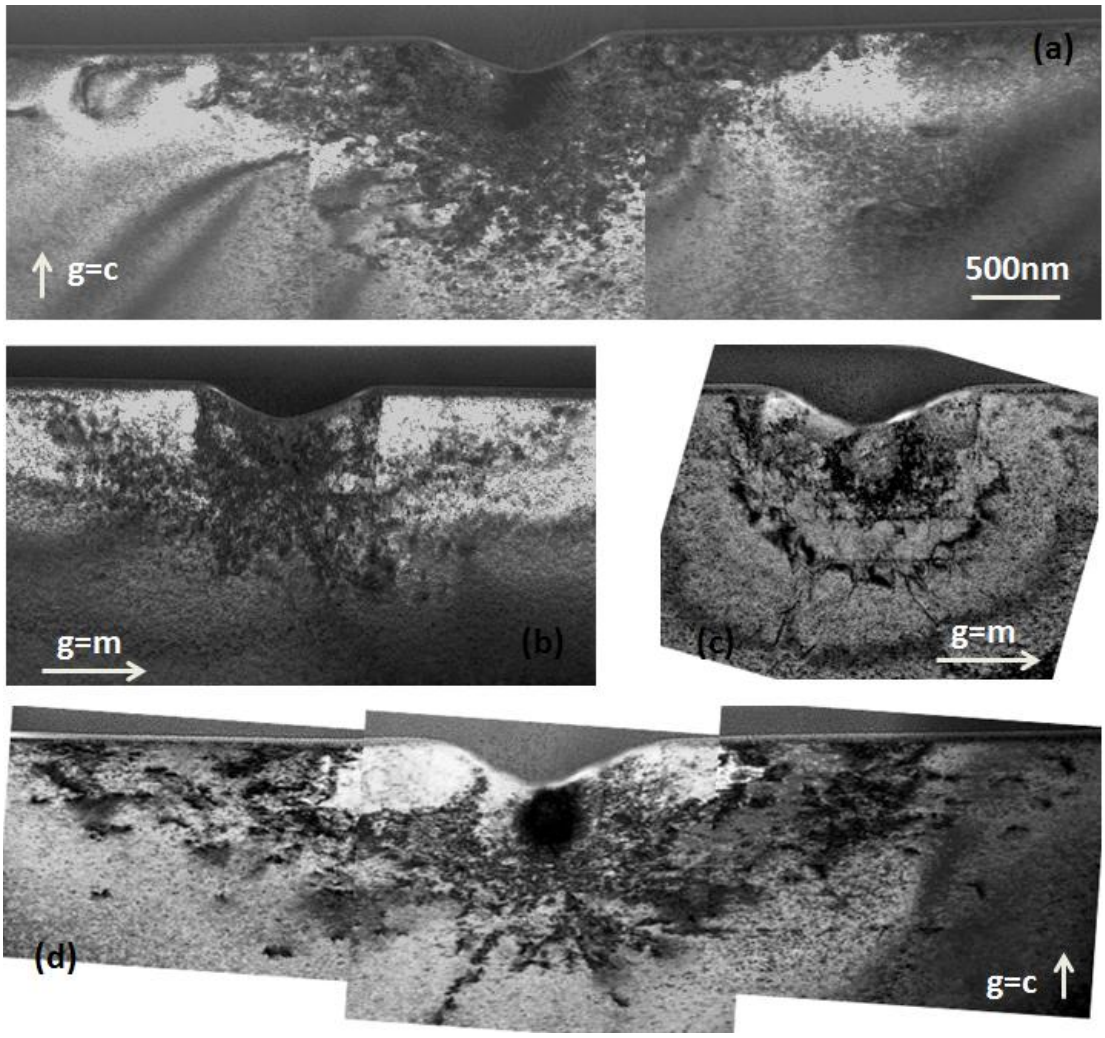

Fig. 4.7. Bright field TEM images showing the defects introduced by indentation on c-plane ZnO single crystals. (a) and (b) are acquired from one sample with different diffraction conditions; (c) and (d) are acquired from the other sample with different diffraction conditions.

Figure 4.8 shows bright field (BF) TEM images and diffraction patterns (DP) taken from samples that contain indentations and the deformed region in *m*-plane ZnO. This sample was prepared along the $\langle 11\bar{2}0 \rangle$ *a*-projection. These images were taken with different diffraction conditions as marked by arrows. Images shown in Fig. 4.8(a) and (b) were taken with same magnification and show the defects near the indent. They display

that the defects are highly localized near the tip-surface contact region and propagate into the crystal. Unlike the case reported in *c*-plane ZnO case, [16] indentation-induced dislocations in *m*-plane ZnO hardly extend beyond the boundary of the tip-surface contact region along *c*-direction. Dislocations that are visible with $\boldsymbol{g} = (1\bar{1}00)$ in (a) are out of contrast with $\boldsymbol{g} = (0002)$ in Figure (b), so the Burgers vector of these dislocations can be determined that it lies in the direction which is perpendicular to $\langle 0002 \rangle$. In other words, the plastic deformation induced by the indentation on *m*-plane ZnO single crystal occurs due to atomic-scale slip along the basal plane right below the contact region and the depth of the dislocation propagation follows the profile of the tip shape. The same as the *c*-plane case, those defects in the highly deformed region act as non-radiative recombination centers for excitons as seen in the CL results. This explains why the dark band in the CL mapping prominent along the $\langle 11\bar{2}0 \rangle$ direction and is restricted to a width, approximately the same dimension of the indent itself along the $\langle 0002 \rangle$ direction. Although clear dislocation lines that are visible in Fig. 4.8(a) are out of contrast in Fig. 4.8(b), there is still some spotty contrast in the deformed region in Fig. 4.8(b), which may indicate some small lattice displacement along the *c*- direction induced by a lateral component of the force as the side of the indenter tip comes in contact with the crystal. This assumption can be confirmed by the stretching along the $\langle 0002 \rangle$ direction of the selected area diffraction (SAD) spot as shown in Fig. 4.8(c). Meanwhile, from the diffraction pattern there is no evidence of phase transformation. Because of the accumulated small displacements in the *c*- direction and lack of relaxation available normal to the preferred basal slip planes, the crystal tend to build up compressive strain on the two sides of indentation along *c*-direction. And this conclusion consists with the

CL mapping in Fig. 4.5(d). Strain in a semiconductor crystal can change its lattice parameter from natural value then affect the materials band gap.[26] A compressive strain decreases the lattice parameter, which will correspond to an increase in the band gap energy. Tensile strain has the opposite effect. Fig.4.5(d) was taken at higher energy shoulder of the main peak, so luminescence from the two ear-like dark regions besides the main dark band indicates an increase of the band gap energy from materials in that region, which correspond to the compressive stain in that region. And it is this compressive strain that leads to a blue-shift of the bound exciton transitions. Also spot-mode CL was performed on this ear-like region, showing a shift of each free and bound exciton peak to a higher energy by approximately 5meV. The pressure-induced shift in ZnO single crystal has been reported to be approximately 24 meV/GPa for free excitons.[27] Therefore, a compressive stress of ~ 0.2 GPa in these regions can be estimated.

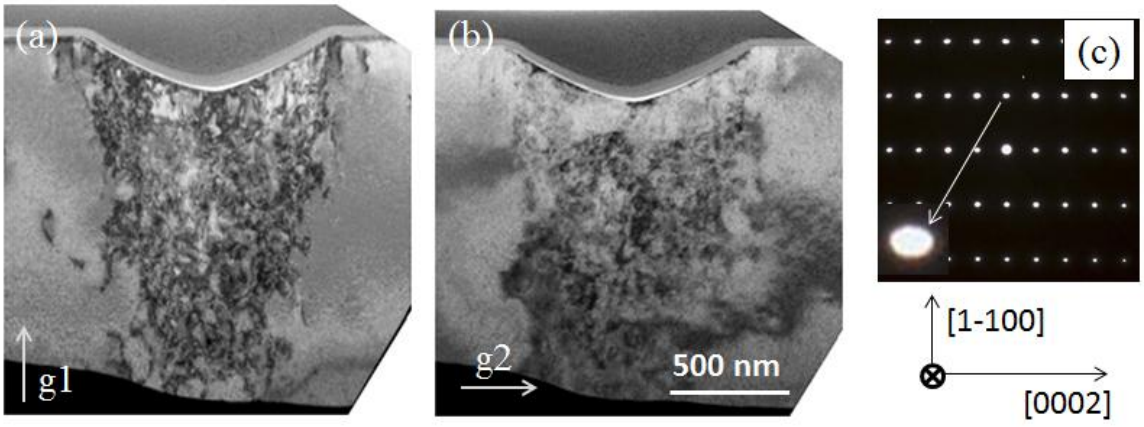

Fig. 4.8. (a) and (b) are Bight field TEM images showing the defects introduced by indentation on m-plane ZnO single crystals. They are acquired from one sample with different diffraction conditions along $\langle 11\bar{2}0 \rangle$ projection; (c) is the diffraction pattern (DP) acquired from the defected region.

So, from the SEM, TEM and CL results, basal plane slipping has been confirmed to be the main deformation mechanism when an indentation is exerted on *m*-plane ZnO single crystal. By comparing it with the precious *c*-plane ZnO results, and those reports on c-plane ZnO single crystal,[18,19] in which the main slip system is basal plane slipping in addition to pyramidal slipping, the difference in the hardness value of the c- and m- facet of ZnO can be explained by the orientation of the basal planes with respect to the indentation axis. Similar conclusion has been reported on the difference in the hardness value of the c- and a- plane ZnO.[28]

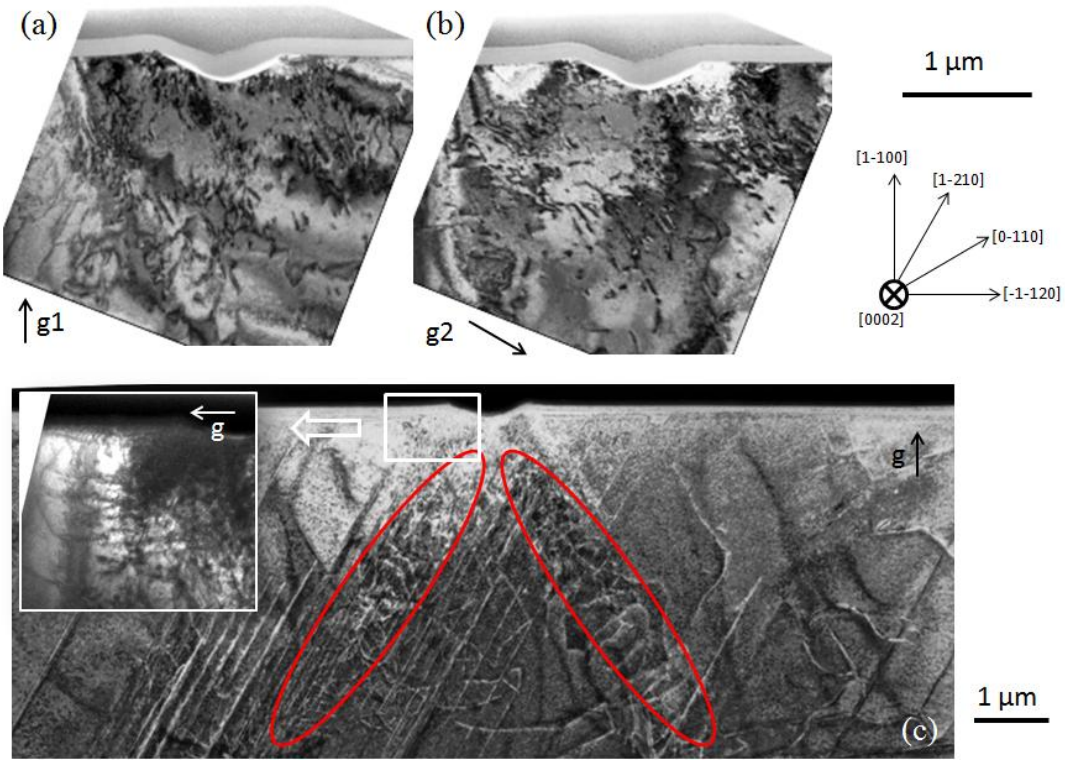

Fig. 4.9. Bight and dark field TEM images showing the defects introduced by indentation on m-plane ZnO single crystals. These samples were prepared along <0002> projection.

On the other hand, to find the reason that the dark band in the CL mapping can extend beyond the boundary of the tip-surface contact region along the $\langle 11\bar{2}0\rangle$ direction, not like the width restriction along the $\langle 0002\rangle$ direction, another TEM sample was prepared along the $\langle 0002\rangle$ *c*- projection, as shown in Fig. 4.9. Fig.4.9(a) and (b) show the region near the indentation. From these two images, it is observed that dislocations generated by the nano-indentation extend beyond the contact area. Detailed crystalline directions are indicated next to the images and the diffraction condition used for each image is marked as arrows $\boldsymbol{g_1}$ and $\boldsymbol{g_2}$. These two images display that most dislocations propagate along $\langle 11\bar{2}0\rangle$ directions, extending beyond the boundary of the contact areas. Therefore, it is concluded that dislocations generated by nano-indentation on *m*-plane ZnO are the non-radiative recombination centers, which cause the quenching of the near bandage emission as observed as the dark band in Fig. 4.5. By comparing the visibility of dislocations with different diffraction conditions in Fig. 4.9(a) and (b), it is found that most dislocations are out of contrast when the $\boldsymbol{g}$ condition is normal to the dislocation lines. For example, dislocation lines which are along $[\bar{1}2\bar{1}0]$ direction becomes invisible with $\boldsymbol{g_2}= (10\bar{1}0)$ which is normal to the dislocation line. And from the *a*- projection TEM results shown in Fig. 4.8, we have learned that slipping mainly occurs along the basal planes, thus, based on "$\boldsymbol{g.b}$" criterion,[29] the Burgers vectors of these dislocations which are along $[\bar{1}2\bar{1}0]$ direction is parallel to the dislocation lines. So these dislocations are mostly of perfect screw type perfect dislocations, created by $\frac{1}{3}\langle 11\bar{2}0\rangle(0002)$ slip system. These slips as well as dislocation propagation and extension can be seen more clearly in the dark field image in Fig. 4.9(c), which was taken in a lower magnification to show the whole defected region. It shows that the most dislocation lines are along the two $\boldsymbol{a}$-

directions ($[\bar{1}2\bar{1}0]$ and $[\bar{2}110]$) that are inclined with surface. And there are two dislocation bands as circled in this image, consisting of a high density of dislocation loops and extending along the two ***a-*** directions. These dislocation loops have screw components on sides and edge components on front, while the screw components predominant in the appearance. The magnified image inserted in the Fig. 4.9(c) also shows that at the region near the surface, there is some dislocations propagating along the $\langle 11\bar{2}0\rangle$ *a*-direction that is parallel to the surface and bending to end at the crystal surface.

Parallel analysis was also exerted on the indentation produced on the $\langle 11\bar{2}0\rangle$ *a*-plane ZnO single crystal. Figure 4.10 shows bright field TEM images taken from samples that contain indentations and the deformed region in *a*-plane ZnO, in which the diffraction conditions are marked by arrows. The sample shown in Fig. 4.10(a) and (b) was prepared along the $\langle 0002\rangle$ *c*-projection, and the other one shown in Fig. 4.10(c) and (d) was prepared along the $\langle 1\bar{1}00\rangle$ *m*-projection. Very similar to the observation from the indentations on *m*-plane crystal, dislocation propagation in basal planes are proven in (c) and (d), in which dislocations are visible with ***g=c*** and become invisible with ***g=m***. Also these dislocations mostly propagate along $\langle 11\bar{2}0\rangle$ *a*-directions as observed and circled in (a) and (b), with restriction along *c*- direction and extension along *m*-direction. Therefore, it is concluded that the deformation mechanism for indentation on non-polar ZnO surface is all originated from the 1/3 $\langle 11\bar{2}0\rangle(0002)$ slip system. The only difference is that, given the same applied normal force, dislocations in *a*-plane ZnO propagate deeper than that in the *m*-plane ZnO. We believe this can be explained by considering the angle of the dislocation propagation direction $\langle 11\bar{2}0\rangle$ with respect to the crystal surface.

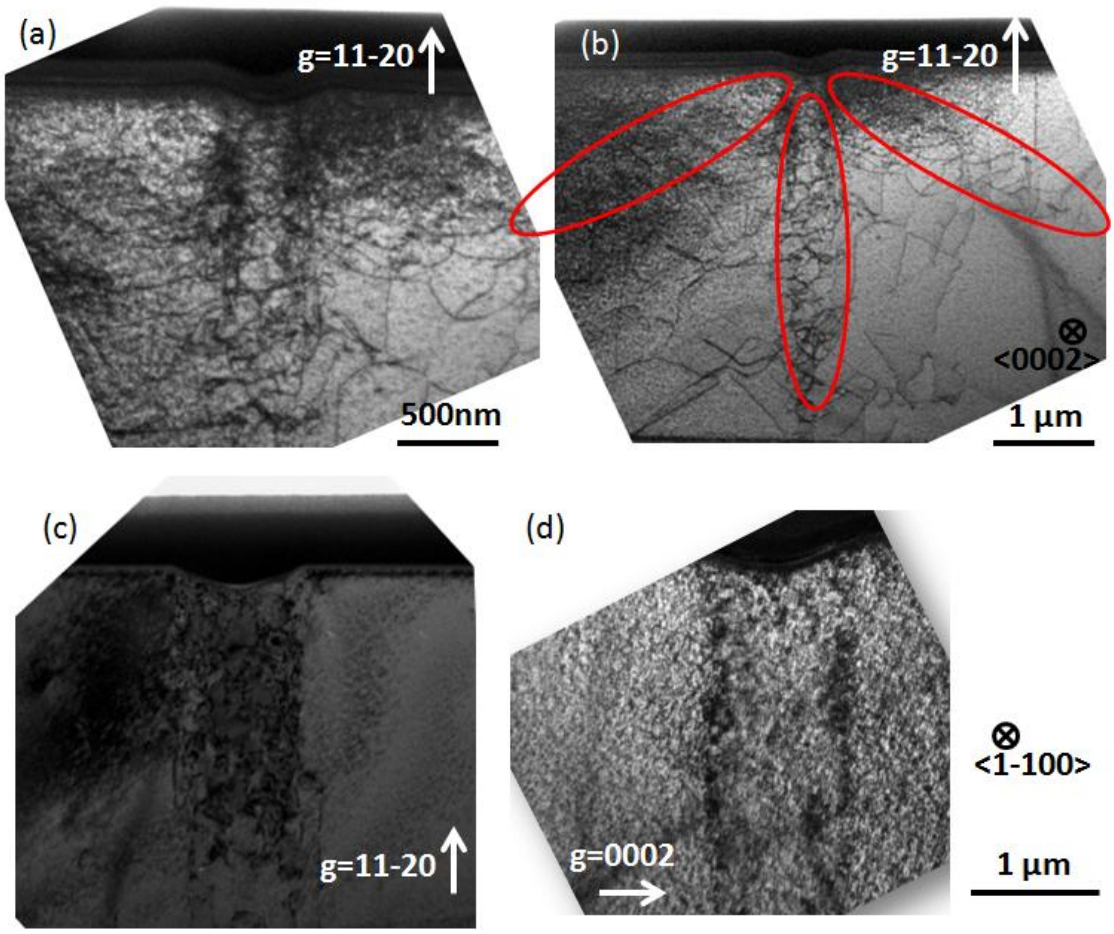

Fig. 4.10. Bight field TEM images showing the defects introduced by indentation on a-plane ZnO single crystals. These images were taken at different magnifications and with different diffraction conditions. The diffraction condition used for imaging is marked as arrows. The scale bar for (c) and (d) is the same.

4.3.4 A COMPARISON BETWEEN INDENTATION INDUCED DEFORMATION BEHAVIOR IN C-PLANE ZNO AND GAN CRYSTALS

GaN crystal also has the wurtzite structure, the same as ZnO crystal, and has been widely used in optoelectronic industry. However, high quality non-polar GaN crystal is hard to grow and expensive, so only *c*-plane GaN crystals were nanoindented here to study its induced plastic deformation, as well as to compare its deformation behavior with ZnO. Figure 4.11 shows the bright field images acquired from an indentation on *c*-plane

GaN crystals using the same indenter with a much higher load of 10^4 μN. These two images were taken from the same region with different diffraction conditions as marked by arrows. Comparing Fig. 4.11 with Fig. 4.7, two important phenomenons have been observed. First, the penetration depth of GaN (~100 nm) is smaller than that of ZnO (~200 nm) even though the applied normal loads for GaN (10^4 μN) is higher than ZnO (5×10^3 μN). It indicates that *c*-plane ZnO is "softer" than *c*-plane GaN, which is consistent with the reported hardness values (*c*-GaN ~12.3 GPa and *c*-ZnO ~6.5 GPa).[22, 30] Second, defect structure introduced by the indentation on *c*-GaN mainly consist of horizontal dislocation lines and inclined dislocation lines that have an angle of 63° with respect to the surface. This defect structure is similar with the one observed from Fig 4.7, indicating that the deformation mechanism of GaN is also predominated by the basal plane slip and $(1\bar{1}01)$ pyramidal plane slip, the same as the ZnO crystal.

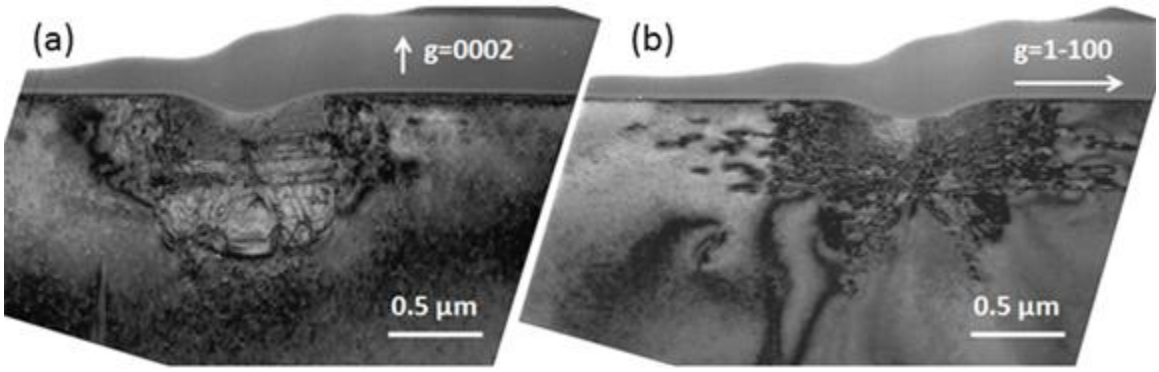

Fig. 4.11. Bight field TEM images showing the defects introduced by indentation on a c-plane GaN crystal. The diffraction condition used for imaging is marked as arrows.

4.4 DISCUSSION AND CONCLUSION

So, from the results presented above, indentation induced plastic deformation in the ZnO crystals with different surface facets can be visualized as the schematic diagram

in Fig. 4.12 and 4.13. Take the indentation on the m-plane ZnO crystal as the non-polar example. As shown in Fig. 4.12, when the conospherical indenter forces down onto the *m*-plane ZnO, it will generate radius stress to bulk material. This radius stress can be decomposed to three components – one is normal to the basal plane (S_n) and the other two are in basal planes (S_{i1} and S_{i2}). Considering our tip shape and size (the penetration depth is less than 15% of the tip radius), S_{i1} is much more significant than S_{i2} and $S_{n.}$ Also considering the possible silp systems in a wurtzite structure,[31] strain caused by S_{i1} and S_{i2} is relaxed in this case with the generation of dislocations introduced by basal plane slip. But since pyramidal slip is not observed in this case, strain caused by the normal component S_n could not get relaxed, and then build compressive strain besides the indentation along $\langle 0002 \rangle$ directions as well as the tensile strain besides the indentation along $\langle 11\bar{2}0 \rangle$ directions, as illustrated in Fig. 4.9 (b). Therefore, the strong emission observed from the CL mapping taken at 3.34 eV in Fig. 4.5 (b) is explained. The red-shift of the bound exciton transitions confirms that there is tensile stress in these regions.

While for the indentation of c-plane ZnO crystal that has a polar surface, S_n is much more significant than S_{i1} and S_{i2}, as shown in Fig. 4.13 (a), so it activated the $(1\bar{1}01)$ pyramidal slip planes in our indentation on the c-plane ZnO crystal. However, basal plane slipping is the primary slip in wurtzite structure; in other words, basal plane slipping is most easily to happen. From the observation, there are still some basal slips, as illustrated in Fig. 4.7, caused by S_{i1} and S_{i2} even though they are much smaller than $S_{n.}$ As we observed from indentations in non-polar ZnO crystals, dislocations originated from the basal plane slipping tend to propagate along *a*- directions, leading to the six-fold spikes as shown in Fig 4.12(b).

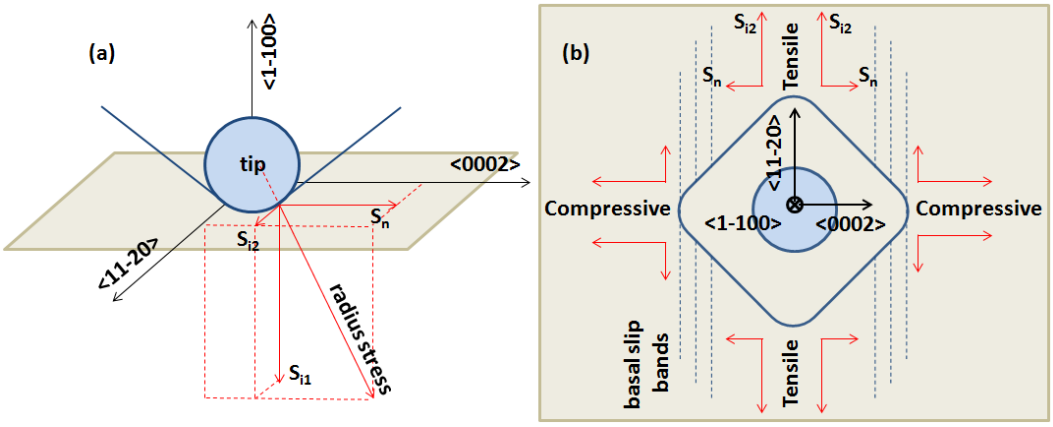

Fig. 4.12. A simple schematic diagram showing the interaction of a indentation tip with the m-plane wurtzite slip system. (a) is side view, and (b) is top view.

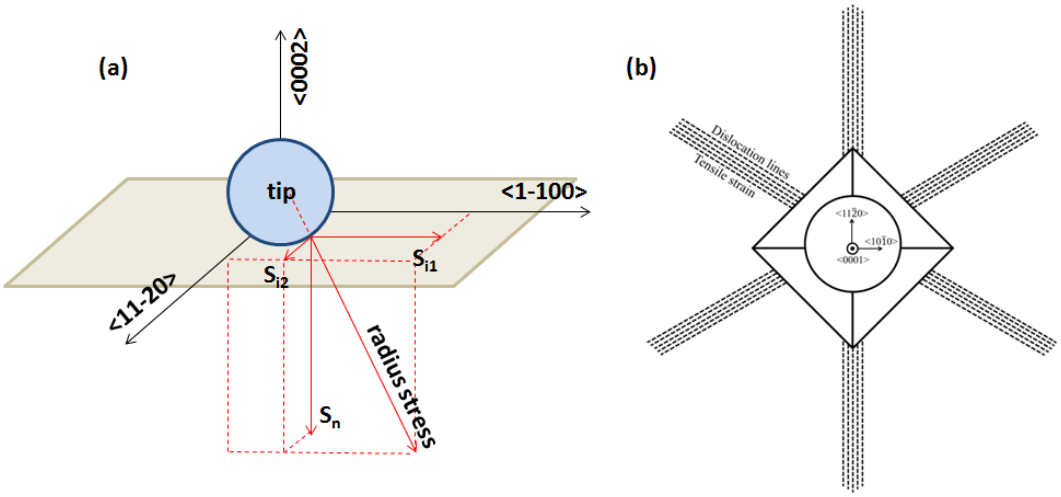

Fig. 4.13. A simple schematic diagram showing the interaction of a indentation tip with the c-plane wurtzite slip system. (a) is side view, and (b) is top view.

In summary, the mechanical deformation process induced by highly localized nanoindentation stress fields has been studied for polar (c-plane) and non-polar (a- and *m*-plane) ZnO single crystals. Hardness of non-polar ZnO turns out to be smaller than that of *c*-plane one. SEM, CL and TEM results reveals that the difference in the hardness

values is due to the orientation of the basal planes with respect to the indentation axis. The higher hardening rates of the *c*-plane are due to the nucleation of pyramidal dislocations, in addition to basal dislocations, which is the only slip system in the indentation on *a*- and *m*-plane ZnO single crystal. CL and TEM results also show the nature of the defects induced by indentation and the consequent effect on luminescence. It is confirmed that most dislocations introduced by indentation are screw type dislocations that formed by slipping in the basal planes along the $\langle 11\bar{2}0 \rangle$ directions. These dislocations are highly localized below the indentation, only propagating in indenter-contacted basal planes, and acting as nonradiative recombination centers. Compressive strains were introduced along $\pm c$ directions next to the indent, and tensile strains were introduced along $\pm a$ directions, modifying the crystal lattice and band gap. These results are important for understanding the mechanical properties of ZnO and will be valuable for the device fabrication. Also, by comparing the defect structure of nanoindented *c*-ZnO and *c*-GaN, it is found out that deformation mechanism in crystals is mainly determined by the crystalline structure even though these crystals have different the mechanical properties such as hardness. So the study on ZnO crystals with different facets also gives us a chance to explore the deformation mechanism in non-polar GaN crystals.

REFERENCE

[1] Y. I. Alivov, J. E. Van Nostrand, D. C. Look, M. V. Chukichev, and B. M. Ataev, Appl. Phys. Lett. **83**, 2943 (2003).

[2] Z. K. tang, G. K. L. Wong, P. Yu, M. Kawasaki, A. Ohtomo, H. Koinuma, and Y. Segawa, Appl. Phys. Lett. **72**, 3270 (1998).

[3] C. Soci, Z. Zhang, B. Xiang, S. A. Dayeh, D. P. R. Aplin, J. Park, X. Y. Bao, Y. H. Lo, and D. Wang, Nano Lett. **7**, 1003 (2007).

[4] F. Hamdani, A. Botchkarev, W. Kim, H. Morkoc, M. Yeadon, J. M. Gibson, S. –C. Y. Tsen, D. J. Smith, D. C. Reynolds, D. C. Look, K. Evans, C. W. Litton, W. C. Mitchel, and P. Hemenger, Appl. Phys. Lett. **70**, 467 (1997).

[5] X. Gu, M. A. Reshchikov, A. Teke, D. Johnstone, and H. Morkoc, Appl. Phys. Lett. **84**, 2268 (2004).

[6] A. Kobayashi, S. Kawano, Y. Kawaguchi, J. Ohta, and H. Fujioka, Appl. Phys. Lett. **90**, 041908 (2007).

[7] T. Wei, R. Duan, J. Wang, J. Li, Z. Huo, J. Yang, and Y. Zeng, Jpn. J. Appl. Phys., **47**, 3346 (2008).

[8] C. Noguera, J. Phys.: Condens Mater. **12**, R367 (2000).

[9] T. Makino, K. Tamura, C. H. Chia, Y. Segawa, M. Kawasaki, A. Ohtomo, H. Koinuma, Appl. Phys. Lett. **81**, 2355 (2002).

[10] T. Onuma, H. Amaike, M. Kubota, K. Okamoto, H. Ohta, J. Ichihara, H. Takasu, and S. F. Chichibu, Appl. Phys. Lett. **91**, 181903 (2007).

[11] J. W. Lee, J. H. Kim, S. K. Han, S. K. Hong, J. Y. Lee, S. I. Hong, and T. Yao, J. Cryst. Growth. **312**, 238 (2010).

[12] S. Yang, B. H. Lin, C. C. Kuo, H. C. Hsu, W. –R. Liu, M. O. Eriksson, P. –O. Hotz, S. –S. Chang, C. –H. Hsu, and W. F. Hsieh, Cryt. Growth Des. **12**, 4745 (2012).

[13] Y. Li, Y. Zhang, H. He, Z. Ye, J. Jiang, J. Lu, and J. Huang, Mater. Res. Bull, **47**, 2235 (2012).

[14] Y. Kawai, S. Ohsuka, M. Iwaya, S. Kamiyama, H. Amano, and Isamu Akasaki, J. Cryst. Growth, **311**, 2929 (2009).

[15] T. Kajima, A. Kobayashi, K. Ueno, K. Shimomoto, T. Fujii, J. Ohta, H. Fujioka, and M. Oshima, Jpn. J. Appl. Phys. **49**, 070202 (2010).

[16] S. O. Kucheyev, J. E. Bradby, J. S. Williams, C. Jagadish, and M. V. Swain, Appl. Phys. Lett. **80**, 956 (2002).

[17] M. J. Mayo, R. W. Siegel, Y.X. Liao, and W. D. Nix, J. Mater. Res. **7**, 973 (1992).

[18] J. E. Bradby, S. O. Kucheyev, J. S. Williams, C. Jagadish, M. V. Swain, P. Munroe, and M. R. Phillips, Appl. Phys. Lett. **80**, 4537 (2002).

[19] V. A. Coleman, J. E. Bradby, C. Jagadish, P. Munroe, P Y. W. Heo, S. J. Pearton, D. P. Norton, M. Inoue, and M. Yano, Appl. Phys. Lett. **86**, 203105 (2005).

[20] W. C. Oliver and G. M. Pharr, J. Mater. Res. **7**, 1564, (1992).

[21] J.R. Morris, H. Bei, G. M. Pharr, and E. P. George, Phys. Rev. Lett. **106**, 165502 (2011).]

[22] R. Navamathavan, K.-K. Kim, D.-K. Hwang, S.-J. Park, J.-H. Hahn, T. G. Lee, G.-S. Kim, Appl. Surf. Sci. **253**, 464 (2006).

[23] D. A. Lucca, M. J. Klopfstein, R. Ghisleni, and G. Cantwell, CIRP Annals – Manufac. Tech. **51**, 483 (2002).

[24] B. K. Meyer, H. Alves, D. M. Hofmann, W. Kriegseis, D. Forster, F. Bertram, J. Christen, A. Hoffmann, M. StraßBurg, M. Dworzak, and A. V. Rodina. Phys. Stat. Sol. (b) **241**, 231-260 (2004).

[25] A. M. Fisher, S. Srinivasan, R. Garcia, F. A. Ponce, S. E. Guaňo, B. C. Di Lello, F. J. Moura, and I. G. Solõrzano. Appl. Phys. Lett. **91**, 121905 (2007).

[26] D. G. Zhao, S. J. Xu, M. H. Xie, S. Y. Tong and Hui Yang, Appl. Phys. Lett. **83**, 677 (2003).

[27] A. Mang, K. Reimann, and St. Rübenacke, Sol. Stat. Commun. **94**, 251 (1995).

[28] S. Basu, and M. W. Barsoum, J. Mater. Res., **22**, 2470 (2007).

[29] David B. Williams and C. Barry Carter, *Transmission Electron Microscopy*, (Plenum press. NewYork and London).

[30] M. D. Drory, J. W. Ager III, T. Suski, I. Gregoryt, S. Porowski, Appl. Phys. Lett. **69**, 4044 (1996).

[31] S. Srinivasan, L. Geng, R. Liu, F. A. Ponce, Y. Narukawa, and S. Tanaka, Appl. Phys. Lett. **83**, 5187 (2003).

CHAPTER 5

EFFECT OF INTRODUCING ANTIMONY ON MICROSTRUCTURE OF GAINNAS THIN FILMS

This chapter describes a comprehensive study on the effect of introducing antimony (Sb) during the GaInNAs epitaxial growth. This work was carried out in collaboration with professor Ryuji Oshima and his colleagues at university of Tokyo. The samples were growth by atomic hydrogen-assisted molecular beam epitaxy in Tokyo; and the X-ray diffraction (XRD) results were provided by professor Oshima. My role in this work mainly involved the micro-structural characterization of the quaternary films using electron microscope and the analysis of chemical composition distribution in the films using scanning transmission electron microscopy (STEM) and energy dispersive X-ray (EDX) spectroscopy. The major results of this study have been published. *

(*)R. Oshima, J. Y. Huang, N. Miyashita, K. Matsubara, Y. Okada, and F. A. Ponce, "*Transmission electron microscope study of GaInNAs(Sb) thin films grown by atomic hydrogen-assisted molecular beam epitaxy*", Appl. Phys. Lett. **99**, 191907 (2011).

5.1 INTRODUCTION

The quaternary GaInNAs is a promising material system for the use in next generation multi-junction photovoltaic devices, such as solar cells,[1] because this material can be lattice matched to GaAs and Ge substrates, and they have a band gap in the 1.0 eV range that is complementary to those of other III-V and elemental semiconductors (Ge: 0.7 eV, GaAs: 1.4 eV, and GaInP: 1.8 eV).[2] Nowadays, lattice-matched AlInGaP/GaAs/GaInNAs/Ge monolithic tandem solar cells are desired in order to achieve conversion efficiency exceeding 45%.[3] However, the main roadblock to the development of these devices is the poor minority carrier diffusion lengths in GaInNAs, generally less than 0.1 μm, [4] well below the 3 μm desired for solar cells.[5] Therefore, it is necessary to achieve accurate control of the growth condition in order to improve compositional homogeneity and to prevent phase separation.[6–13] Furthermore, use of atomic hydrogen (H),[14] antimony (Sb),[15, 16] or bismuth[17] as a surfactant in molecular beam epitaxy (MBE) has been shown to be effective in obtaining better electrical and optical properties. This chapter reports a correlated study of the structural and compositional properties of GaInNAs(Sb) films using transmission electron microscopy (TEM).

5.2 EPERIMENTAL DETAILS

The GaInNAs thin films used in this study were grown on GaAs(001) substrates in an atomic H-assisted MBE with a nitrogen radiofrequency (rf) plasma source.[18] Figure 5.1 shows the schematic diagram of the sample structure. After a deposition of 250 nm thick GaAs buffer layer at 580 ℃, 100 nm thick $Ga_{0.92}In_{0.08}N_{0.013}As_{0.987}$ film and a 100 nm thick GaAs capping layer were grown at 520 ℃. Two samples were grown

respectively, with/without adding the Sb beam flux during the 100 nm thick GaInNAs layer growth. The Sb beam flux was 3×10^{-8} Torr, which resulted in ~1% of Sb incorporation as determined by secondary ion mass spectroscopy (SIMS).[15] High-resolution x-ray diffraction (HR-XRD), TEM, and energy dispersive X-ray (EDX) spectroscopy were used to determine the degree of compositional uniformity. Cross-sectional TEM specimens were prepared by conventional mechanical polishing and dimpling followed by argon ion-beam milling at liquid nitrogen temperature with low energy of 3.5 keV in a precision ion polishing system. Before the sample milling was finished, lower-energy of ~2 keV ion beams were briefly used to clean the surface. The TEM characterization was carried out using a JEM-4000EX high-resolution electron microscope operated at 400 kV with a structural resolution of ~1.7 angstrom. And the STEM and EDX were carried out using a JEOL 2010FX electron microscope. All samples were prepared for observation along <110> zone axis projections.

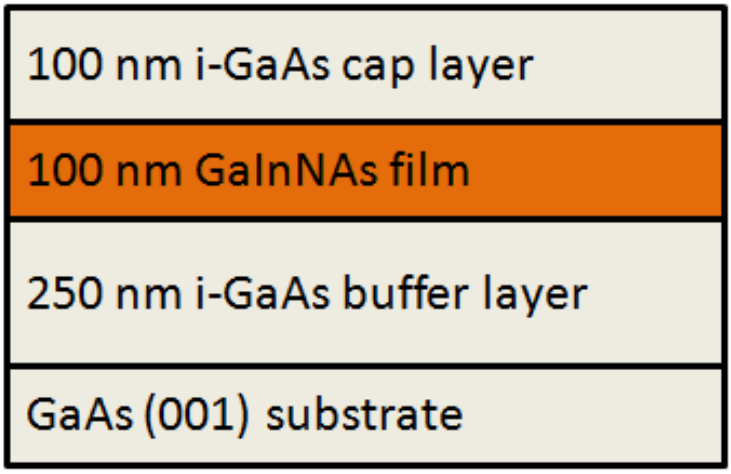

Fig. 5.1. A schematic illustration of the MBE-growth of the quaternary GaInNAs sample overall structure.

5.3 RESULTS AND DISCUSSION

5.3.1 X-RAY DIFFRACTION

Figure 5.2 shows the XRD spectra around (004) reflection in a ω-2θ geometry measured for (a) GaInAs, (b) GaInNAs, and (c) GaInNAsSb, respectively. The solid lines are the experimental results while the dashed lines are the simulated ones. The main peak observed at 33.01 °is the (004) peak from the GaAs substrate. The other dominating peak position for each spectrum, which is around 32.6° ~ 32.9°, is from the corresponding GaInAs and GaInNAs expitaxy. The peak position for (b) was shifted to a larger angle of 32.86° compared to (a) of 32.64° according to the incorporation of nitrogen, while the shift toward smaller angle of 32.61° for (c) is due to the incorporation of antimony into the layer. The full width at half maximum (FWHM) of these peaks are (a) 152.2 sec, (b) 162.9 sec, and (c) 148.9 sec, in which the smallest FWHM for (c) indicates the best crystalline quality that is mainly due to the incorporation of Sb into the layer. The lattice mismatch is less than 1.1% for all these three samples, which indicates that the active layer does not exceed the critical thickness for generation of dislocations.[19] The experimental curves with well defined fringe peaks are well fitted to simulated curve for all samples. In addition, the streak patterns in reflection high energy electron diffraction, which was observed during growth, strongly support two dimensional layer-by-layer growths even though under the relatively high growth temperature of 520 ℃ compared to other reports.[12, 13]

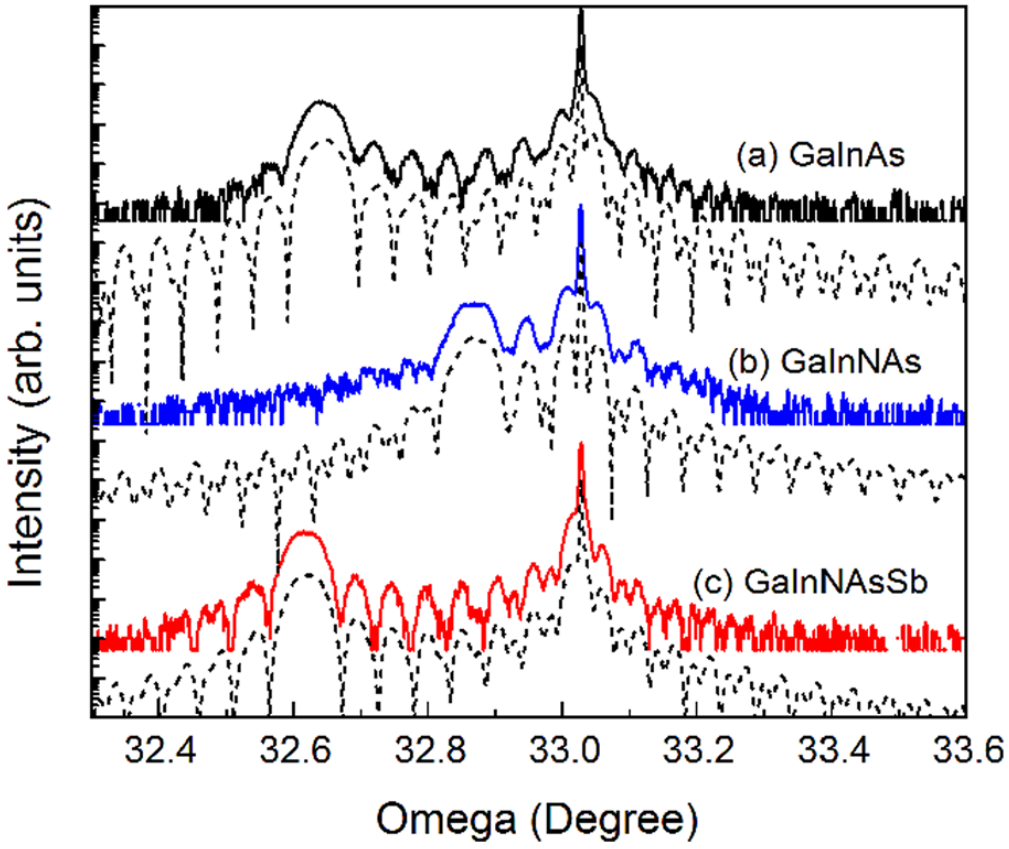

Fig. 5.2. Colored lines are symmetric (004) X-ray diffraction patterns for (a) GaInAs, (b) GaInNAs, and (c) GaInNAs(Sb). The dashed lines are simulated curves for each sample.

5.3.2 MICROSTRUCTURAL CHARACTERIZATION USING TEM

To investigate the effect of introduction of Sb on the GaInNAs growth, a series of microstructural characterization using transmission electron microscope was exerted on the sample (b) GaInNAs, and (c) GaInNAsSb. Figure 5.3 shows the bright-field cross sectional TEM images taken with diffraction condition of $\boldsymbol{g}$=(002). No dislocations have been observed in both samples, but it reveals strong striation features and contrast fluctuations throughout the GaInNAs layer in Fig. 5.3(a). While GaInNAs layer grown with antimony exhibits uniform contrast throughout as shown in Fig. 5.3(b). Two-dimensional growth with striation is associated with compositional fluctuation on the

growth front. Especially, horizontal striations indicate elemental segregation during growth and abrupt incorporation into a layered structure.

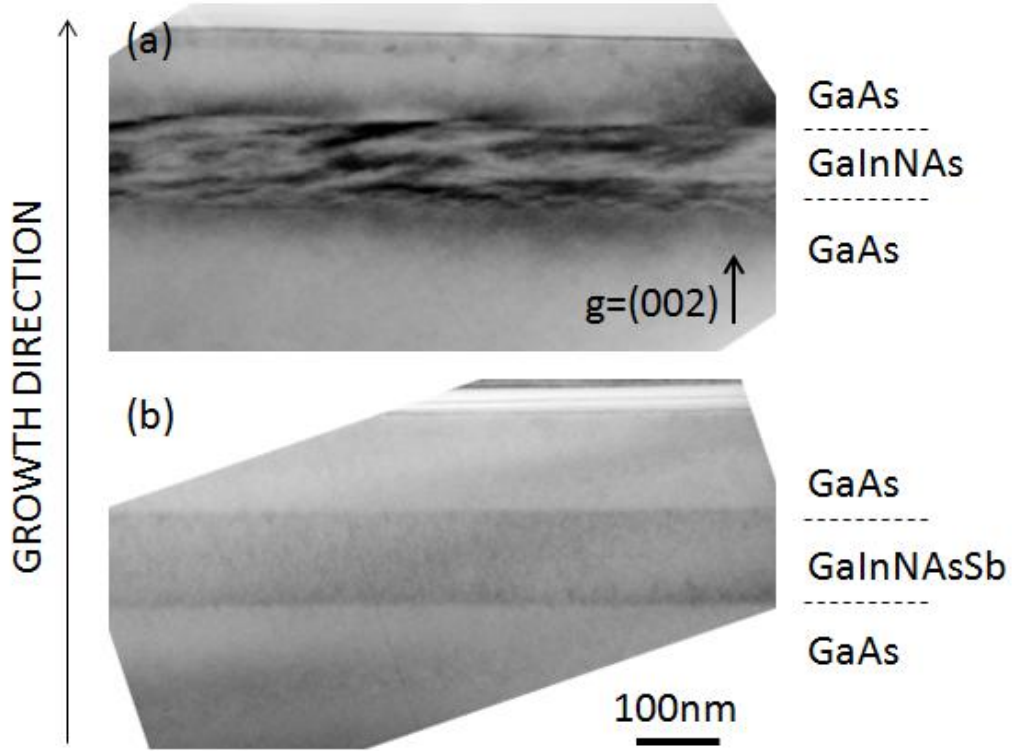

Fig. 5.3. Bright-field cross sectional TEM images of (a) GaInNAs, and (b) GaInNAs(Sb) taken with g=(002).

The similar phenomenon was also observed in Fig. 5.4, which is high-resolution lattice image taken along the [110] zone axis of (a) GaInNAs and (b) GaInNAsSb layer, respectively. Figure 5.4(b) exhibits uniform contrast throughout, in contrast with clearly strong contrast variation in Fig. 5.4(a). The strong contrast variation in the HR images in (a) can be attributed to strain variations due to local compositional fluctuations caused by elemental segregation of indium and gallium (bright and dark regions), in agreement with the diffraction contrasts.

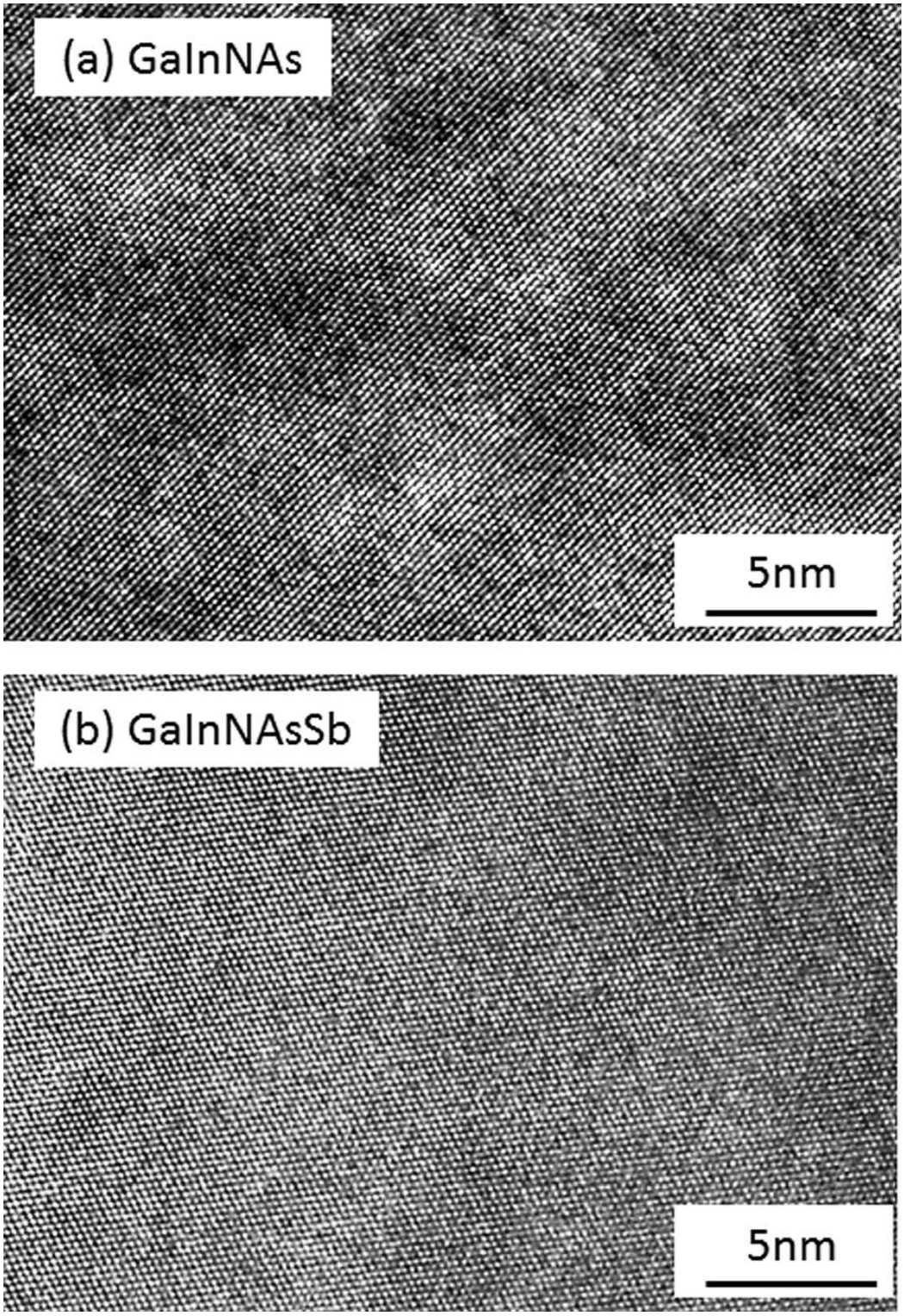

Fig. 5.4. High resolution lattice images of (a) GaInNAs, and (b) GaInNAs(Sb).

5.3.3 COMPOSITIONAL PROPERTIES

A series of correlated study on the compositional properties of these two GaInNAs samples was done by high-angle annular dark-field (HAADF) STEM imaging and EDX line scan spectra, as shown in Fig. 5.5.

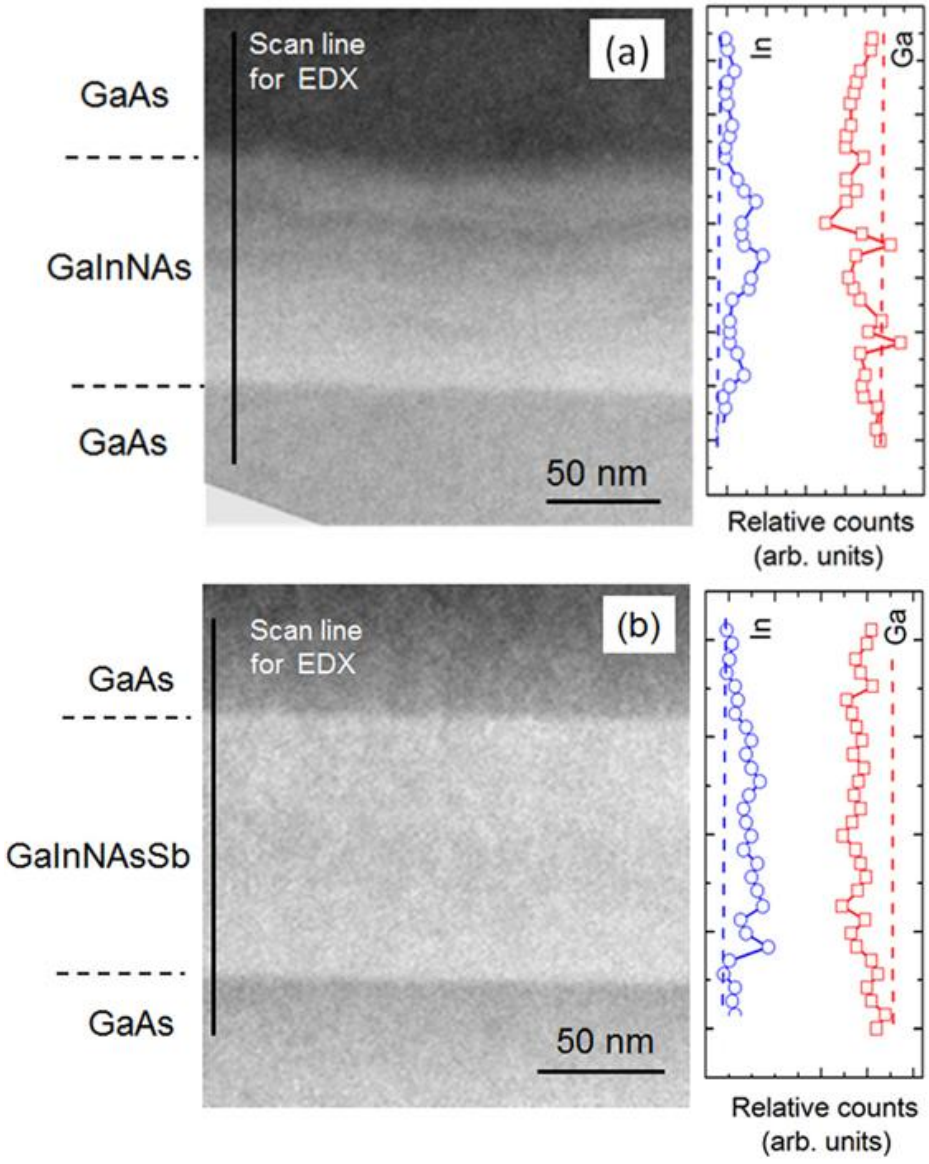

Fig. 5.5. STEM images and EDX line scan spectra of (a) GaInNAs, and (b) GaInNAs(Sb).

From the STEM images on the left, GaInNAs film grown without Sb shows a strong undulation at the upper heterointerface with GaAs cap and contrast variation throughout the film, while the GaInNAs film grown with Sb exhibits abrupt interface and uniform contrast in the film. Meanwhile, the EDX profile on the right (In and Ga signals) obtained by the vertical line scan marked in the STEM images clarifies the character and the degree of the compositional fluctuation existing in the epilayer. The EDX curve for (b) GaInNAs(Sb) exhibit steady In and Ga counts. But the EDX curves for (a) GaInNAs shows some local counts fluctuations, reflecting the local elemental distribution fluctuation which is in agreement with the results from the contrast modulation. Also, both curves follow an opposite trend, i.e. positions with high In intensity correspond to low Ga intensity and vice versa.

In a quaternary alloy, the nearest-neighbor bond configuration is determined by minimizing the alloy free energy. The local strain is produced by the difference in bond lengths between the corresponding III-V atom combinations. During the epitaxial growth, the adatoms are able to relieve local strain toward the free surface. Therefore, the development of nearest neighbor configuration is theoretically more driven by maximizing the cohesive bond energy than minimizing the local strain.[20] The cohesive energy of the respective binary solids follow the sequence GaN>InN>GaAs>InAs (2.24, 1.93, 1.63, and 1.55 eV per bond, respectively),[21] so the formation of Ga-N and In-As bonds should be preferred. Kong et. al. have confirmed these consideration experimentally by using electron energy-loss spectroscopy.[12] These composition fluctuations are the driving force for the morphological instabilities at the interface. Further, higher growth temperature is responsible to the enhancement of surface

mobilities of adatoms, resulting in a severe compositional fluctuation. However, exposure of Sb, during the growth, results in a reduction of the adatom mobility due to lowering the barrier for chemical bonding, which is responsible for a lower probability to generate the favorable bonds.[22] This is why exposure of Sb dramatically improves compositional uniformity within the film.

5.4 CONCLUSION

In summary, the effect of Sb exposure during growth on the structural properties of GaInNAs alloy has been systematically investigated in this chapter. For the growth of all samples, H-MBE has been employed. Both (S)TEM and EDX results confirm that introduction of antimony during growth of GaInNAs enhances overall compositional uniformity because adding antimony could reduce the adatom mobility due to lowering the barrier for chemical bonding, which is responsible for a lower probability to generate the favorable bonds. These enhancements of structural properties of GaInNAsSb thin film encourage the feasibility of 1.0 eV range subcell in four junction solar cells.

REFERENCE

[1] M. Kondow, K. Uomi, A. Niwa, T. Kitatani, S. Watahiki, Y. Yazawa, Jpn. J. Appl. Phys. **35**, 1273 (1996).

[2] S. R. Kurtz, A. A. Allerman, E. D. Jones, J. M. Gee, J. J. Banas, B. E. Hammons, Appl. Phys. Lett. **74**, 729 (1999).

[3] M. Yamaguchi, T. Takamoto, K. Araki, N. Ekins-Dauks, Sol. Energy **79**, 78 (2005).

[4] S. R. Kurtz, A. A. Allerman, C. H. Seager, R. M. Sieg, E. D. Jones, Appl. Phys. Lett. **70**, 700 (2000).

[5] D. J. Friedman, Current Opinion in Solid state and Material Science **14**, 131 (2010).

[6] D. B. Jackrel, S. R. Bank, H. B. Yuen, M. A. Wistey, J. S Harris Jr, A.J. Ptak, S. W. Johnston, D. J. Friedman, S. R. Kurtz, J. Appl. Phys.**101**, 114916 (2007).

[7] Y. Shimizu, N. Miyashita, Y. Mura, A. uedono, Y. Okada, J. Crystal Growth. **301-302**, 579 (2007).

[8] L. Borkovska, O. Yafanov, O. Gudymenko, S. Johnson, V. Kladko, N. Korsunska, T Kryshtab, Y. Sadofyev, Y.-H. Zhang, Thin Solid Films **515**, 786 (2006).

[9] Y. Qui, S.A. Nikisin, H. Temkin, V.A. Elyukhin, Y.A. Kudriavtsev, Appl. Phys. Lett. **70**, 2831 (1997).

[10] T. Hakkarainen, E.-M. Pavelescu, J. Likonen, Physica E **32**, 266 (2006).

[11] S. R. Bank, H. B. Yuen, H. Bae, M. A. Wistey, J.S. Harris Jr., Appl. Phys. Lett. **88**, 221115 (2006).

[12] X. Kong, A. Trampert, E. Tournie, K.H. Ploog, Appl. Phys. Lett. **87**, 171901 (2005).

[13] T. Gugov, V. Gambin, M. Wistey, H. Yuen, S. Bank, J. S. Harris. Jr., J. Vac. Sci. Technol. B **22**, 1588 (2004).

[14] Y. Kamikawa-Shimizu, S. Niki, Y. Okada, Solar Energy Materials and Solar Cells, **93**, 1120 (2008).

[15] N. Miyashita, S. Ichikawa, Y. Okada, J. Crystal Growth **311**, 3249 (2009).

[16] S. R. Bank, H.P. Bae, H.B. Yuen, M.A. Wistey, L.L. Goddard, J.S. Harris Jr., Electron. Lett. **42**, 156 (2006).

[17] A.J. Ptak, R. France, C.-S. Jiang, R.C. Reedy, J. Vac. Sci. Technol. B **26**, 1053 (2008).

[18] Y. Shimizu, N. Kobayashi, A. Uedono, Y. Okada, J. Crystal Growth **278**, 553 (2005).

[19] M. Tabuchi, S. Noda, and A. Sasaki, J. Crystal Growth **115**, 169 (1991).

[20] K. Kim, A. Zunger, Phys. Rev. Lett. **86**, 2609 (2001).

[21] W.A. Harrison, Electronic Structure and the Properties of Solids (Dover, New York, 1989), pp. 175-176.

[22] X. Kong, A. Trampert, K.H. Ploog, Micron **37**, 465 (2006).

CHAPTER 6

COMPOSITIONAL INSTABILITY IN INALN/GAN LATTICE-MATCHED EPILAYERS

This chapter describes a comprehensive study on some fundamental issues commonly existing the in group III nitride alloys, such as the compositional fluctuation, extensive dislocation, etc. This work was carried out in collaboration with Professor T. Egawa and his colleagues at Nagoya Institute of Technoogy in Japan. They provided the InAlN samples grown by metal organic chemical vapor deposition in Japan. My role in this work mainly involved the micro-structural characterization of films using electron microscope and the analysis of chemical composition distribution in the films using scanning transmission electron microscopy (STEM) and energy dispersive X-ray (EDX) spectroscopy. The cathodoluminescence results were provided by a previous group member Dr. Ti Li and the Rutherford back-scatting spectrometry results were provided by a previous group member Dr. Qiyuan Wei. Some results of this study have been published. *

(*)Q. Y. Wei, T. Li, J. Y. Huang, Z. T. Chen, T. Egawa, and F. A. Ponce, "*Compositional instability in InAlN/GaN lattice-matched epitaxy",* Appl. Phys. Lett. **100**, 092101 (2012).

6.1 INTRODUCTION

The ternary-alloy material system mainly consisting of three Group III nitride materials - GaN, InN and AlN, are widely used in electronic and optoelectronic devices. However, because of the discrepancy of the optimum growth temperature for these three nitride materials, it is challenging to grow thick, uniform, and high quality ternary films due to the tendencies towards spinodal decomposition.[1,2] Particularly, growing thick group III nitride ternary alloys is extremely difficult by conventional growth technologies such as MBE and MOCVD due to difficulties in maintaining uniform film morphology, good crystalline structure, as well as device-quality optical and electrical properties.[3] Compositional instabilities in InGaN/GaN and AlGaN/GaN systems have been reported and explained by a compositional pulling effect where, during the initial deposition of InGaN or AlGaN on GaN, the incorporation of In or Al atoms is impeded by lattice mismatch strain.[4,5] Therefore, considering the lattice mismatch effect, $In_xAl_{1-x}N$ alloy with x~18% has recently received much attention because they are lattice matched to GaN, that is usually introduced as a buffer layer. Minimizing the lattice mismatch is expected to provide better structural characteristics and the possibilities to grow thick InAlN layers for distributed Bragg reflectors and optical waveguides.[6,7] So, in this chapter, I will report a study on the compositional instability in a lattice matched thick InAlN epilayer grown on GaN, triggered by the presence of threading dislocations.

6.2 EPERIMENTAL DETAILS

The InAlN epilayers described in this chapter were grown on GaN at ~800 ℃ by MOCVD using a Taiyo Nippon Sanso SR2000 system.[8] We studied two samples with different thickness (140 nm and 500 nm) to investigate the effect of thickness on the

structural and optical properties of InAlN films on lattice-matched GaN substrates. The microstructure of these samples was studied by TEM, in a Philips CM200 instrument operating at 200KV and a JEOL 4000 EX instrument operating at 400KV. The chemical composition of the epilayers was tested by RBS and STEM, in a JEOL 2010F instrument operating at 200KV. The TEM specimens were prepared by mechanical wedge-polishing, followed by ion milling in a cold stage to minimize indium diffusion and phase separation. Cathodoluminescence spectra were acquired at near liquid-helium temperatures in a scanning electron microscope.

6.3 RESULTS AND DISCUSSION

Figure 6.1 shows the RBS spectra of InAlN/GaN samples. The expected He scattering energies by indium and aluminum atoms in our measurement are 1.741 and 1.105 MeV, respectively, and are identified in the figure with vertical lines. These values are calculated based on the energy and momentum conservation during the Rutherford backscattering process. Because for a fixed experimental setup, the chemical composition of element A and B in the same layer can be determined by their scattering yield as $\frac{Y_A}{Y_B} = \frac{N_A Z_A^2}{N_B Z_B^2}$; Bring the yield ratio of Al/In (~0.320) obtained from the RBS spectrum of 140nm-thick InAlN epilayer, the indium content has been calculated to be 18.0% using the equation. However, there is no single value of the In/Al yield ration due to a step profile appearing in the RBS spectrum of 500 nm-thick InAlN epilayer. It indicates that for the thick InAlN epilayer, the chemical composition has an abrupt change at certain depth, above which the indium content decreases from ~18% to 10%.

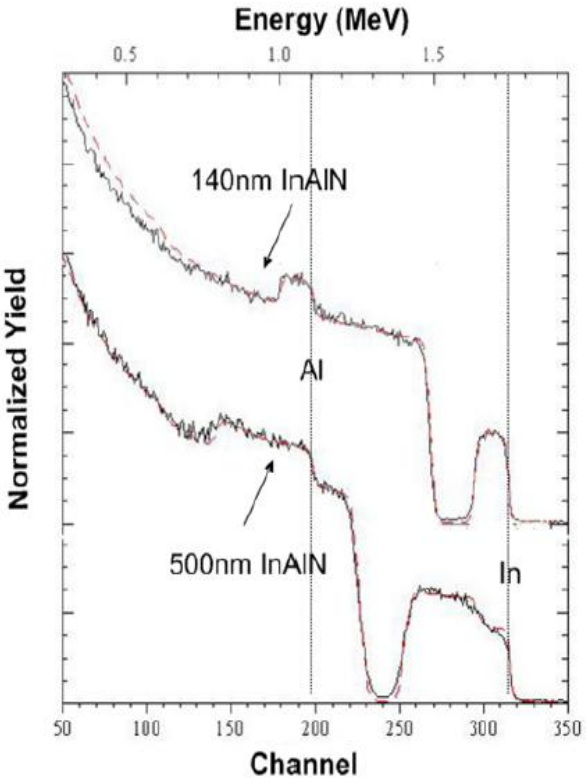

Fig. 6.1. Rutherford backscattering spectra of InAlN epilayers with thickness of 140nm and 500nm. Solid lines are experimental data and dashed lines are simulated ones.

The energy-dispersive X-ray (EDX) spectroscopy acquired from different region shown in Fig. 6.2 also displays the compositional difference in the thick InAlN epilayer. The EDX spectroscopy acquired from the bottom part of the 500 nm-thick InAlN layer gives the indium content of 11.4%, which is larger than 8.96% that is obtained from the top of the layer. The absolute value of composition is different from the RBS results and maybe not accurate, due to the lack of standard samples with known composition for calibration. The trend of this compositional change is consistent with the RBS results.

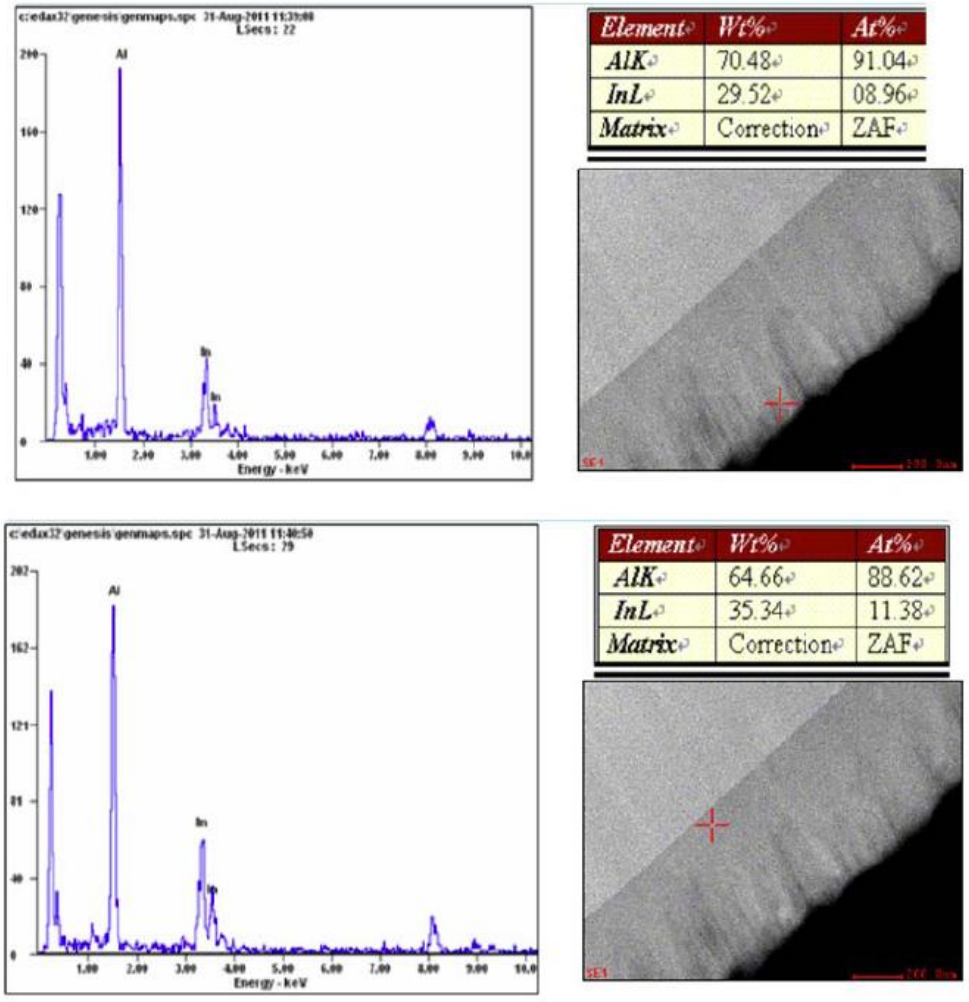

Fig. 6.2. Energy-dispersive X-ray spectroscopy acquired from different regions in the 500nm-thick InAlN epilayer as marked with cross, as shown in the images on the right.

Cross-sectional TEM study also shows the existence of sub-layers in the 500nm-thick InAlN film but not in the 140 nm-thick InAlN film. Figure 6.3 is g/3g dark-field images for the 140 nm and 500 nm thick InAlN samples. The image for the 140nm-thick layer in Fig. 6.3(a) exhibits relatively uniform contrast, while the image for 500 nm-thick layer in Fig. 6.3(b) exhibits an abrupt contrast change on the top. Both images display some threading dislocations in the epilayer. However, in the 140 nm-thick layer, these

threading dislocations distribute relatively uniform with an average density of ~$2\times10^9/cm^2$ and open up at ~80nm above the InAlN/GaN interface. In the 500 nm-thick layer, the defect density increase rapidly beyond a thickness of ~200nm.

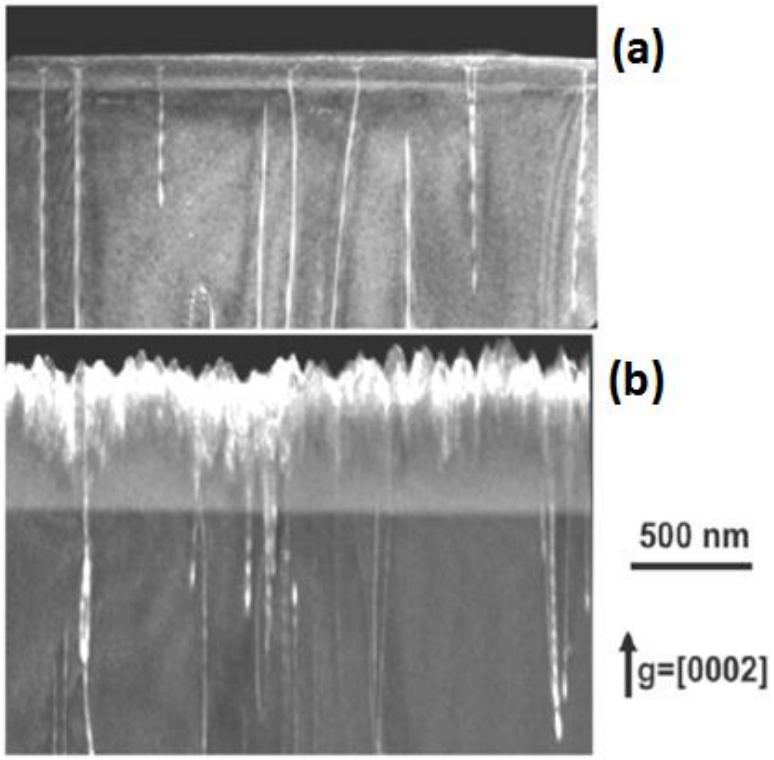

Fig. 6.3. Cross-section g/3g dark field TEM images of InAlN epilayers grown on GaN, with different thickness (a) 140 nm, and (b) 500 nm.

To fully understand the formation of the sub-layers in the 500 nm-thick InAlN sample, a series of microstructure analysis was tested as shown in Fig. 6.4. Figure 6.4(a) and (b) are dark field TEM images taken with two different standard diffraction conditions for hexagonal structure at low magnification, showing the whole structure including the GaN buffer layer and the 500 nm-thick InAlN layer. These two images demonstrate that most of the dislocations are visible under $\boldsymbol{g}$ = [0002] condition, indicating the predominance of screw and mixed type dislocations. They have Burgers

vectors ***c*** and ***c+a***, respectively, where ***a*** and ***c*** are the unit cell vectors in the wurtzite structure. [9] The ratio of mixed type to pure screw type dislocations is found to be ~1:1 from the diffraction contrast analysis. Figure 6.4(c) and (d) are bright field images taken with similar diffraction conditions at higher magnification mainly showing the microstructure of the 500 nm-thick epilayer. Dislocations in the 500 nm-thick InAlN layer were observed to open up laterally within the first ~ 100 nm above the InAlN/GaN interface, forming V-grooves with a divergence angle of ~ 36 °, which is close to $\{1\bar{1}01\}$ facets. Similar dislocation openings were also observed at the tip of some threading dislocations in the 140 nm-thick InAlN layer in Fig. 6.3(a). The fan-like regions originating from other dislocations in the vicinity but not contained in the thin TEM foil in Fig. 6.4 (of estimated cross-section thickness of ~ 80 nm) coalesce at a distance of ~ 200 nm above the InAlN/GaN interface. Selected area diffraction pattern acquired from the top part of the 500 nm-thick layer, in Fig. 6.4(e), displays two distinct sets of diffraction patterns – a set of small diffraction spots and a set of bigger disks. The spot and disk can be seen more clearly in the magnified inset. We believe that the small spot set is corresponding to the bottom sub-layer with uniform composition, while the larger disks is corresponding to the top sub-layer that constitutes the largest fraction of the area selected for diffraction. It is noticeable that the large disk is elongated along the $[11\bar{2}0]$ axis indicating various lateral dimensions of the crystallites responsible for this reflection. Also the large disk is displaced from the small spot along the [0001] direction, indicating the lower indium content in the top sub-layer than in the bottom sub-layer, which is consistent with the RBS and EDX results.

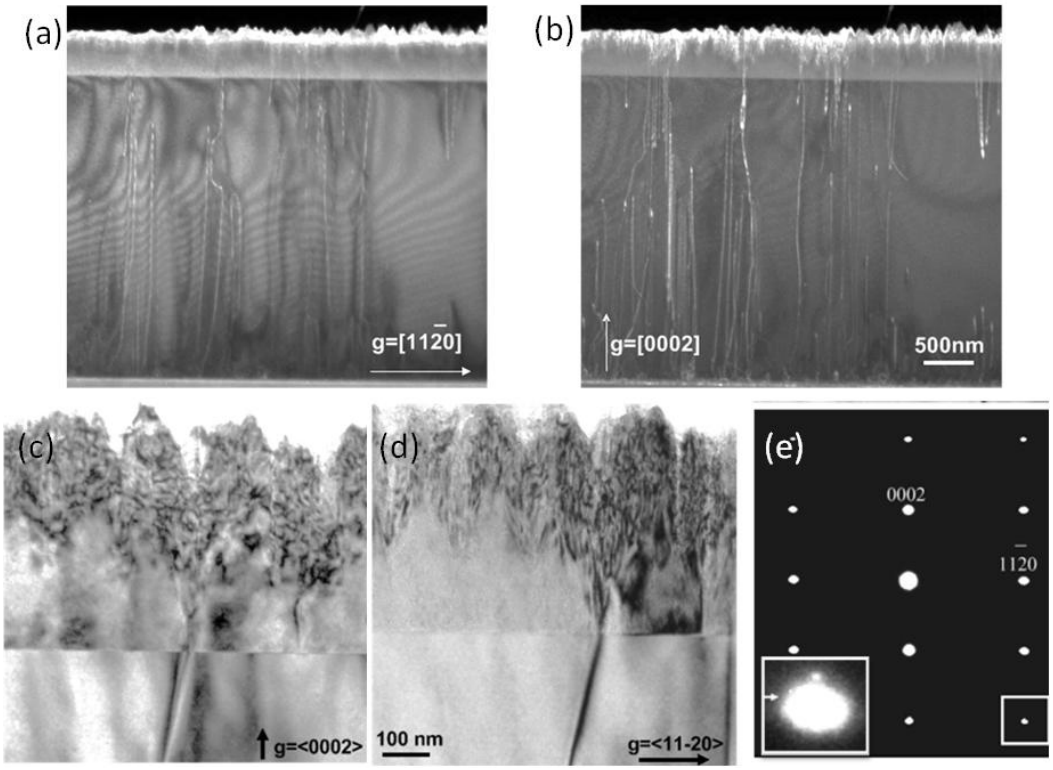

Fig. 6.4. Cross-section TEM images of 500 nm-thick InAlN epilayers grown on GaN, with different diffraction conditions and magnifications (a)-(d), and selected area diffraction pattern acquired from the top part of this epilayer (e).

Optical characteristics of these two samples were assessed by CL spectra, in Fig. 6.5, using an electron accelerating voltage of 2.5 keV. The purpose of using such relatively low voltage is to let the electron beam interact mostly with the near-surface region where the InAlN epilayer instead of the GaN substrate is. From the spectra, emission of InAlN from the 500 nm-thick layer is observed to be much broader than that from the 140 nm-thick layer. It indicates that the thicker InAlN layer has more degraded crystal quality and/or higher density of defects. Also, the center of the InAlN emission from the 500 nm-thick layer is red-shifted from the one from the 140 nm-thick layer, indicating the overall indium content in the thicker layer is lower.

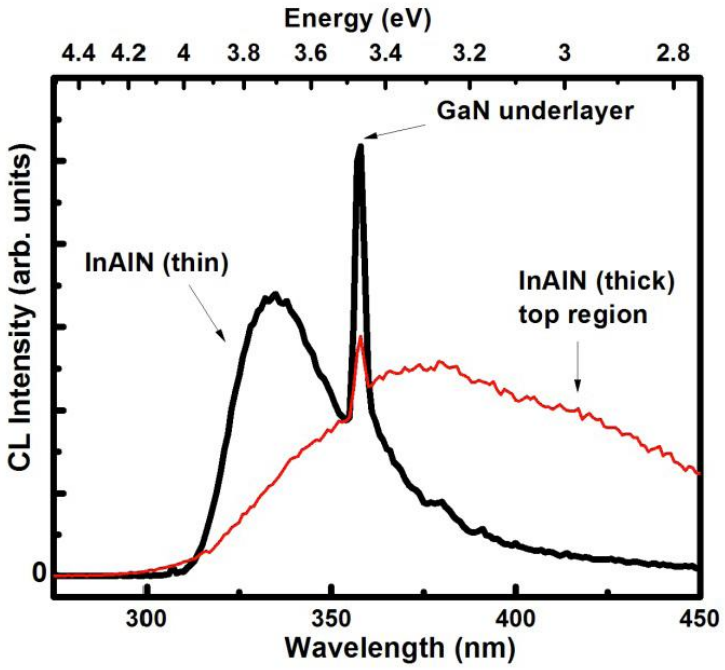

Fig. 6.5. Cathodoluminescence spectra from InAlN epilayers with different thickness. (the black one is from 140 nm-thick layer; the red one is from 500 nm-thick layer)

So, from the micro-structural analysis as well as the optical characteristic described above, the compositional variation in the 500 nm-thick InAlN layer can be summarized as follows. InAlN film with indium composition of ~18% was firstly grown on GaN in which threading dislocations open up during growth due to the strain energy associated with the large Burgers vector, developing $\{1\bar{1}01\}$ facets.[10, 11] After the threading dislocation opening, crystallites with a lower indium composition of ~ 10% nucleate heterogeneously at the inclined facets of the open-core dislocations. The compositional change of indium content has been verified by the RBS and EDX results. No indium precipitates were detected. We attribute the drop in indium content to the sequential growth on an inclined facet of wurtzite structure. More specifically speaking, the compositional pulling effect requirs an Al-rich gas phase for c-plane growth, but as

the film grows thicker, the screw threading dislocations open up due to the local strain generated by random-alloy fluctuations, and these steady opening present inclined facets that allows higher Al incorporation and an increase in growth rate. These observations in InAlN films are consistent with a model proposed by Northrup et al. for the formation of pits in GaN and its effect on indium incorporation during growth of InGaN.[12]

Comparing out results with the study by Zhou et.al. [13] on the InAlN thin film with thickness of ~50 nm grown by MBE on GaN, they observed the formation of a vertical honeycomb structure due to the lateral phase separation. But materials grown by MBE typically exhibit higher dislocation density, and growth happens at lower temperatures (465-480 ^{o}C) while the MOCVD gowth happens at around 800 ^{o}C.

6.4 CONCLUSION

In InAlN/GaN lattice-matched epitaxy, compositional instability has been observed when the InAlN epilayer is grown thick enough. This compositional variation is found to be triggered by the presence of threading screw dislocations that open up into a faceted inverted pyramidal shape. InAlN crystallites with lower indium content nucleate heterogeneously on the facets of coreless dislocations. Thus, two regions with distinct chemical composition and micro-structural features are formed. The degraded crystal quality results in a defect-related broad optical emission. The overall lower indium content leads to a red-shift of the InAlN emission center.

REFERENCE

[1] F. A. Ponce, S. Srinivasan, A. Bell, L. Geng, R. Liu, M. Stevens, J. Cai, H. Omiya, H. Marui, and T. Tanaka, Phys. Stat. Sol. B **240**, 273 (2003).

[2] V. G. Deibuk and A. V. Coznyi, Semiconductors. **39**, 623 (2005).

[3] J. Phillips et al, Laser Photonics Rev. **1**, 307 (2007).

[4] S. Pereira, M. R. Correia, E. Pereira, K. P. O'Donnell, C. Trager-Cowan, F. Sweeney, and E. Alves, Phys. Rev. B **64**, 205311 (2001).

[5] M. Hao, H. Ishikawa, T. Egawa, C. L. Shao, and T. Jimbo, Appl. Phys. Lett. **82**, 4702 (2003).

[6] J. F. Carlin and M. Ilegems, Appl. Phys. Lett. **83**, 668 (2003).

[7] R. Butté, J.-F. Carlin, E. Feltin, M. Gonschorek, S. Nicolay, G. Christmann, D. Simeonov, A. Castiglia, J. Dorsaz, H. J. Buehlmann, S. Christopoulos, G. Baldassarri Höger Von Högersthal, A. J. D. Grundy, M. Mosca, C. Pinquier, M. A. Py, F. Demangeot, J. Frandon, P. G. Lagoudakis, J. J. Baumberg, and N. Grandjean, J. Phys. D **40**, 6328 (2007).

[8] Z. T. Chen, S. X. Tan, Y. Sakai, and T. Egawa, Appl. Phys. Lett. **94**, 213504 (2009).

[9] F. A. Ponce, D. Cherns, W. T. Young, and J. W. Steeds, Appl. Phys. Lett. **69**, 770 (1996).

[10] D. Cherns, W. T. Young, J. W. Steeds, F. A. Ponce, and S. Nakamura, J. Crystal Growth. **178**, 201 (1997).

[11] D. Cherns, W. T. Young, J. W. Steeds, F. A. Ponce, and S. Nakamura, Phil. Mag. A **77**, 273 (1998).

[12] J. E. Northup, L. T. Romano, and J. Neugebauer, Appl. Phys. Lett. **74**, 2319 (1999).

[13] L. Zhou, D. J. Smith, M. R. Mccartney, D. S. Katzer, and D. F. Storm, Appl. Phys. Lett. **90**, 081917 (2007).

CHAPTER 7

SUMMARY AND FUTURE WORK

7.1 SUMMARY

In this dissertation, the microstructural and optical properties of some common II-VI and III-V compound semiconductor materials have been systematically investigated using transmission electron microscopy (TEM) and cathodoluminescence (CL) as well as some other techniques.

In chapter 3, the microstructure of (001) InP singe crystals scratched with a small diamond tip in an atomic force microscope has been studied as a function of applied normal force and crystalline directions. It is found that within the plastic deformation range, the scratch surface of the InP crystal conforms the tip shape by the formation of crystal slip steps along {111} planes. The slip of {111} planes produces dislocations deep in the bulk of the material. The onset of dislocation nucleation was observed to be different along the <100> and <110> scratch directions. And the plastic flow is always deeper when scratching along the <110> direction for a given normal force. This has been explained by the interplay between normal and lateral forces in the <110>{111} slip system. High strain fields observed in <100> scratches indicate hardening due to locking of dislocations gliding on different slip planes. Reverse plastic events have been observed in <110> scratches with a normal force of 120 μN, that manifest themselves in the form of pop-up events that result from recovery of stored compressive elastic strain.

In chapter 4, nanoindentation-induced plastic deformation has been studied in *c*-, *a*-, and *m*-plane ZnO single crystals; and *c*-plane GaN crystals, to investigate the deformation mechanism in hexagonal structures. TEM results reveal that the prime

deformation mechanism is the nucleation of slip on basal planes for indentations on non-polar ZnO crystals, and on pyramidal plus basal planes for *c*-plane ZnO and GaN. The stain field induced by this deformation is built along particular directions. Dislocations generated are mostly of the screw-type; they are perfect dislocations with Burgers vector of $1/3\langle 11\bar{2}0\rangle$. No evidence of phase transformation or cracking was observed in these materials. CL imaging reveals a quenching of the near band-edge emission due to deformation-produced defects that act as non-radiative recombination centers.

In chapter 5, the effect of introducing antimony during the growth of GaInNAs has been discussed. With the exposure to minute levels of antimony during growth, GaInNAs epilayers exhibit uniform chemical composition. While the one without antimony exposure show two-dimensional growth with striation features associated with compositional fluctuation and nanometer scale elemental segregation. It is found out that antimony atoms can suppress the surface mobilites of adatoms resulting in a lower probability to generate the favored bonds, such as Ga-N and In-As, then improving compositional uniformity within the film.

In chapter 6, compositional inhomogeneity in ternary InAlN epilayers with different thickness has been presented. It is found that the lattice-matched InAlN epitaxial films grown on GaN exhibit chemical instability when the InAlN layer is grown beyond a certain thickness. In a 500nm thick InAlN film on GaN, two sub-layers with different indium content were observed, and their interface is associated with the generation of threading screw dislocations. The screw dislocations open up into a faceted inverted pyramidal shape that allows higher Al incorporation. The top sub-layer tends to have

lower indium than the bottom layer due to elemental segregation (so-called pulling effects).

7.2 FUTURE WORK

In this dissertation, we have reported on the mechanical deformation in several semiconductor single crystals. This work has been done on materials that were controllably deformed by nanoindentation, In actual practice, however, there are always films and epilayers involved and substrate in a real device structure. The stress field between the substrate and the different layers, can change the deformation response to the external load. So it is also essential to study the mechanical deformation in films and multilayer structure rather than just in single crystals. Additionally, non-polar and semi-polar growth of GaN is being used in industry. It thus becomes necessary to learn the mechanical behaviors and deformation mechanisms of the non-polar and semi-polar GaN crystals. On the other hand, nanoindentation (nanoscratching) created pits (grooves) have been proved to be selective sites for nanocrystals growth and the structure of the nanocrystals is related to the defect structure under the pits (grooves). It would be very interesting to grow such nanocrystals in a controllable manner using controllably introduced defects. But I understand that this is a very challenging task.

REFERENCES

[1] B. G. Yacobi, *Semiconductor Materials: An Introduction to Basic Principles* (Kluwer Academic, New York, 2003), p. 1.

[2] R. F. Pierret, *Semiconductor Device Fundamentals*, (Addison-Wesley, 1996), p. 354.

[3] D. A. Neamen, *Semiconductor Physics and Devices: Basic Principles* (3rd Ed., McGraw-Hill, 2003), p. 617.

[4] I. Vurgaftman , J. R. Meyer, and L. R. Ram-Mohan, J. Appl. Phys. **89**, 5815 (2001).

[5] P. Bhattacharya, *Semiconductor optoelectronic devices* (2nd Ed., Prentice Hall, Upper Saddle River, NJ, 1997), pp. 115-118.

[6] S. M. Sze, and K. K. Ng, *Physics of Semiconductor Devices* (3rd Ed., John Wiley & Sons, Inc., Hoboken, NJ, 2007), p. 30.

[7] V. Swaminathan and A. T. Macrander, *Material Aspects of GaAs and InP Based structures*, (Prentice Hall, Englewood Cliffs, 1991), pp. 265, 266.

[8] P. Bhattacharya, *Properties of Lattice-Matched and Strained InGaAs*, (London, 1993), p. 16.

[9] S. Adachi, *Physical Properties of III-V Semiconductor Compounds*, (Wiley-VCH, Weinheim, 2004), p. 23.

[10] J. C. Phillips, *Bonds and Bands in Semiconductors*, (Academic, New York, 1973), pp. 71-74.

[11] F. A. Ponce, in *Group III-Nitride Semiconductor Compounds*, ed. by B. Gil (Oxford Univ. Press, Oxford, 1998), p. 127.

[12] M. P. Maruska, and J. J. Tietjen, Appl. Phys. Lett. **15**, 327 (1969).

[13] H. Amano, N. Sawaki, I. Akasaki, and Y. Toyoda, Appl. Phys. Lett. **48**, 353 (1986).

[14] F. A. Ponce, and D. P. Bour, Nature, London, **386**, 351 (1997).

[15] I. Ho, and G. B. Stringfellow, Appl. Phys. Lett. **69**, 2701 (1996).

[16] S. Chichibu, T. Azuhata, T. Sota, and S. Nakamura, Appl. Phys. Lett. **69**, 4188 (1996).

[17] F. A. Ponce, D. Cherns, W. T. Young, and J. W. Steeds, Appl. Phys. Lett. **69**, 770 (1996).

[18] F. A. Ponce, Mater. Res. Soc. Bull, **22**, 51 (1997).

[19] D. Cherns, Mater. Sci. and Eng. B. **91/92**, 274 (2002).

[20] L. Gerward, and J. S. Olsen, J. Synchrotron Radiat. **2**, 233 (1995).

[21] S. Desgreniers, Phys. Rev. B. **58**, 14102 (1998).

[22] T. Yamamoto, T. Shiosaki, and A. Kawabata, J. Appl. Phys. **83**, 7844 (1998).

[23] T. Mitsuyu, S. Ono, and K. Wasa, J. Appl. Phys. **51**, 2464 (1980).

[24] A. Hachigo, H. Nakahata, K. Higaki, S. Fujii, and S. Shikata, Appl. Phys. Lett. **65**, 2566 (1994).

[25] K.–K. Kim, J.–H. Song, H.–J. Jung, W.–K. Choi, S.–J. Park, and J.–H. Song, J. Appl. Phys. **87**, 3572 (2000).

[26] P. Fons, K. Iwata, S. Niki, A. Yamada, and K. Matsubara, J. Cryst. Growth. **201-202**, 627 (1999).

[27] R. D. Vispute, V. Talyansky, R. P. Sharma, S. Choopun, M. Downes, T. Venkatesan, Y. X. Li, L. G. Salamanca-Riba, A. A. Lliadis, K. A. Jones, and J. McGarrity Appl. Sur. Sci. **127**, 431 (1998).

[28] Y. Liu, C. R. Gorla, S. Liang, N. Emanetoglu, Y. Lu, H. Shen, and M. Wraback, J. Electron. Mater. **29**, 69 (2000).

[29] N. Takahashi, K. Kaiya, T. Nakamura, Y. Momose, and H. Yamamoto, Jpn. J. Appl. Phys. Part 2 **38**, L454 (1999).

[30] J. Narayan, K. Dovidenko, A. K. Sharma, and S. Oktyabrsky, J. Appl. Phys. **84**, 2597 (1998).

[31] C. Kingshirn, ChemPhysChem. **8**, 782-803 (2007).

[32] D. Tabor, *The Hardness of Metals,* (Oxford University Press, Oxford, 2000).

[33] H. Hertz, J. Reine Angewandte Math. **92**, 156 (1882).

[34] S.I. Bulychev, V.P. Alekhin, M.Kh. Shorshorov, and A.P. Ternovskii, Prob. Prochn. **9**, 79 (1976).

[35] M. Kh. Shorshorov, S. I. Bulychev, and V. P. Alekhin, Sov. Phys. Dokl. **26**, 769 (1982).

[36] J. S. Field and M. V. Swain, J. Mater. Res. **10**, 101 (1995).

[37] W. W. Gerberich, J. C. Nelson, E. T. Lilleodden, P. Anderson, and J. T. Wyrobek, Acta Mater. **44**, 3585 (1996).

[38] P. Tangyunyong, R. C. Thomas, J. E. Houston, T. A. Michalske, R. M. Crooks, and A. J. Howard, Phys. Rev. Lett. **71**, 3319 (1993).

[39] H. Z. Song, Y. Nakata, Y. Okada, T. Miyazawa, T. Ohshima, M. Takatsu, M. Kawabe, and N. Yokoyama, Physica E **21**, 625 (2004).

[40] C. Taylor, E. Marega, E. A. Stach, G. Salamo, L. Hussey, M. Munoz, and A. Malshe, Nanotechnology **19**, 015301 (2008).

[41] H. D. Fonseca-Filho, R. Prioli, M. P. Pires, A. S. Lopes, P. L. Souza, and F. A. Ponce, Appl. Phys. Lett. **90**, 013117 (2007).

[42] F. A. Ponce, Q. Y. Wei, Z. H. Wu, H. D. Fonseca-Filho, C. M. Almeida, R. Prioli, and D. Cherns, J. Appl. Phys. **106**, 076106 (2009).

[43] C. M. Almeida, R. Prioli, Q. Y. Wei, and F. A. Ponce, J. Appl. Phys. **112**, 063514 (2012).

[44] B. G. Yacobi and D. B. Holt, *Cathodoluminescence Microscopy of Inorganic Solids* (Plenum Press, New York, 1990).

[45] P. E. Batson, N. Dellby, and O. L. Krivanek, Nature **418**, 617 (2002).

[46] D. J. Smith, Materials Today. **11**, 30 (2008).

[47] F. A. Ponce, D. P. Bour, W. T. Young, M. Saunders, and J. W. Steeds, Appl. Phys. Lett. **69**, 337 (1996).

[48] B. Fultz, and J. M. Howe, *Tansmission electron microscopy and diffractometry of materials, 2nd edition*. (pp. 362, New York: Springer, 2001).

[49] D. B. Williams, and C. B. Carter, Transmission Electron Microscopy, (Springer, 1996).

[50] P. D. Nellist, Scanning Transmission Electron Microscopy: Imaging and Analysis, (Chapter 2, Springer, 2011).

[51] P. Hartel, H. Rose, and C. Dinges, Ultramicroscopy **63**, 93 (1996).

[52] C. Z. Wang, D. J. Smith, S. Tobin, T. Parodos, J. Zhao, Y. Chang, and S. Sivananthan, J. Vac. Sci. Technol. A **24**, 995 (2006).

[53] L. A. Giannuzzi, and F. A. Stevie, Micron **30**, 197 (1999).

[54] C. K. Hyon, S. C. Choi, S. H. Song, S. W. Hwang, M. H. Son, D. Ahn, Y. J. Park, and E. K. Kim, Appl. Phys. Lett. **77**, 2607 (2000).

[55] H. Z. Song, Y. Nakata, Y. Okada, T. Miyazawa, T. Ohshima, M. Takatsu, M. Kawabe, and N. Yokoyama, Physica E **21**, 625 (2004).

[56] A. Hirai and K. M. Itoh, Physica E **23**, 248 (2004).

[57] H. D. Fonseca-Filho, R. Prioli, M. P. Pires, A. S. Lopes, P. L. Souza, and F. A. Ponce, Appl. Phys. Lett. **90**, 013117 (2007).

[58] C. Taylor, E. Marega, E. A. Stach, G. Salamo, L. Hussey, M. Munoz, and A. Malshe, Nanotechnology **19**, 015301 (2008).

[59] H. D. Fonseca-Filho, R. Prioli, M. P. Pires, A. S. Lopes, P. L. Souza, and F. A. Ponce, Appl. Phys. A.: Mater. Sci. Process. **89**, 945 (2007).

[60] B. Bhushan and V. N. Koinkar, Appl. Phys. Lett. **64**, 1653 (1994).

[61] P. Egberts and R. Bennewitz, Nanotechnology **22**, 425703 (2011).

[62] C. M. Almeida, R. Prioli, and F. A. Ponce, J. Appl. Phys. **104**, 113509 (2008).

[63] J. E. Bradby, J. S.Williams, and J. Wong-Leung, Appl. Phys. Lett. **77**, 23 (2000).

[64] J. E. Bradby, J. S.Williams, and J. Wong-Leung, Appl. Phys. Lett. **78**, 21 (2001).

[65] L. Largeau, G. Patriarche, F. Glas, and E. Le Bourhis, J. Appl. Phys. **95**, 8 (2004).

[66] C.-H. Chien, S.-R. Jian, C.-T. Wang, J.-Y. Juang, J. C. Huang and Y.-S. Lai, J. Phys. D: Appl. Phys. **40**, 3985 (2007).

[67] J. E. Bradby, S. O. Kucheyev, J. S. Williams, J. Wong-Leung, M. V. Swain, P. Munroe, G. Li, and M. R. Phillips, Appl. Phys. Lett. **80**, 3 (2002).

[68] F. A. Ponce, Q. Y. Wei, Z. H. Wu, H. D. Fonseca-Filho, C. M. Almeida, R. Prioli, and D. Cherns, J. Appl. Phys. **106**, 076106 (2009).

[69] H. D. Fonseca-Filho, C. M. Almeida, R. Prioli, M. P. Pires, P. L. Souza, Z. H. Wu, Q. Y. Wei, and F. A. Ponce, J. Appl. Phys. **107**, 054313 (2010).

[70] K. Wasmer, M. Parlinska-Wojtan, R. Gassilloud, G. Pouvreau, J. Tharian, and J. Micher, Appl. Phys. Lett. **90**, 031902 (2007).

[71] P. G. Caldas, R. Prioli, C. M. Almeida, J. Y. Huang, and F. A. Ponce, J. Appl. Phys. **109**, 013502 (2011).

[72] V. Domnich, Y. Gogotsi, and S. Dub, Appl. Phys. Lett. **76**, 2214 (2000).

[73] N. Fujisawa, S. Ruffell, J. E. Bradby, J. S. Williams, B. Haberl, and O. L. Warren, J. Appl. Phys. **105**, 106111 (2009).

[74] K. Wasmer, R. Gassiloud, J. Michler, and C. Ballif, J. Mater. Res. **27**, 320 (2012).

[75] J. Schreiber and S. Vasnyov, J. Phys.: Condens. Matter 16, S75 (2004).

[76] J. L. Bucaille, E. Felder, and G. Hochstetter, Wear **249**, 422 (2001).

[77] G. Patriarche and E. Le Bourhis, Philos. Mag. A **82**, 1953 (2002).

[78] Y. Ahn, T. N. Farris, and S. Chandrasekar, Mechanics of Mater., 29, 143 (1998).

[79] Y. I. Alivov, J. E. Van Nostrand, D. C. Look, M. V. Chukichev, and B. M. Ataev, Appl. Phys. Lett. **83**, 2943 (2003).

[80] Z. K. tang, G. K. L. Wong, P. Yu, M. Kawasaki, A. Ohtomo, H. Koinuma, and Y. Segawa, Appl. Phys. Lett. **72**, 3270 (1998).

[81] C. Soci, Z. Zhang, B. Xiang, S. A. Dayeh, D. P. R. Aplin, J. Park, X. Y. Bao, Y. H. Lo, and D. Wang, Nano Lett. **7**, 1003 (2007).

[82] F. Hamdani, A. Botchkarev, W. Kim, H. Morkoc, M. Yeadon, J. M. Gibson, S. – C. Y. Tsen, D. J. Smith, D. C. Reynolds, D. C. Look, K. Evans, C. W. Litton, W. C. Mitchel, and P. Hemenger, Appl. Phys. Lett. **70**, 467 (1997).

[83] X. Gu, M. A. Reshchikov, A. Teke, D. Johnstone, and H. Morkoc, Appl. Phys. Lett. **84**, 2268 (2004).

[84] A. Kobayashi, S. Kawano, Y. Kawaguchi, J. Ohta, and H. Fujioka, Appl. Phys. Lett. **90**, 041908 (2007).

[85] T. Wei, R. Duan, J. Wang, J. Li, Z. Huo, J. Yang, and Y. Zeng, Jpn. J. Appl. Phys., **47**, 3346 (2008).

[86] C. Noguera, J. Phys.: Condens Mater. **12**, R367 (2000).

[87] T. Makino, K. Tamura, C. H. Chia, Y. Segawa, M. Kawasaki, A. Ohtomo, H. Koinuma, Appl. Phys. Lett. **81**, 2355 (2002).

[88] T. Onuma, H. Amaike, M. Kubota, K. Okamoto, H. Ohta, J. Ichihara, H. Takasu, and S. F. Chichibu, Appl. Phys. Lett. **91**, 181903 (2007).

[89] J. W. Lee, J. H. Kim, S. K. Han, S. K. Hong, J. Y. Lee, S. I. Hong, and T. Yao, J. Cryst. Growth. **312**, 238 (2010).

[90] S. Yang, B. H. Lin, C. C. Kuo, H. C. Hsu, W. –R. Liu, M. O. Eriksson, P. –O. Hotz, S. –S. Chang, C. –H. Hsu, and W. F. Hsieh, Cryt. Growth Des. **12**, 4745 (2012).

[91] Y. Li, Y. Zhang, H. He, Z. Ye, J. Jiang, J. Lu, and J. Huang, Mater. Res. Bull, **47**, 2235 (2012).

[92] Y. Kawai, S. Ohsuka, M. Iwaya, S. Kamiyama, H. Amano, and Isamu Akasaki, J. Cryst. Growth, **311**, 2929 (2009).

[93] T. Kajima, A. Kobayashi, K. Ueno, K. Shimomoto, T. Fujii, J. Ohta, H. Fujioka, and M. Oshima, Jpn. J. Appl. Phys. **49**, 070202 (2010).

[94] S. O. Kucheyev, J. E. Bradby, J. S. Williams, C. Jagadish, and M. V. Swain, Appl. Phys. Lett. **80**, 956 (2002).

[95] M. J. Mayo, R. W. Siegel, Y.X. Liao, and W. D. Nix, J. Mater. Res. **7**, 973 (1992).

[96] J. E. Bradby, S. O. Kucheyev, J. S. Williams, C. Jagadish, M. V. Swain, P. Munroe, and M. R. Phillips, Appl. Phys. Lett. **80**, 4537 (2002).

[97] V. A. Coleman, J. E. Bradby, C. Jagadish, P. Munroe, P Y. W. Heo, S. J. Pearton, D. P. Norton, M. Inoue, and M. Yano, Appl. Phys. Lett. **86**, 203105 (2005).

[98] W. C. Oliver and G. M. Pharr, J. Mater. Res. **7**, 1564, (1992).

[99] J. R. Morris, H. Bei, G. M. Pharr, and E. P. George, Phys. Rev. Lett. **106**, 165502 (2011).]

[100] R. Navamathavan, K.-K. Kim, D.-K. Hwang, S.-J. Park, J.-H. Hahn, T. G. Lee, G.-S. Kim, Appl. Surf. Sci. **253**, 464 (2006).

[101] D. A. Lucca, M. J. Klopfstein, R. Ghisleni, and G. Cantwell, CIRP Annals – Manufac. Tech. **51**, 483 (2002).

[102] B. K. Meyer, H. Alves, D. M. Hofmann, W. Kriegseis, D. Forster, F. Bertram, J. Christen, A. Hoffmann, M. Straßburg, M. Dworzak, and A. V. Rodina. Phys. Stat. Sol. (b) **241**, 231-260 (2004).

[103] A. M. Fisher, S. Srinivasan, R. Garcia, F. A. Ponce, S. E. Guaňo, B. C. Di Lello, F. J. Moura, and I. G. Solŏrzano. Appl. Phys. Lett. **91**, 121905 (2007).

[104] D. G. Zhao, S. J. Xu, M. H. Xie, S. Y. Tong and Hui Yang, Appl. Phys. Lett. **83**, 677 (2003).

[105] A. Mang, K. Reimann, and St. Rübenacke, Sol. Stat. Commun. **94**, 251 (1995).

[106] S. Basu, and M. W. Barsoum, J. Mater. Res., **22**, 2470 (2007).

[107] M. D. Drory, J. W. Ager III, T. Suski, I. Gregoryt, S. Porowski, Appl. Phys. Lett. **69**, 4044 (1996).

[108] S. Srinivasan, L. Geng, R. Liu, F. A. Ponce, Y. Narukawa, and S. Tanaka, Appl. Phys. Lett. **83**, 5187 (2003).

[109] M. Kondow, K. Uomi, A. Niwa, T. Kitatani, S. Watahiki, Y. Yazawa, Jpn. J. Appl. Phys. **35**, 1273 (1996).

[110] S. R. Kurtz, A. A. Allerman, E. D. Jones, J. M. Gee, J. J. Banas, B. E. Hammons, Appl. Phys. Lett. **74**, 729 (1999).

[111] M. Yamaguchi, T. Takamoto, K. Araki, N. Ekins-Dauks, Sol. Energy **79**, 78 (2005).

[112] S. R. Kurtz, A.A. Allerman, C.H. Seager, R.M. Sieg, E. D. Jones, Appl. Phys. Lett. **70**, 700 (2000).

[113] D. J. Friedman, Current Opinion in Solid state and Material Science, **14**, 131 (2010).

[114] D. B. Jackrel, S. R. Bank, H. B. Yuen, M.A. Wistey, J. S Harris Jr, A.J. Ptak, S.W. Johnston, D.J. Friedman, S.R. Kurtz, J. Appl. Phys.**101**, 114916 (2007).

[115] Y. Shimizu, N. Miyashita, Y. Mura, A. uedono, Y. Okada, J. Crystal Growth. **579**，301-302, (2007).

[116] L. Borkovska, O. Yafanov, O. Gudymenko, S. Johnson, V. Kladko, N. Korsunska, T Kryshtab, Y. Sadofyev, Y.-H. Zhang, Thin Solid Films **515**, 786 (2006).

[117] Y. Qui, S. A. Nikisin, H. Temkin, V. A. Elyukhin, Y. A. Kudriavtsev, Appl. Phys. Lett. **70**, 2831 (1997).

[118] T. Hakkarainen, E.-M. Pavelescu, J. Likonen, Physica E **32**, 266 (2006).

[119] S. R. Bank, H. B. Yuen, H. Bae, M. A. Wistey, J.S. Harris Jr., Appl. Phys. Lett. **88**, 221115 (2006).

[120] X. Kong, A. Trampert, E. Tournie, K. H. Ploog, Appl. Phys. Lett. **87**, 171901 (2005).

[121] T. Gugov, V. Gambin, M. Wistey, H. Yuen, S. Bank, J. S. Harris. Jr., J. Vac. Sci. Technol. B **22**, 1588 (2004).

[122] Y. Kamikawa-Shimizu, S. Niki, Y. Okada, Solar Energy Materials and Solar Cells, **93**, 1120 (2008).

[123] N. Miyashita, S. Ichikawa, Y. Okada, J. Crystal Growth **311**, 3249 (2009).

[124] S. R. Bank, H.P. Bae, H.B. Yuen, M.A. Wistey, L.L. Goddard, J.S. Harris Jr., Electron. Lett. **42**, 156 (2006).

[125] A. J. Ptak, R. France, C.-S. Jiang, R.C. Reedy, J. Vac. Sci. Technol. B **26**, 1053 (2008).

[126] Y. Shimizu, N. Kobayashi, A. Uedono, Y. Okada, J. Crystal Growth **278**, 553 (2005).

[127] M. Tabuchi, S. Noda, and A. Sasaki, J. Crystal Growth **115**, 169 (1991).

[128] K. Kim, A. Zunger, Phys. Rev. Lett. **86**, 2609 (2001).

[129] W. A. Harrison, Electronic Structure and the Properties of Solids (pp. 175-176, Dover, New York, 1989).

[130] X. Kong, A. Trampert, K.H. Ploog, Micron **37**, 465 (2006).

[131] F. A. Ponce, S. Srinivasan, A. Bell, L. Geng, R. Liu, M. Stevens, J. Cai, H. Omiya, H. Marui, and T. Tanaka, Phys. Stat. Sol. B **240**, 273 (2003).

[132] V. G. Deibuk and A. V. Coznyi, Semiconductors. **39**, 623 (2005).

[133] J. Phillips et al, Laser Photonics Rev. **1**, 307 (2007).

[134] S. Pereira, M. R. Correia, E. Pereira, K. P. O'Donnell, C. Trager-Cowan, F. Sweeney, and E. Alves, Phys. Rev. B **64**, 205311 (2001).

[135] M. Hao, H. Ishikawa, T. Egawa, C. L. Shao, and T. Jimbo, Appl. Phys. Lett. **82**, 4702 (2003).

[136] J. F. Carlin and M. Ilegems, Appl. Phys. Lett. **83**, 668 (2003).

[137] R. Butté, J.-F. Carlin, E. Feltin, M. Gonschorek, S. Nicolay, G. Christmann, D. Simeonov, A. Castiglia, J. Dorsaz, H. J. Buehlmann, S. Christopoulos, G. Baldassarri Höger Von Högersthal, A. J. D. Grundy, M. Mosca, C. Pinquier, M. A. Py, F. Demangeot, J. Frandon, P. G. Lagoudakis, J. J. Baumberg, and N. Grandjean, J. Phys. D **40**, 6328 (2007).

[138] Z. T. Chen, S. X. Tan, Y. Sakai, and T. Egawa, Appl. Phys. Lett. **94**, 213504 (2009).

[139] F. A. Ponce, D. Cherns, W. T. Young, and J. W. Steeds, Appl. Phys. Lett. **69**, 770 (1996).

[140] D. Cherns, W. T. Young, J. W. Steeds, F. A. Ponce, and S. Nakamura, J. Crystal Growth. **178**, 201 (1997).

[141] D. Cherns, W. T. Young, J. W. Steeds, F. A. Ponce, and S. Nakamura, Phil. Mag. A **77**, 273 (1998).

[142] J. E. Northup, L. T. Romano, and J. Neugebauer, Appl. Phys. Lett. **74**, 2319 (1999).

[143] L. Zhou, D. J. Smith, M. R. Mccartney, D. S. Katzer, and D. F. Storm, Appl. Phys. Lett. **90**, 081917 (2007).

APPENDIX

LIST OF PUBLICATIONS DURING THE STUDY TOWARDS THE DOCTORAL DEGREE

Publications that resulted from my work at ASU are listed below:

[1] T. Li, Q. Y. Wei, A. M. Fischer, J. Y. Huang, Y. U. Huang, F. A. Ponce, J. P. Liu, Z. Lochner, J.–H, Ryou, and R. D. Dupuis, "The effect of InGaN underlayers on the electronic and optical properties of InGaN/GaN quantum wells", Appl. Phys. Lett. **102**, 04115 (2013).

[2] Q. Y. Wei, T. Li, J. Y. Huang, F. A. Ponce, E. Tschumak, A. Zado, and D. J. As, "Free carrier accumulation at cubic AlGaN/GaN heteojunctions", Appl. Phys. Lett. **100**, 142108 (2012).

[3] Q. Y. Wei, T. Li, J. Y. Huang, Z. T. Chen, T. Egawa, and F. A. Ponce, "Compositional instability in InAlN/GaN lattice-matched epitaxy", Appl. Phys. Lett. **100**, 092101 (2012).

[4] R. Oshima, J. Y. Huang, N. Miyashita, K. Matsubara, Y. Okada and F. A. Ponce, "Transmission electron microscopy study of GaInNAs(Sb) thin films grown by atomic hydrogen-assisted molecular beam epitaxy", Appl. Phys. Lett. **99**, 191907 (2011).

[5] J. Y. Huang, Fernando. A. Ponce, P. G. Caldas, C. M. Almeida, R. Prioli, "Microstructure of nanoscratched semiconductors", J. Phys. Conf. Ser. **326**, 012061 (2011).

[6] P. G. Caldas, R. Prioli, C. M. Almeida, J. Y. Huang and F. A. Ponce, "Plastic hardening in cubic semiconductors by nanoscratching", J. Appl. Phys. **109**, 013512(2010).

[7] J. Kim, Z. Lochner, M.-H. Ji, S. Choi, H.-J. Kim, J.-S. Kim, R. D. Dupuis, A. M. Fischer, R. Juday, Y. Huang, T. Li, J. Y. Huang, F. A. Ponce, J.-H. Ryou. "Origins of unintentional incorporation of gallium in InAlN layers during epitaxial growth", J. Cryst. Growth, 17 March 2013. (http://dx.doi.org/10.1016/ j.jcrysgro.2013.03.029)

[8] R. Juday, E. M. Silva, J. Y. Huang, P. G. Caldas, R. Prioli, and F. A. Ponce, "Strain-related optical properties of ZnO crystals due to nanoindentation on various surface orientations", J. Appl. Phys., submitted January 2013.

[9] J. Kim, Z. Lochner, M.-H. Ji, S. Choi, H.-J. Kim, J.-S. Kim, R. D. Dupuis, A. M. Fischer, R. Juday, Y. Huang, T. Li, J. Y. Huang, F. A. Ponce, J.-H. Ryou, "Origins of unintentional incorporation of gallium in InAlN layers during epitaxial growth, Part II: Effects of growth chamber conditions and underlying layers", J. Cryst. Growth, submitted 25 March 2013.